

**MODELLING AND SIMULATION OF DIESEL CATALYTIC DEWAXING
REACTORS**

By

© Eugenio Turco Neto

A thesis submitted to the

School of Graduate Studies

in partial fulfillment of the requirements for the degree of

Master of Engineering

Faculty of Engineering and Applied Sciences

Memorial University of Newfoundland

May, 2017

St. John's

Newfoundland

Abstract

Designing catalytic dewaxing reactors is a major challenge in petroleum refineries due to the lack of kinetic studies related to this operation. Also, the measurements of the cloud point of diesel fuels produced from those units are still being carried out using inaccurate visual procedures, which bring difficulties to the process control design. In this thesis, a single event kinetic model is developed for catalytic dewaxing on Pt/ZSM-5, which application has not been explored in the scientific literature. A total of 14 kinetic parameters have been estimated from experimental data, which are independent on the feedstock type. Then, the obtained parameters were used to propose a soft-sensor consisting of three different modules that handles the feedstock distillation data and integrates a mechanistic reactor model to a solid-liquid flash algorithm to predict the cloud point of the diesel product. Finally, a surrogate model is developed using a sequential design of experiments to simplify the sensor framework and reduce the computing time so that it can be industrially implemented to perform on-line cloud point estimations. The results have showed that the proposed kinetic model was in agreement with observed data and suitable to simulate the industrial operation. Pressure, temperature, and liquid hourly space velocity (LHSV) were found to be the main process variables controlling the conversion in the hydrodewaxing mechanism. The proposed sensor showed to be suitable to study the reactor performance for different set of operating conditions. Also, the surrogate model drastically reduced the computing time to obtain the cloud point estimations and showed to be suitable for on-line prediction purposes. Finally, the employed sequential design strategy revealed that nonlinearities can strongly affect the sensor accuracy if not properly handled.

Acknowledgements

First of all, I would like to thank my supervisors Dr. Syed Imtiaz and Dr. Salim Ahmed for all their support, motivation, and encouragement to carry out this research through courses and regular meetings, which were crucial at every stage of this work. They have been an inspiration for my future career. Also, I would like to express my gratitude to Dr. Mohammed Aziz Rahman for always giving me advises on how to carry out research and provide me opportunities to show my full potential as an engineer. I would also like to thank Dr. Jorge Martinis from Bryan Research & Engineering for his knowledgeable advises on how to calculate the single event numbers and rate constants. I also acknowledge the financial support from Imperial Oil, Research & Development Corporation (RDC), and the Natural Sciences and Engineering Research Council of Canada (NSERC).

I would also like to thank my parents Edson and Nilda Turco and my sister Ana Carolina Turco. Their teaching and support throughout my life were essential to bring me to success and I am going to be grateful for the rest of my life. I would like to express my intense gratitude to my fiancé Jordan Chafe and her parents Peggy and Roger Chafe for their patience and support either emotional or financial throughout my stay in Canada and making this entire process smooth.

Finally, I would like to acknowledge all my friends from Canada and Brazil in special Arthur Altoé, Karla Fuglem, Gordon Pike, Derek Ryan, Sean Jessome, Steve Dorey, Plinio Ferreira Pinto, Murilo Texeira, Henrique Botelho, Livia Okabe Botelho, Robson Domingos, Renan Domingos, and my friends from MUN Process Engineering Classes of 2016, 2017, and 2018.

Table of Contents

Abstract	ii
Acknowledgements.....	iii
List of Tables	viii
List of Figures	x
List of Symbols and Abbreviations.....	xiv
Introduction.....	1
1.1. Motivation of the Research	5
1.2. Objectives	8
1.3. Organization of the Thesis	9
Literature Review.....	11
2.1. Preface.....	11
2.2. Kinetic Modelling for Conventional Hydrocracking Reactors	12
2.3. Kinetic Modelling for Shape-Selective Hydrocracking and Hydroisomerization Processes	15
2.4. Cloud Point Estimation	21
Single Event Kinetic Modelling of Catalytic Dewaxing on Commercial Pt/ZSM-5.....	25
3.1. Preface.....	25
3.2. Introduction.....	25

3.3. Reactor Modeling.....	30
3.3.1. Shape-Selectivity Effects	30
3.3.2. Reaction Mechanism.....	32
3.3.3. Reaction Network Generation.....	34
3.3.4. Single Event Kinetic Modelling.....	45
3.3.5. Posteriori-Lumping	47
3.3.6. Rate Expressions and Kinetic Parameters.....	48
3.3.7. Reactor Model.....	57
3.3.8. Physical Properties Estimation.....	60
3.4. Results and Discussions	61
3.4.1. Parameter Estimation	61
3.4.2. Effect of Temperature	68
3.4.3. Effect of Pressure	69
3.4.4. Effect of H ₂ /HC Ratio.....	71
3.4.5. Effect of Liquid Hourly Space Velocity (LHSV).....	72
3.4.6. Effect of Feed Carbon Number.....	74
3.4.7. Effect of Shape-Selectivity	76
3.5. Conclusion	77

Development of a Diesel Cloud Point Soft-Sensor using Thermodynamic and Mechanistic Models.....	79
4.1. Preface.....	79
4.2. Introduction.....	79
4.3. Cloud Point Soft-Sensor Design	82
4.3.1. Soft-Sensor Description	82
4.3.2. Molecular Type and Homologous Series (MTHS) Matrix	86
4.3.3. Hydrodewaxing (HDW) Reactor Model.....	91
4.3.4. Hydrodesulfurization Reactor Model.....	95
4.3.4.1. Reaction Network	95
4.3.4.2. Kinetic Parameters and Rate Equations	98
4.3.4.3. Reactor Model.....	102
4.3.5. Solid-Liquid Equilibrium Thermodynamic Model.....	103
4.3.6. Fuzzy Local Linear Approximation (FLOLA)	109
4.3.7. Monte-Carlo Voronoi Approximation	115
4.3.8. FLOLA-Voronoi Sequential Design Strategy	118
4.3.9. Gaussian Process Surrogate Model.....	120
4.4. Results and Discussions	123
4.4.1. Industrial Case Study	123

4.4.2. Design of Computer Experiments.....	134
4.4.3. Nonlinearity Tracking and Exploration Capability.....	138
4.4.4. On-line Cloud Point Soft-Sensor Application	140
4.5. Conclusions.....	146
Conclusions and Recommendations	148
5.1. Conclusions.....	148
5.2. Recommendations and Future Work	151
Bibliography	153
Appendix A-1. Industrial Diesel Feedstock MTHS Matrix.....	163
Appendix A-2. Validation of The Reaction Network Algorithm	164

List of Tables

Table 1-1: Comparison between MDDW and MIDW dewaxing processes [2]	2
Table 1-2: Common ranges for operating conditions and feedstock specifications for industrial catalytic dewaxing reactors integrated to hydrotreating units [2].....	4
Table 3-1: Assumed elementary steps promoted by metal and acid sites on Pt/ZSM-5....	33
Table 3-2: Number of elementary steps generated by the reaction network for n-hexadecane	44
Table 3-3: Number of species generated by the reaction network for n-hexadecane	44
Table 3-4: Single-event kinetic rate constants and Langmuir equilibrium coefficients for shape-selective Pt/ZSM-5	47
Table 3-5: Composite single-event Arrhenius and Langmuir adsorption parameters to be estimated	55
Table 3-6: Estimated single-event rate and Langmuir equilibrium constants for Pt/ZSM-5	64
Table 3-7: Langmuir physisorption equilibrium constants for Pt/US-Y and Pt/ZSM-5 at $T = 249.32^{\circ}\text{C}$	76
Table 4-1: Distillation curve and bulk properties for an industrial diesel feedstock	87
Table 4-2: Validation results obtained from the MTHS algorithm.....	90
Table 4-3: Common elementary steps promoted by metal and acid sites on Pt/ZSM-5....	92
Table 4-4: Hougen-Watson rate equations for the main reactions taking place in HDS process [54, 55]	98

Table 4-5: Arrhenius expressions for the rate constants for the HDS mechanisms [54, 55]	99
Table 4-6: Van't Hoff expressions for the adsorption equilibrium constants for the HDS mechanisms [54, 55]	100
Table 4-7: Stoichiometric table for hydrodesulfurization reactions	101
Table 4-8: Validation of solid-liquid equilibrium algorithm for cloud point estimation.	109
Table 4-9: Adopted constraints for operating conditions and reactor dimensions	125
Table 4-10: Reactor dimensions and operating conditions for the industrial reactor unit	126
Table 4-11: Comparison between target and calculated values for the output variables.	127
Table 4-12: Process variables and ranges adopted to develop the diesel cloud point predictor	135
Table 4-13: Estimated hyperparameters of the cloud point surrogate model	140
Table 4-14: Comparison between each type of model considered in the sensor framework in terms of computing time	146

List of Figures

Figure 1-1: Multi-bed hydrodesulfurization and hydrodewaxing process configuration [2]3	
Figure 1-2: Hydrotreating and hydrodewaxing unit in series for seasonal operations [2]...3	
Figure 3-1: Boolean matrix representation for 2-methyl-4-heptyl	35
Figure 3-2: Characterization vector form.....	36
Figure 3-3: Characterization vector of 2-methyl-4-octyl.....	36
Figure 3-4: Molecular structure, characterization vector, and Boolean matrix for 3-methyl-4-heptyl	37
Figure 3-5: Boolean matrix indicating the β -carbon positions in the molecular structure	38
Figure 3-6: Possible PCP structures formed from 3-methyl-4-heptyl	38
Figure 3-7: Boolean matrix for the PCP structure in consideration.....	39
Figure 3-8: Isomerization pathways.....	40
Figure 3-9: Boolean matrix for the product isomer obtained through α -cleavage.....	41
Figure 3-10: Standardized Boolean Matrix for product ion resulted from the α -Ckeavage pathway.....	42
Figure 3-11: Computer representation for the considered α -Cleavage elementary step....	42
Figure 3-12: General algorithm to build the reaction network for an elementary step type	43
Figure 3-13: Calculation routine to obtain the lumping coefficients of consumption and formation.....	56
Figure 3-14: Schematic representation of the calculation routine adopted to solve the reactor model	59

Figure 3-15: Optimization framework for kinetic parameter estimation.....	63
Figure 3-16: Total conversion profile for n-hexadecane feed.....	65
Figure 3-17: Isomerization yield profile for n-hexadecane feed.....	66
Figure 3-18: Combined molar flow rate profiles for reactor temperatures at 298.03°C (top) and 317.12°C (bottom).....	68
Figure 3-19: Effect of pressure on total conversion, isomerization, and cracking yields for n-hexadecane feed at LHSV = 0.4 h ⁻¹ , T = 298.03°C, and H ₂ /HC = 2.016	70
Figure 3-20: Effect of the H ₂ /HC ratio on total conversion, isomerization, and cracking yields for n-hexadecane feed at LHSV = 0.4 h ⁻¹ , T = 298.03°C, and P = 69.96 bar.....	71
Figure 3-21: Effect of the LHSV on total conversion, isomerization, and cracking yields for n-hexadecane feed at H ₂ /HC = 2.016, T = 298.03°C, and P = 69.96 bar	73
Figure 3-22: Effect of the feedstock carbon number on total conversion, isomerization, and cracking yields for LHSV = 0.4 h ⁻¹ , H ₂ /HC = 2.016, T = 298.03°C, and P = 69.96 bar ...	75
Figure 4-1: Schematic representation for the proposed cloud point soft-sensor framework	83
Figure 4-2: Comparison between industrial and calculated TBP curves	91
Figure 4-3: Mechanism for hydrodesulfurization of dibenzothiophene [54].....	96
Figure 4-4: Mechanism for hydrodesulfurization of 4,6-dimethyldibenzothiophene [55]	97
Figure 4-5: Solid-Liquid Equilibrium Calculation Algorithm [29]	108
Figure 4-6: Algorithm to estimate the Voronoi cell volume [46].....	117
Figure 4-7: FLOLA-Voronoi Sequential Design Strategy [47]	119
Figure 4-8: Schematic representation of the industrial reactor unit under study	123
Figure 4-9: Simulated temperature profile across the industrial unit	128

Figure 4-10: Simulated sulfur concentration profile along the industrial reactor.....	129
Figure 4-11: Mole flow rate evolution for the sulfur compounds along the industrial reactor	129
Figure 4-12: Effect of inlet temperature on the product cloud point and sulfur content at different pressures for $LHSV = 3.25 \text{ hr}^{-1}$	131
Figure 4-13: Effect of inlet pressure on the product cloud point and sulfur content at different temperatures for $LHSV = 3.25 \text{ hr}^{-1}$	132
Figure 4-14: Effect of LHSV on the product cloud point and sulfur content at different temperature conditions at $P_{\text{reactor}} = 54 \text{ bar}$	133
Figure 4-15: Effect of LHSV on the product cloud point and sulfur content at different pressure conditions at $T_{\text{in}} = 613 \text{ K}$	133
Figure 4-16: Overall algorithm for the cloud point surrogate model development	137
Figure 4-17: Contour plots for the true “Peaks” function (left) and surrogate model (right)	139
Figure 4-18: Comparison between initial (left) and final (right) experiment designs	139
Figure 4-19: Parity plot comparing the cloud point response for the product diesel obtained from surrogate model (Predicted) and detailed model (Actual) for the validation data set	142
Figure 4-20: Comparison between surrogate model and original soft-sensor responses for both training and validation data sets.....	143
Figure 4-21: Residuals between the responses obtained from surrogate and reactor model- based soft-sensors	144

Figure 4-22: Comparison between FLOLA-Voronoi and Latin Hypercube designs in terms of surrogate model accuracy 145

List of Symbols and Abbreviations

Symbol	Definition
ARD	Automatic relevance determination
BCH	Bicyclohexyl
BPH	Biphenyl
CP	Cloud Point in °C
DBT	Dibenzothiophene
DMDBT	4,6-dimethyldibenzothiophene
DMBPH	4,6-dimethylbiphenyl
FLOLA	Fuzzy local linear approximation
HDW	Hydrodewaxing
HDS	Hydrodesulfurization
LHSV	Liquid hourly space velocity in hr ⁻¹
MeABP	Mean average boiling point in °C
MCHT	3-methylcyclohexyltoluene
MDDW	Mobil Distillate Dewaxing
MIDW	Mobil Isomerization Dewaxing
PCB	Protonated cyclobutane
PCP	Protonated cyclopropane
TBP	True Boiling Point in K
ULSD	Ultra low sulfur diesel

a_v	Gas-liquid specific surface area in m_i^2/m_r^3
A	Reactor cross-sectional area in m_r^2
A_d	Adhesion
\tilde{A}_l	Single event frequency factor for l type elementary step in h^{-1}
$\tilde{A}_{pr/de}$	Van't Hoff frequency factor for protonation/deprotonation elementary step in $kg/kmol$
\tilde{A}_l^*	Composite frequency factor for l type elementary step in $kmol/kg\ h$
C	Cohesion
C_i	Concentration of component i in $kmol/m_r^3$
C_i^G	Gas phase concentration of the lump i in $kmol/m_G^3$
C_i^L	Liquid phase concentration of the lump i in $kmol/m_L^3$
C_{pG}	Specific heat capacity of gas phase in $kJ/kmol\ K$
C_{pL}	Specific heat capacity of liquid phase in $kJ/kmol\ K$
$C_{L_m}^L$	Concentration of lump L_m in liquid phase in $kmol/m_r^3$
$C_{H_2}^L$	Concentration of hydrogen in liquid phase in $kmol/m_r^3$
$C_{P_i}^L$	Concentration of paraffin P_i in liquid phase in $kmol/m_r^3$
C_n	Carbon number

C_{sat}	Saturation surface concentration of physisorbed paraffins in kmol/kg
C_t	Surface concentration of total active sites in kmol/kg
CP_{imp}	Cloud point improvement in °C
d	Number of dimensions in the design space
$E(\mathbf{x}_r)$	Overall linear approximation deviation
E_l	Activation energy for l type elementary step in kJ/kmol
$f_h(\mathbf{x})$	Characteristic functions of \mathbf{X}
\hat{f}_i^L	Liquid phase fugacity coefficient of component i in mixture in bar
\hat{f}_i^S	Solid phase fugacity coefficient of component i in mixture in bar
$f_{i,pure}^L$	Liquid phase fugacity coefficient of pure component i in bar
$f_{i,pure}^S$	Solid phase fugacity coefficient of pure component i in bar
F_i^G	Molar flow rate of lump i in gas phase in kmol/h
F_i^L	Molar flow rate of lump i in liquid phase in kmol/h
$F_{n-C_{16},0}^G$	Inlet molar flow rate of n-hexadecane in gas phase in kmol/h
$F_{n-C_{16},0}^L$	Inlet molar flow rate of n-hexadecane in liquid phase in kmol/h
$F_{n-C_{16},out}^G$	Outlet molar flow rate of n-hexadecane in gas phase in kmol/h
$F_{n-C_{16},out}^L$	Outlet molar flow rate of n-hexadecane in liquid phase in kmol/h

\mathbf{g}	Gradient vector
h	Planck constant in J s
k_B	Boltzmann constant in J/K
k	Rate constant in h^{-1}
$\tilde{k}_{PCP}(m, w)$	Single event rate constant for PCP-isomerization forming carbenium ion of w type from m type carbenium ion in hr^{-1}
$\tilde{k}_{cr}(m, w, O)$	Single event rate constant for β -scission cracking forming carbenium ion of w type and olefin of O type from m type carbenium ion in hr^{-1}
\tilde{k}^*	Composite single event rate constant in kmol/kg h
$\tilde{K}_{DH}^{(P_i \leftrightarrow O_{ij})}$	Single event dehydrogenation equilibrium constant in kmol kg/m_r^6
$\tilde{K}_{isom}^{(O_{ij} \leftrightarrow O_r)}$	Single event isomerization equilibrium constant between O_{ij} and reference olefin O_r
$\tilde{K}_{pr/de}^{(O_r \leftrightarrow m_{ik})}$	Single event protonation equilibrium constant between reference olefin O_r and carbenium ion m_{ik} in kg/kmol
$k_{i,\sigma}$	Rate constant of hydrogenolysis of component i at σ -sites in kmol/kg h
$k_{i,\tau}$	Rate constant of hydrogenation of component i at τ -sites in kmol/kg h
k_G	Gas phase volumetric mass transfer film coefficient in $\text{m}_G^3/\text{m}_i^2 \text{ h}$
k_L	Liquid phase volumetric mass transfer film coefficient in $\text{m}_L^3/\text{m}_i^2 \text{ h}$
$k_{o,i}$	Overall mass transfer coefficient in $\text{m}_r^3/\text{m}_i^2 \text{ h}$

$K_i^{C,VLE}$	Concentration based equilibrium constant in m_L^3/m_G^3
K_i^{VLE}	True vapor-liquid equilibrium constant
$K_{i,\sigma}$	Langmuir adsorption of component i at σ -sites in $m_L^3/kmol$
$K_{i,\tau}$	Langmuir adsorption of component i at τ -sites in $m_L^3/kmol$
$K_{L,j}$	Langmuir adsorption constant for j type paraffin in $m_r^3/kmol$
K_i^{SL}	Solid-liquid equilibrium constant of component i
M_i	Molecular weight of component i in kg/kmol
$M_{i,j}$	Molecular weight of molecular type j and homologous series i in kg/kmol
M^{cal}	Calculated molecular weight in kg/kmol
M^{ind}	Molecular weight from industrial data in kg/kmol
n	Number of olefins producing a given carbenium ion
n_C	Number of normal paraffinic compounds
n_e	Number of single events
n_P	Number of design points
n_R	Number of responses in the design of experiments
n_S	Number of random points
N	Number of components

N_i	Interphase mass transfer flux of the i-th lump in kmol/m _r ² h
N_{obs}	Number of observations
N_R	Number of reactions
N_{RES}	Number of responses
P	Pressure in bar
$P_{reactor}$	Reactor pressure in bar
q_T	Number of l type elementary steps consuming carbenium ions of m type in lump L _m and forming w type carbenium ions
R	Ideal gas constant in kJ/kmol K
$R_{L_m, l, m, w}^{cons}$	Rate of consumption of carbenium ions of m type in lump L _m and forming w type carbenium ions through l type elementary step in kmol/m _r ³ h
$R_{L_m, l, k, l, m, w}^{form}$	Rate of formation of carbenium ions of w type in lump L _m from carbenium ions of m in lump L _k in kmol/m _r ³ h
$R_{L_m}^{net}$	Net rate of formation of lump L _m in kmol/m _r ³ h
$r_{i, \sigma}$	Rate of formation of component i at σ-sites in kmol/kg h
$r_{i, \tau}$	Rate of formation of component i at τ-sites in kmol/kg h
s	Random point
$S[i, j]$	Stoichiometric coefficient of component i reacting in reaction j
SG_{ij}	Specific gravity of molecular type j and homologous series i

SG^{ind}	Specific gravity from industrial data
SG^{cal}	Calculated specific gravity
SSE	Sum of squares error
T	Temperature in K
T_C	Critical Temperature in K
T_{in}	Reactor inlet temperature in K
T_i^f	Fusion temperature of component i in K
T_G	Temperature of gas phase in K
T_L	Temperature of liquid phase in K
T_G^{out}	Outlet gas temperature of a HDS bed in K
T_L^{out}	Outlet liquid temperature of a HDS bed in K
u_G	Superficial velocity of gas phase in m _r /h
u_L	Superficial velocity of liquid phase in m _r /h
v	Total number of neighbor points
V_i	Molar volume of component i in cm ³ /mol
V_{TBP}^{ind}	Percent volume distilled from industrial data
V_{TBP}^{cal}	Calculated percent volume distilled
W	Weighting matrix

W_{low}	Fuzzy set for low weighting factors
$W_{average}$	Fuzzy set for average weighting factors
W_{high}	Fuzzy set for high weighting factors
W	Weighting factor
$W_{i,j}$	Weight fraction of molecular type j and homologous series i
X	Experiment design
X_{tot}	Total conversion in %
\mathbf{X}	Neighbor point
$x_{i,j}$	Mole fraction of molecular type j and homologous series i
\mathbf{x}_r	Reference design point
\mathbf{x}_{rv}	v-th neighbor with respect to the reference \mathbf{x}_r
x_{new}	Additional point
x_j^{cal}	Calculated total mole fraction of molecular type j
x_{aro}^{cal}	Calculated total aromatic mole fraction
x_{nap}^{cal}	Calculated total naphthenic mole fraction
x_{par}^{cal}	Calculated total paraffinic mole fraction
x_S^{cal}	Calculated total sulfur mole fraction
x_{aro}^{ind}	Total aromatic mole fraction from industrial data

x_{nap}^{ind}	Total naphthenic mole fraction from industrial data
x_{par}^{ind}	Total paraffinic mole fraction from industrial data
x_S^{ind}	Total sulfur mole fraction from industrial data
x_i^L	Mole fraction of component i in liquid phase
x_i^S	Mole fraction of component i in solid phase
Y_{iso}	Isomerization yield in %
\mathbf{y}	Vector of model response
y_i	Actual model response
\hat{y}_i	Surrogate model response
y_{ij}	Predicted value of the response
\hat{y}_{ij}	Experimental value of the response
y_{i,L_m}	Equilibrium composition of i-th isomer within lump L_m
z	Axial position in m_r
β_k	Characteristic parameters
$\varepsilon(\mathbf{x})$	Modelling error at design point \mathbf{X}
ε_b	Bulk void fraction
σ^2	Error variance
σ_f	Signal standard deviation

$\sigma_{gl}^{\#}$	Global symmetry number of activated complex
σ_{gl}^r	Global symmetry number of reactant
ρ_{molar}^G	Molar density of gas phase in kmol/mG ²
ρ_{molar}^L	Molar density of liquid phase in kmol/mL ²
γ_i^{fv}	Free-volume activity coefficient of specie i
γ_i^L	Liquid phase activity coefficient of specie i
γ_i^{res}	Residual activity coefficient of specie i
γ_i^S	Solid phase activity coefficient of specie i
θ_k	Characteristic length scale for the h-th variable
ΔC_P^{LS}	Phase change heat capacity in cal/mol K
$\Delta G_{f,i}^{0,L}$	Standard Gibbs energy of formation of component i in kJ/kmol
ΔH_i^f	Fusion enthalpy of component i in kJ/mol
$\Delta H_{L,j}$	Enthalpy of adsorption for paraffinic type j in kJ/kmol
$\Delta H_{pr/de}$	Protonation/deprotonation enthalpy change in kJ/kmol
ΔH_{sub}	Sublimation enthalpy in kJ/mol
ΔH_{tr}	Transition enthalpy in kJ/mol
ΔH_{vap}	Vaporization enthalpy in kJ/mol
ΔH_{vi}	Heat of vaporization of compound i in kJ/kmol

$\Delta H^{0\#}$	Intrinsic enthalpy difference in kJ/kmol
$\Delta S^{0\#}$	Intrinsic entropy difference in kJ/kmol K
μ	Mean of stochastic process
λ_{ij}	Interaction energy between paraffinic molecules "i" and "j" cal/mol
Λ	Characteristic energy
ω	Acentric factor

Chapter 1

Introduction

Heavy paraffins in diesel fuels have been pointed out as a major concern for oil refineries located in countries with harsh winter conditions. As those compounds have high values of fusion temperature, they crystallize when the fuel is exposed to low temperatures causing wax formation in automotive filters. To overcome this problem, Exxon Mobil created a new process similar to hydrocracking called catalytic dewaxing, which uses bifunctional shape-selective catalysts such as Pt/ZSM-5 to either isomerize or break down heavy paraffins through selective isomerization and cracking reactions [1]. In order to quantify the impact of the process on the diesel cold flow properties, the cloud point, which is highest temperature at which the first wax crystal forms, is used as a product specification [2]. There are strong evidences that by increasing the hydrodewaxing conversion, the cloud point of the diesel product is indeed reduced; however, the increase in the severity of the process favours the cracking steps and diesel yield losses may increase [1].

Two types of catalytic dewaxing processes are applied in the refining industry: Selective cracking dewaxing (MDDW) and selective isomerization dewaxing (MIDW). MDDW is the oldest process and reduces the cloud point of middle-distillates by selectively cracking down heavy into smaller paraffins [2]. The main disadvantage is the high yield losses of diesel at high conversions, which can be avoided by using a feedstock with higher final boiling point so that the loss of diesel can be balanced by the cracking conversion itself. MIDW favours the isomerization route in the reaction mechanism and increases the degree

of branching of the heavy paraffins without lowering their carbon number. Therefore, the diesel yield loss is less compared to MDDW. A performance comparison between the MDDW and MIDW processes is shown in Table 1-1.

Table 1-1: Comparison between MDDW and MIDW dewaxing processes [2]

	Dewaxing Process		
	MIDW	MDDW	MIDW Advantage
Yield (%wt)			
C₁-C₅	2	9.5	-7.5
C₅-145°C	3	11.5	-8.5
145°C+	95	79	+16
Delta pour point (°C)	-30	-30	0

It can be noted that no improvement in the pour point was observed for the MDDW process; however, the amount of lighter products is significantly higher than that observed for the MIDW operation. Due to the negative influence of nitrogen and sulfur compounds on the dewaxing activity, the feedstock must be first hydrotreated. Therefore, placing the hydrotreating and hydrodewaxing catalytic beds in the same unit or in series is a common practice in oil refineries [2]. The schematic representation of catalytic dewaxing process in multi-stage and series configurations are shown in Figures 1-1 and 1-2, respectively.

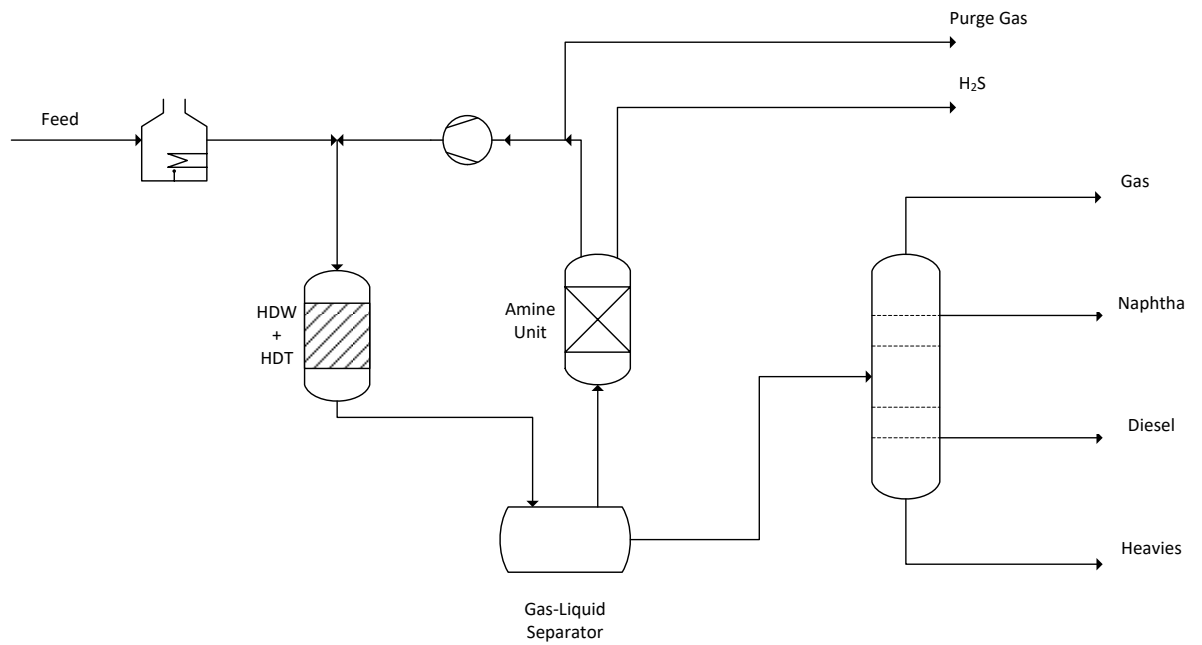


Figure 1-1: Multi-bed hydrodesulfurization and hydrodewaxing process configuration [2]

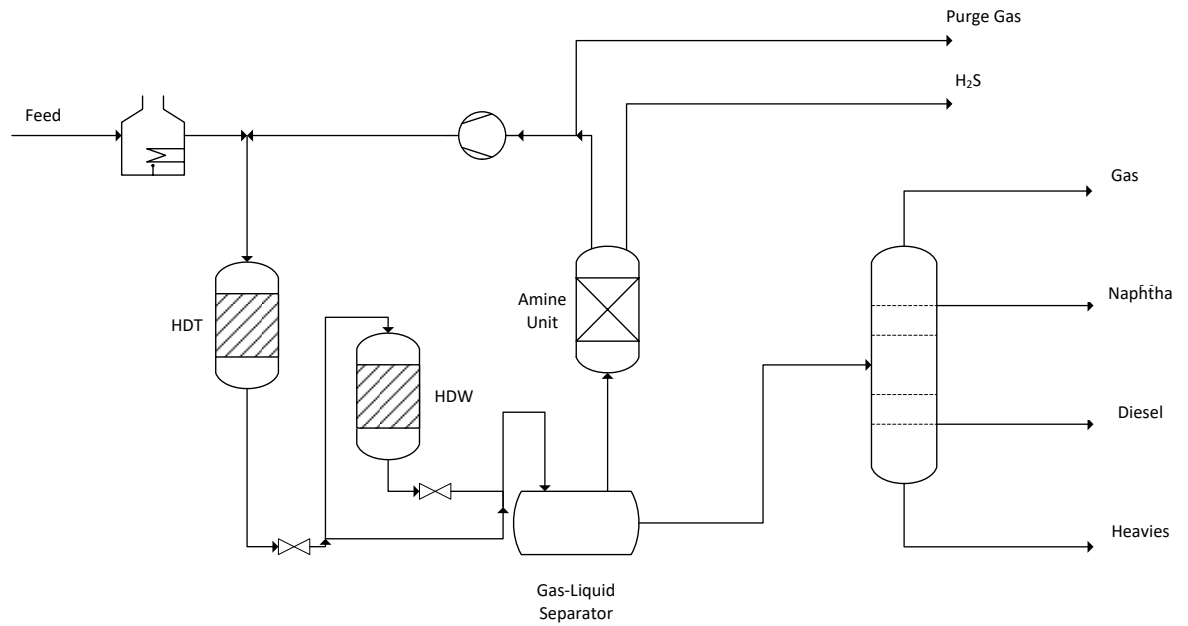


Figure 1-2: Hydrotreating and hydrodewaxing unit in series for seasonal operations [2]

The configuration shown in Figure 1-1 is usually implemented when there is an existing HDT unit available and shape-selective dewaxing catalyst is loaded as an additional bed. On the other hand, when the demand for diesel with improved cold flow properties is seasonal, i.e. only during winter, the configuration showed in Figure 1-2 is commonly implemented so that the outlet stream from the HDT reactor is by-passed to the hydrodewaxing unit when it is necessary.

The most common operating condition ranges and types of feedstock used for industrial catalytic dewaxing operations have been presented by Rakoczy and Morse (2013), which shown in Table 1-2.

Table 1-2: Common ranges for operating conditions and feedstock specifications for industrial catalytic dewaxing reactors integrated to hydrotreating units [2]

Applicable feedstocks	LGO, HGO, VGO, VBGO, LCGO, HCGO, CGO
Operating pressure (bar)	30-150
LHSV according to cold-flow improvement service (h⁻¹)	0.5-8
Tolerance to sulfur (wt%)	< 2.5
Tolerance to basic nitrogen (wt-ppm)	< 1000
Regenerability	Yes (in-situ and ex-situ)
Presulfiding	According to HDS catalyst procedure
Production: Light hydrocarbons (%wt)	0.5-5

Naphtha (%wt)	1-15
Diesel (%wt)	80-99

1.1. Motivation of the Research

In the oil refining context, the impact of wax formation is usually felt by the final consumer due to the winter fuel performance. Novel technologies in conventional hydrocracking units have been developed along the years to break down the molecules in heavy crudes and produce as much diesel and gasoline as possible for a given crude throughput capacity. However, the concentration of heavy paraffinic compounds in the product fuel can still be high enough to promote wax formation when used in automobiles during the winter season. As previously mentioned, the catalytic dewaxing unit is the most promising technology emerged to improve the cold flow properties of diesel fuels through cracking and isomerization reactions on shape-selective zeolites [2]. A process model based on the conservation laws (mass, energy, and momentum) for this reactor can assist oil refineries to quickly design, scale-up, and optimize the operation without disturbing the physical process or depending on pilot units, which would lead to economic losses or compromise the plant integrity due to the process excitation.

In order to solve the material and energy balances, a kinetic model must be developed to predict the rate at which species are consumed or produced by the chemical reactions. Currently, most of the kinetic models available for shape-selective catalysts are found for Pt/ZSM-22 catalyst while no information is available for the commercial Pt/ZSM-5, which

is commonly used in industrial catalytic dewaxing processes. From experimental data obtained from a pilot reactor, the kinetic parameters can be estimated through optimization techniques developed for nonlinear regression purposes.

As petroleum feedstocks are complex mixtures involving thousands of hydrocarbons, a large number of kinetic parameters would need to be estimated if the complete reaction mechanism was taken into consideration by the kinetic model [3]. To overcome this problem, refinery reactor models use lumping techniques, which split the True Boiling Point (TBP) curve into single pseudo-components representing common petroleum cuts to reduce number of kinetic parameters [3]. However, the chemistry behind the actual process is lost and the parameters have to be re-estimated either when the feedstock is changed or during scale-up as the hydrodynamics of industrial reactors are more complex than that observed for pilot ones.

Considering those limitations, a mechanistic kinetic model was proposed by Froment and co-workers based on the single event theory. According to this methodology, the rate constants are formulated based on the statistical thermodynamics and quantum chemistry, which allow to factor out the effects of the molecular structure of reactants and activated complexes on the rate parameters by introducing the number of single events. The carbenium ion chemistry can be incorporated to model by using the reaction network algorithm proposed by Clymans and Froment (1985) and Baltanas and Froment (1985), which generates all possible elementary steps taking place on bifunctional catalysts. These catalysts contain metal sites responsible for the dehydrogenation/hydrogenation steps and acidic ones on which isomerization and cracking reactions occur. However, as the number of molecules involved in the reaction mechanism is extremely large, the posteriori-lumping

technique proposed by Vynckier and Froment (1991) is used to keep the number of kinetics parameters small. In this technique, thermodynamic equilibrium is assumed to obtain the composition distribution for the individual components within the lump. The main advantage in using this type of kinetic model is that the single-event rate constants are independent on the nature of feedstock and can be applied to design any kind of hydrocracking reactor [7]. There are no publications found so far applying such mechanistic model to simulate industrial hydrodewaxing reactors.

To characterize the cold flow properties of diesel fuels, the cloud point temperature is extensively used [2]. This property is defined as the highest temperature at which the first wax crystal forms in the fuel [2]. The measurement is commonly through visual techniques defined by the standard ASTM D2500. The uncertainties introduced due to operator's visual capability and the time required to collect the measurements could cause a negative impact on the control system design for the reactor unit due to large time delays. As an alternative, a reactor model to quickly and accurately predict the cloud point values while waiving the dependence on visual measurements would be beneficial. Current publications have shown that the solid-liquid equilibrium (SLE) theory can be used to estimate the cloud point of hydrocarbon mixtures with good accuracy. Therefore, integrating a mechanistic reactor model to the solid-liquid equilibrium one would provide a simple way to develop a soft-sensor to predict on-line the product cloud point from the knowledge of the reactor operating conditions and feedstock distillation data during the catalytic dewaxing operation. Such application has not been reported in literature and is going to be explored in this thesis.

1.2. Objectives

The objectives of this thesis can be summarized as follows:

- i. Develop a mechanistic single-event kinetic model to simulate catalytic dewaxing reactor operation. This technique eliminates the dependence of the kinetic parameters on the feedstock type and reactor hydrodynamics found in most conventional lumping approaches;
- ii. Estimate the feedstock independent single-event rate constants using experimental data for hydrodewaxing of n-hexadecane on Pt/ZSM-5 catalyst. All rate-limiting elementary steps involved in the process were obtained using a reaction network algorithm.
- iii. Propose a soft-sensor by coupling the developed catalytic dewaxing reactor model to a Solid-Liquid Equilibrium (SLE) flash algorithm to predict the cloud point of the dewaxed diesel product. The hydrodesulfurization effects were also included in order to show the application of the model to industrial operations.
- iv. Develop a surrogate model to eliminate the dependence of the cloud point prediction on solving the mechanistic reactor models, which are computationally expensive and have complex mathematical formulation. A sequential design strategy for computer experiments that applies concepts from Fuzzy logic, Voronoi tessellation, and Local Linear Approximation (LOLA) theories was implemented so that nonlinear effects on the accuracy of the surrogate model could be handled.

1.3. Organization of the Thesis

The manuscript format was adopted to write this thesis. An outline of each chapter is provided as follows:

In Chapter 1, the catalytic dewaxing process is introduced and the issues related to the cloud point measurements of diesel fuels are highlighted. The motivation and objectives for this research are also discussed.

In Chapter 2, a literature review covering all existing techniques to model conventional hydrocracking reactors and kinetic models developed for shape-selective hydrocracking and hydroisomerization are discussed as they are the core to understand the reaction mechanisms taking place in catalytic dewaxing reactors.

In Chapter 3, a single event kinetic model is developed for catalytic dewaxing on Pt/ZSM-5. As the kinetic parameters derived from the single event theory do not depend on the feedstock type, experimental data for hydroconversion of n-hexadecane in a tubular reactor was adopted for the parameter estimation. Finally, a sensitivity analysis study is made through reactor simulations to understand the effect of the main process variables on the reactor performance. This chapter was submitted to the Industrial & Engineering Chemistry Research journal.

In Chapter 4, a soft-sensor is developed to perform on-line cloud point predictions during industrial operation of catalytic dewaxing reactors. The sensor framework was built using three modules involving mechanistic reactor and thermodynamic models to estimate the cloud point of diesel product. The computing time and complexity of the sensor were reduced by proposing a surrogate model to replace the mechanistic ones using a sequential

design strategy capable of tracking nonlinearities in the cloud point response to improve its accuracy. This chapter was submitted to the Chemical Engineering Science journal.

In Chapter 5, the conclusions highlighting the main contributions of this thesis and recommendations for future works in this field of study are provided.

Chapter 2

Literature Review

2.1. Preface

In this section, a brief literature review is provided regarding to existing kinetic and reactor modelling techniques for both conventional and shape-selective hydrocracking processes. Also, the current application of thermodynamic models to predict the cloud point of hydrocarbon mixtures are discussed. The objective is to give an insight on the ongoing research being carried out in this field as well as justify the contributions of this work.

Catalytic dewaxing reactors are important units in petroleum refineries that can replace the conventional solvent dewaxing procedures when attempting to reduce the cloud point of diesel fuels without major yield losses [2]. However, the availability of kinetic and process modelling studies related to those units are still scarce and limits the knowledge about the reaction mechanisms governing the process as well as increases the need for expensive pilot units to assist in the process design and optimization steps. Although solid-liquid thermodynamic models have been extensively applied to predict the cloud point of diesel fuels, they have not been yet incorporated to reactor models capable of simulating the full unit operation. Such integrated model would be beneficial to petroleum refineries in the aspect that they can replace the highly inaccurate practices currently in place to measure and control the cloud point of the product fuel.

2.2. Kinetic Modelling for Conventional Hydrocracking Reactors

Qader and Hill (1969) proposed the first lumped kinetic model reported for Vacuum Gas Oil (VGO) hydrocracking that uses pseudo-components representing the most common boiling point cuts such as gasoline, middle distillate, and diesel. Only one reaction was considered to represent the conversion of VGO to the products and a first order kinetic model with respect to the feed concentration was proposed. Callejas and Martínéz (1999) formulated a three-lump kinetic model for Maya residue hydrocracking, which the reaction network considered first order reactions converting the feedstock into lumps representing light oils and gases. Sánchez et al. (2005) introduced a 5-lump kinetic model for hydrocracking of heavy oils considering first order reactions involving 5 lumps: unconverted residue, vacuum gas oil, distillates, naphtha, and gases. For all these approaches, the parameter estimation was made through minimization of sum of square errors between the measured and predicted values for lump compositions considering first order reactions.

The main disadvantage of these kinetic models is related to their dependence on the nature of feedstock and, therefore, re-estimation of the kinetic parameters is necessary when the feedstock is changed [7]. Furthermore, the number of kinetic parameters quickly increases as more lumps are added to the kinetic model for accuracy purposes [11].

Another technique available in the literature to model the kinetics of hydrocracking of complex feedstocks is the continuum lumping technique, which considers the reaction mixture as continuous with respect to the boiling point and molecular weight. This technique was developed by Laxminarasimham et al. (1996) and the proposed kinetic

model depends on the estimation of a characterization parameter from the TBP curve. The material balances and kinetic model are function of the reactivity of each component in the feedstock and are represented by an integro-differential equation. Even though, this methodology requires less parameters, the chemistry of the process is still not taken into consideration in its formulation [7].

Baltanas et al. (1989) proposed a fundamental kinetic model for hydroisomerization of n-octanes into monomethylheptanes on Pt/USY zeolites. The reaction network was built through a computer algorithm proposed by Clymans and Froment (1984) and Baltanas and Froment (1985). The ideal hydrocracking process was assumed by considering the rate-determining steps as those taking place at the acid sites of the catalyst such as the PCP-isomerization and β -scission cracking reactions. A total of 12 feedstock independent single event kinetic parameters were estimated from experimental data for gas hydrocracking taking place in a Berty-type reactor. The results showed very good agreement between experimental and calculated values for rate of formation.

Svoboda et al. (1995) estimated the single event kinetic parameters for hydroisomerization and hydrocracking of paraffins on Pt/US-Y zeolite in gas phase considering ideal hydrocracking conditions. The reaction network was generated through a computer algorithm proposed by Clymans and Froment (1989). A total of 22 reaction Arrhenius parameters were estimated from experimental reaction rate values for pure n-octane feedstock. It was the first published work after Baltanas et al. (1989) that considered the formation of multibranched paraffins. The reaction network was generated using the previously algorithm and thermodynamic constraints were further incorporated to the model formulation to further reduce the number of kinetic parameters. A total of 22 single

event rate constants were estimated from wide range of feedstocks, which their dependence on the feed were proved to be statistically nonsignificant through the validation steps comparing the experimental and calculated effluent mole flow rates.

Schweitzer et al. (1999) applied the single event kinetics to model the hydrocracking of paraffins taking place in a three-phase reactor operating in trickle flow. In their work, all the elementary steps in metal and acid sites were included in the parameter estimation. The reaction network generation considered not only the formation of PCP but also the protonated cyclobutane (PCB) intermediate structures. Twelve single event parameters and four Langmuir adsorption coefficients were estimated from experimental values for cracking yields, selectivities, and molar distribution for a feedstock consisting of pure n-hexadecane. The vaporization of the liquid phase along the reactor was also taken into account. The estimated kinetic parameters were used to simulate the hydrocracking of a Fisher-Tropsch effluent containing paraffins within the C₁₁-C₁₈ range, which good predictions were reported. However, diffusional limitations in the experimental reactor were detected as the calculated outlet mole fractions for monoparaffins were considerably deviated from the measured values.

Kumar and Froment (2007) applied the single event kinetic model to study the non-ideal hydrocracking of long-chain paraffins taking place in a trickle bed reactor. The feedstock considered for parameter estimation involved heavy paraffinic molecules up to C₃₂. The reaction mechanism was proposed based on the carbenium ion chemistry and the elementary steps were obtained through an improved reaction network algorithm. The rate of formation of the intermediate olefins at the metal sites was formulated based the molecular dehydrogenation/hydrogenation mechanisms. To further reduce the number of

kinetic parameters related to the dehydrogenation steps, the activation energy was assumed to be dependent on the nature of the carbons forming the double bond, which led to five activation energies and one frequency factor to be estimated. Moreover, the surface of the catalyst was considered to be entirely surrounded by the liquid phase. To account for the effect of the carbenium ions on the activation energy, the free-energy linear relation of Evan-Polanyi was adopted. The posteriori-lumping technique was used and the net rate of formation was expressed in terms of lumps selected based on carbon number and degree of branching. A total of 14 parameters were estimated from experimental data obtained from a tubular reactor using n-hexadecane. The authors studied the effects of the catalyst activity on the product distribution through reactor simulations and found out that as farther from the equilibrium the metal site elementary steps are, the cracking steps are favoured once olefins are hydrogenated at low rates.

The single event kinetic modeling has been extensively applied to simulate and optimize other types of refining processes such as catalytic cracking in riser reactors [16], alkylation [17, 18], and methanol-to-olefins [19, 20], which proves its efficiency and applicability. However, no application has been reported yet for the catalytic dewaxing reactor.

2.3. Kinetic Modelling for Shape-Selective Hydrocracking and Hydroisomerization Processes

The main difference between conventional hydrocracking and hydrodewaxing processes is in the type of catalyst used. Conventional hydrocracking uses wide-pore zeolites that allow

all molecules in the reaction mixture to access the acid sites [21]. Therefore, after the isomerization reactions achieve significant extent of reaction, the cracking reactions dominate the hydrocracking process to decrease the average molecular weight of overall mixture [21].

Hydrodewaxing processes apply shape-selective catalysts in which the ability of the reactant molecules to reach an acid site in the zeolite crystal depends on the shape and size of the reactant, product, or activated complex molecular structures [21]. The most accepted theories to explain the shape-selectivity effects are formulated based on the pore-mouth and key-lock mechanisms [22].

Both mechanisms have been intensively adopted to formulate kinetic models for hydroconversion of n-alkanes on Pt/H-ZSM-22 [22, 23]. According to the pore-mouth mechanism, the physisorption mode of the intermediate olefins attempting to reach an acid sites determines whether acid-catalyzed reactions such as protonation, cracking and isomerization are going to take place [22]. Normal paraffins have straight carbon chains and are entirely physisorbed into the micro-pores of the zeolite crystal. On the other hand, branched paraffins only have one of its straight-ends allowed to enter the catalyst pore-mouth as methyl branches are blocked [22]. Therefore, substituted carbenium ions are only formed at the pore mouth for a given physisorption mode that allows the entire double bond of the resulting olefin to chemisorb at the acid site [22]. For wide pore catalysts, such as US-Y zeolites, the protonation reactions are competitive as a particular acid site can be accessed by any olefinic compound in the mixture; however, for shape-selective catalysts, these reactions are non-competitive because the site can only be accessed by the particular branched olefin sorbed at that location [22]. This mechanism explains the high yield of

monobranched paraffins with the methyl group located close to one of extremes at the main carbon chain [21].

The key-lock mechanism is used to explain the increase in the yield of dimethyl isomers as the size of the reactant carbon chain increases. According to this theory, a long carbon chain is stretched and the two straight-ends are physisorbed simultaneously at adjacent pore-mouths [22]. The existence of this mechanism is proved from the observed formation of monobranched paraffinic molecules with a methyl group occupying a central position at the main chain or dimethyl isomers with groups spaced by two or three carbon atoms [21]. It is important to mention that geminal or vicinal dibranched paraffins, which have two methyl groups connected to the same carbon atom, are not formed as they are sterically hindered at the pore-mouth [22].

Laxmi Narasimhan et al. (2004) studied the pore-mouth catalysis in hydroconversion of n-octane on Pt-H-ZSM-22 shape-selective catalysts. According to the authors, only part of the carbon chain of branched paraffins can be allowed into the pore-mouth, where the typical acid-catalyzed reactions take place. They proposed a single event kinetic model in order to compare the kinetic parameters to those obtained for wide-pore zeolites such as Pt/US-Y. Experimental data for vapor phase hydrocracking of n-octane were collected in a tubular reactor. They observed that the selectivity of monobranched paraffins decreases as the methyl group moves towards the middle of the main chain and small selectivity for dibranched paraffins was also detected. The rate-determining steps were considered to be PCP isomerization and β -scission cracking steps with dehydrogenation/hydrogenation reactions in pseudo-equilibrium. According to the authors, the kinetic model must take into consideration the modes of physisorption as the normal paraffins are fully admitted into the

micro-pores while only part of the branching or main chain of substituted alkanes can penetrate into the pore mouth. Also, enthalpy and entropy losses regarding to the transport of the species to the bulk of the micro-pore was identified as the main reason that physisorption is an important step in the hydroconversion on shape-selective catalysts. Due to the size and shape constraints, the elementary steps forming and consuming tertiary and quaternary carbenium ions were excluded from the reaction network once they cannot reach the acid sites at the pore mouth. The parameter estimation provided the difference in activation energies between ZSM-22 and US-Y zeolites and the frequency factor was obtained from the literature. The parameters were obtained by considering the activation energy dependent on the reactant family leading to good agreement with experimental data for the yield of cracking products. It was also reported that shape-selective catalysis promotes high selectivity for isomerization and very low selectivity for cracking products as most of the multibranched carbenium ions are not allowed to be formed in such catalysts. According to the single-event microkinetic model for hydroconversion of n-octane on Pt/H-ZSM-22 developed by Laxmi Narasimham et al (2004), the protonation/deprotonation equilibrium constant was the term in their rate expression that introduced the effect of the shape-selectivity nature of the catalyst on the kinetic model.

However, these kinetic studies were focused on the catalyst design and a more complex methodology was adopted to estimate the kinetic parameters.

Vandegheuchte et al. (2014a) studied the hydroconversion of n-hexane on Pt/ZSM-5. The main objective was to identify the most important shape-selectivity mechanism among diffusion limitation, transition state shape selectivity, and physisorption selectivity affecting the conversion process. To carry out this analysis, a single event microkinetic

model was developed using experimental data for outlet product compositions collected in a Berty-type continuous stirred tank reactor (CSTR). The authors divided the parameters of the rate equation into two categories. The “kinetic descriptors” are the single event frequency factors and activation energies whose values were taken from literature data for Pt/US-Y catalysts. The “catalyst descriptors” were defined as those parameters that characterizes the nature of the catalyst such as Langmuir adsorption coefficients, physisorption saturation concentration, total acid site concentration, and protonation equilibrium coefficient. The prior was formulated using the Van’t Hoff’s law and the main parameters to be estimated were the standard heat of protonation values for each reactant and product in the reaction network. Their results revealed that the intracrystalline diffusion limitation was the main shape selectivity effect in Pt/ZSM-5 that could accurately explain the higher selectivity towards 2-methyl-branched compared to 3-methyl-branched alkanes observed experimentally. That effect was incorporated to the reactor model by solving a reaction-diffusion problem using the Fick’s law. However, it was shown that the diffusion coefficient is a strong function of the pore occupancy due to peculiar pore structure of Pt/ZSM-5 catalyst, which characterizes the so-called “configurational diffusion” and cannot be estimated from conventional methods. To overcome this problem, the diffusivity was written in terms of a corrected diffusion coefficient that was assumed to be a linear function of the pore occupancy as interspecies correlation effects were neglected. Finally, when regression was made considering the transition-state shape selectivity or physisorption selectivity effects, the results showed that the regression either led to poor fitting to describe composition distribution for the monobranched paraffins or led to non-realistic values of standard heat of protonation. In their later work, Vandegheuchte et al.

(2014b) improved their results by considering the interspecies correlation effects into the corrected diffusion coefficient formulation.

Although the study conducted by Vandegehuchte et al. (2014a) provided significant insight to better understand the hydroconversion process on Pt/ZSM-5 catalysts, some features in their model would not allow its application to design and simulate a catalytic dewaxing reactor. Due to the small size of the reaction network generated for n-hexane, the Langmuir adsorption coefficients as well as single event frequency factors can be easily estimated from available literature data for standard entropy of formation and physisorption for the few individual compounds found in the product. For heavy paraffinic feedstocks, such as n-hexadecane, the spectrum of hydrocarbons existing in the reaction mixture is significantly larger and it is possible that thermodynamic data for standard entropy of physisorption would not be available for some of the carbenium ions found in the reaction network. Also, the values of saturation physisorption concentration and total concentration of acid sites considered by the authors were taken from literature data for a silicate catalyst with similar Si/Al ratio used in their work. If the catalyst characterized by different value of Si/Al ratio is used in the industrial operation, those concentration values would significantly change and finding information for similar catalyst in the literature would be time consuming and difficult. Finally, the values of single event activation energy were not estimated but assumed to be the same as those obtained Pt/US-Y zeolites, which are non-shape selective catalysts. This assumption may not be valid for the hydroconversion of heavy paraffins as the key-lock shape selective mechanism, which is not observed in the hydroconversion of small alkanes, would play an important role on the conversion process as these molecules can stretch and adsorb at two adjacent pore-mouths.

2.4. Cloud Point Estimation

Another challenge faced when designing catalytic dewaxing units is related to cloud point measurements for product fuel. The most used analytical procedure is established by the standard ASTM D2500, which consists on a visual methodology and it is subjected to several sources of error due to its dependence on the operator's visual skills. This problem can be overcome by applying the solid-liquid thermodynamic models formulated in the field of reservoir engineering in the recent years.

Pedersen (1995) proposed a vapor-liquid-solid thermodynamic model to predict the phase equilibria including the possible formation of a wax phase. The liquid phase was described using a fugacity coefficient evaluated using an equation of state such as Peng-Robinson. The fugacity of a component in the solid phase was expressed in terms of its fugacity in liquid phase for a standard state and fusion properties. Due to the complexity of the oil mixture analyzed, the plus-fraction lumping technique was used so that hydrocarbons containing more than seven carbons in their structure were grouped into a single lump. It was also considered that not all the lumped molecules would be present in the solid phase aromatics and highly branched paraffins have different solidification processes compared to those for normal paraffins. Therefore, the plus-fraction lump was split in two parcels: wax forming and non-wax forming fractions. In order to obtain the physical properties necessary to solve the equation of state, the wax forming fraction was divided into pseudo-component where mole fraction distribution was calculated based on an empirical equation whose parameters were estimated using experimental mole composition distribution from oil samples taken from several wells. The non-waxing components were avoided in the solid phase by setting

their fugacities to infinity. The predicted cloud point was in well agreement with the measured values; however, the model was limited to the parameter estimation used to characterize the plus-fraction lump.

Coutinho and Ruffier-Meray (1997) studied the solid-liquid region of heavy paraffinic solutions ranging from C₁₉ to C₄₈ dissolved in ethylbenzene by experimental means such as DSC to detect different solid phases and chromatography to measure the compositions of species in the liquid phase. They also studied the effect of aromatics on the wax formation and a thermodynamic model was proposed to predict the measured results. The model was formulated by combining the Flory-free-volume equation and UNIFAC to describe the behavior of the liquid phase and predictive Wilson to model the solid phase. They observed from the experiments that the amount of the heaviest normal paraffins in the solid phase quickly increased as temperature dropped compared to light normal alkanes. Also, it was found that the aromatic species have no influence on the paraffinic solidification. The main advantage in using these models is related to the fact that there are no empirical parameters in their formulation and they only depend on physical properties of the pure components in mixture. The predictions were shown to be in agreement with the experimental results for cloud point for the mixtures tested. Another contribution from this work was the identification of an azeotrope-like behavior for the solid phase. It was also identified the limitations of the thermodynamic model proposed. According to the authors, the predictive Wilson is not capable of describing solutions forming multiple solid phases in terms of composition. However, the cloud point was well predicted once it is only dependent on the behavior of the heaviest molecules in the mixture.

Coutinho (2000) proposed a thermodynamic model that overcomes the limitations in describing the solid phase encountered in previous methodologies and correlations. His model considered the UNIQUAC model to describe the solid phase and assumed normal paraffins. Experimental data for four jet fuels, two ship propulsion distillate fuels, and three types of diesel fuels were used to validate the thermodynamic model. Isoparaffins, aromatics, and naphthenes were lumped into a single pseudo-component based on the assumption that PNA (Paraffin-Naphthenic-Aromatic) distribution or any other physical property for the fuel was known. The author showed that the measured and calculated solid and liquid compositions were in excellent agreement for all fuels. It was also reported that when the fuel is mainly constituted by small paraffinic molecules, a correction of 3% must be applied to the interaction term in the thermodynamic model so that the end-effect interactions can be taken into account. Another finding was that the results were independent on the use of pseudo-components to represent the aromatic, naphthenic, and branched paraffinic species due to the high solubility of n-alkanes on those components. The predicted cloud point values were also found in excellent agreement with the experimental values obtained through either ASTM 2386-67 or DSC depending on the nature of the fuel.

Ghanaei et al. (2007) formulated a thermodynamic model to predict the wax formation considering the liquid phase as an ideal solution and the solid phase described by using the predictive Wilson model. The model was extended so that the effect of high pressure could be also accounted by using the Poynting correction, which is dependent on fusion temperatures evaluated at atmospheric pressures. This overcomes an issue faced by older models, which considers the solid and liquid phases as incompressible. The model was

validated using experimental data for cloud point using binary mixtures consisting of C₁₄-C₁₅ and C₁₄-C₁₆ for different pressures ranging from 0.1 to 100 MPa and very good agreement was reported. It was also showed to be superior to other models that are based on equation of state or multi-solid phase solution.

Although these thermodynamic models showed good accuracy in predicting the cloud point of hydrocarbon mixtures and fuels, they have not been formulated and applied in a way that they can be used to perform on-line predictions when operating industrial catalytic dewaxing units. In this work, a thermodynamic model formulated based on the UNIFAC and Wilson models to describe the liquid and solid phases, respectively, is applied to compute the cloud point of the diesel product based on the simulated outlet compositions obtained from the catalytic dewaxing reactor model.

Chapter 3

Single Event Kinetic Modelling of Catalytic Dewaxing on Commercial Pt/ZSM-5

Eugenio Turco Neto, Syed Imtiaz, Salim Ahmed

Center for Risk, Integrity and Safety Engineering Group
Department of Process Engineering
Memorial University of Newfoundland, NL, St. John's, A1B 3X5, Canada.

3.1. Preface

This manuscript was submitted to the Industrial & Engineering Chemistry Research in February 2017. The co-author Dr. Salim Ahmed supervised the principal author Eugenio Turco Neto in assessing the best optimization algorithm to obtain the kinetic parameters. The corresponding author Dr. Syed Imtiaz supervised the main author of this work and provided all necessary knowledge to support the main author and co-author.

3.2. Introduction

High concentration of long-chain paraffins in diesel fuels have been a major concern for oil refineries located in countries with harsh winter seasons. Due to their high fusion temperatures, the fuel can crystallize even when exposed to moderate positive temperatures, which leads to wax formation in automotive filters. To overcome this problem, Exxon Mobil created a new technological process similar to hydrocracking in 1970 called catalytic dewaxing, which uses bifunctional shape-selective catalysts such as

Pt/ZSM-5 to convert heavy paraffinic molecules through selective isomerization and cracking reactions carried out in trickle bed reactors [1]. In order to assess the performance of this process, the cloud point, which is the highest temperature at which the first wax crystal appears in the fuel, is the common metric used in industry to determine if the fuel cold flow specifications have been met [2]. There are strong evidences that by increasing the dewaxing conversion, the cloud point of the diesel product is reduced; however, high yield losses are observed due to the higher selectivity towards cracking products [1].

In order to optimize and design a catalytic dewaxing reactor for industrial purposes, a kinetic model is necessary to predict the net rate of consumption for the heavy paraffinic components in a given diesel feedstock so that the continuity and energy equations can be solved. However, diesel is a complex mixture of hydrocarbons and a reactor model that includes all the reactions would require a prohibitive number of kinetic parameters to be estimated [3]. To overcome this problem, refinery reactor models use lumping techniques, which split the True Boiling Point (TBP) curve into pseudo-components representing common petroleum cuts so that the complexity of the mixture as well as the number of kinetic parameters are reduced [3]. Qader and Hill (1969) proposed the first lumped kinetic model reported for Vacuum Gas Oil (VGO) hydrocracking using the most common boiling point cuts such as gasoline, middle distillate, and diesel as pseudo-components. Only one reaction was considered to represent the conversion of VGO and a first-order kinetic model with respect to the feed concentration was proposed. Callejas and Martinez (1969) formulated a three-lump kinetic model for Maya residue hydrocracking considering first-order reactions converting the feedstock into lumps representing light oils and gases. Sánchez et al. (2005) introduced a 5-lump kinetic model for hydrocracking of heavy oils

using first-order kinetics and 5 pseudocomponents: unconverted residue, vacuum gas oil, distillates, naphtha, and gases.

Even though the previous models are simple and can be easily implemented, their main disadvantage is related to their dependence on the feedstock composition. Therefore, a re-estimation of the kinetic parameters is necessary when the feedstock is changed [7]. Moreover, the number of kinetic parameters quickly increases as more lumps are added to the kinetic model for better accuracy [7].

Another type of kinetic model available in the literature suitable to describe the hydrocracking of complex feedstocks is the continuum lumping technique, which considers the reaction mixture continuous with respect to the boiling point and molecular weight. This technique was developed by Laxminarasimham et al. (1996) and the proposed kinetic model depends on the estimation of a characterization parameter from the feedstock TBP curve. It is also assumed that the material balances and kinetic model are functions of the reactivity of each component in the feedstock, which are represented by integro-differential equations. Even though, this methodology involves less parameters to be estimated, the chemistry of the process is still not taken into consideration [7].

A mechanistic kinetic model for hydrocracking and hydroisomerization was introduced by Froment and co-workers based on the single event theory. According to this methodology, the rate constants are formulated based on the statistical thermodynamics and quantum chemistry allowing the effects of the molecular structure of reactant and activated complex to be factored out by introducing the number of single events in the rate constant formulation. The carbenium ion chemistry is incorporated to the kinetic model by using a computer reaction network algorithm proposed by Clymans and Froment (1984) and

Baltanas and Froment (1985) that generates all possible elementary steps commonly taking place on bifunctional catalysts. These catalysts are constituted by metal and acid sites responsible by hydrogenation/dehydrogenation and cracking/isomerization reactions, respectively. The main advantage in using this type of kinetic model relies on the independence of the kinetic parameters on the feedstock type, which allows the application of the hydrocracking model to cases involving feedstocks from different sources.

Baltanas et al. (1989) developed a single event kinetic model to describe the hydroisomerization of n-octanes into monomethylheptanes on Pt/US-Y zeolites. A total of 12 feedstock independent kinetic parameters were estimated from experimental data. Good agreement between experimental and predicted values of rate of formation for several products was reported. Svoboda et al. (1995) extended the previous single event kinetic model proposed by Baltanas et al. (1989) by considering the formation of multibranched paraffins. A total of 22 single event kinetic parameters were estimated for a wide range of feedstocks, which the results showed that the feedstock influence on those parameters were statistically nonsignificant.

Schweitzer et al. (1999) applied the single event kinetic modelling to simulate the hydroconversion of paraffinic feedstocks in a trickle bed reactor. A total of 12 single event rate constants and 4 Langmuir adsorption coefficients were estimated from experimental data for yields, selectivity, and product mole distribution considering n-hexadecane as feedstock. The model showed to be suitable to describe the hydroconversion of n-hexadecane as well as the hydroconversion of a Fischer-Tropsch effluent containing paraffins within C₁₁-C₁₈ range.

Kumar and Froment (2007) developed a single event kinetic model to analyze the hydroconversion of heavy paraffins up to C₃₂ when the catalyst is not properly loaded with metal sites. A total of 14 single event Arrhenius parameters were estimated from experimental data. The authors showed that product distribution drastically changes for catalysts consisted of weak metal sites as the quasi-equilibrium assumption regarding the hydrogenation and dehydrogenations steps is no longer valid.

Finally, Vandegehutche et al. (2014a) applied a single event microkinetic model to identify the most important shape selectivity effects on the hydroconversion of n-hexane on Pt/ZSM-5. The results have shown that the intracrystalline diffusion limitation within the catalyst particle was the main mechanism governing the shape selectivity affecting the product distribution and accurately described the higher selectivity toward 2-methyl-branched compared to 3-methyl-branched alkanes. Moreover, the Fick's diffusion coefficients had to be reformulated as the diffusion mechanism are strongly affected by the pore occupancy within the catalyst. To overcome this problem, the authors proposed initially a mean-field model that considers the diffusion coefficients as linear function of the pore occupancy, which introduced few parameters to estimated. This approach was later improved by Vandegehutche et al. (2014b) by taking into account the interspecies correlation in the diffusion coefficient formulation.

The single event kinetic modeling has been extensively applied to simulate and optimize other types of refining processes such as catalytic cracking in riser reactors [16], alkylation [17, 18], and Methanol-to-Olefins process [19, 20], which proves its efficiency and applicability; however, no studies using such mechanistic concept have been applied to model industrial catalytic dewaxing reactors.

In this work, a single event kinetic modeling approach developed to describe the selective isomerization and cracking reactions carried out on a catalytic dewaxing bed loaded with commercial shape-selective Pt/ZSM-5. The feedstock independent single-event rate constants were estimated using experimental data for the hydroconversion of n-hexadecane. Finally, reactor simulations were carried out for different operating conditions and feedstocks to study their effect on the reactor performance.

3.3. Reactor Modeling

3.3.1. Shape-Selectivity Effects

The main difference between the conventional hydrocracking and hydrodewaxing processes relies on the type of catalyst used. Conventional hydrocracking reactors use wide-pore zeolite catalysts on which all molecules in the reaction mixture have an equal probability to occupy a given acid site [21]. It is also necessary that the isomerization reactions achieve a certain conversion before the cracking elementary steps take place [21]. Shape-selective catalysts are used in catalytic dewaxing units and the ability of the reactant molecules to reach an acid site in the zeolite crystal depends on the shape and size of its molecular structure [21]. The most accepted theory used to explain the shape-selectivity promoted by this type of catalyst is based on the pore-mouth and key-lock mechanisms [22].

Both mechanisms have been used to develop kinetic models to describe the hydroconversion of n-alkanes on Pt/H-ZSM-22 [22, 30, 31]. In the pore-mouth mechanism,

the physisorption mode of the intermediate olefins attempting to reach the acid sites determines whether acid-catalyzed reactions such as protonation, cracking and isomerization are going to take place [22]. As normal alkanes are straight carbon chains, these molecules form olefins that are entirely physisorbed into the micropore of the zeolite crystal without any sterical hindrance. However, only one of straight-ends of the branched olefin can sorb into the pore-mouth once the methyl branches block their full entrance into the pore [22]. Therefore, branched carbenium ions are only formed at the pore mouth for a given physisorption mode that allows the entire double bond to chemisorb at an acid site [22].

For US-Y zeolites, the protonation reactions are competitive as molecules can access the acid sites; however, in shape-selective catalysts, these reactions are non-competitive because the acid site located at the pore-mouth can only be accessed by the specific olefin sorbed at that location [22]. This mechanism explains the high yield of monobranched paraffins with a methyl group located at one of extremes in main carbon chain when shape-selective zeolites are used [21].

The key-lock mechanism is used to explain the increase in the yield of dimethyl isomers as the size of the reactant main carbon chain increases. According to this theory, the carbon chain is stretched and two straight-ends are simultaneously physisorbed at adjacent pore-mouths [22]. The experimental evidence confirming the existence of such mechanism lies on the formation of monobranched paraffinic molecules with a methyl group occupying a central position in the main chain and dimethyl isomers with methyl branches spaced by two or three carbon atoms [21]. It is important to mention that geminal or vicinal dibranched paraffins are not formed due to steric hindrance effects. Furthermore, tribranched

carbenium ions are not considered in hydroconversion on shape selective catalysts due to their shape and size constraints [23].

In the single event microkinetic model developed by Laxmin Narasimham et al. (2003) to describe the hydroconversion of n-octane on Pt/H-ZSM-22, the deprotonation/protonation equilibrium constant is the term in the rate expression that determines shape-selectivity effects to the kinetic model. Hence, the single-event kinetic parameters available in the literature for Pt/US-Y zeolites cannot be used to model catalytic dewaxing reactors and they must be re-estimated.

Therefore, due to the pore size constraints found in Pt/ZSM-5 catalysts, less reactions are allowed to take place when compared to those in Pt/US-Y catalysts. Laxmin Narasimham et al. (2003) suggested that some further assumptions must be made to incorporate the shape selectivity effects when building the reaction network, which are listed as follows:

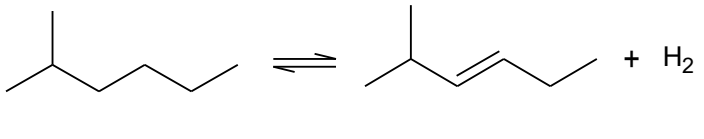
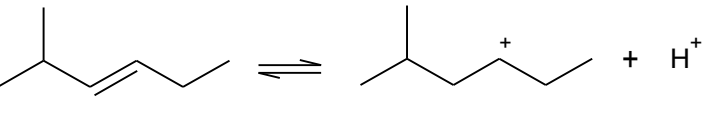
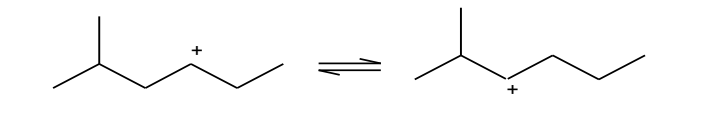
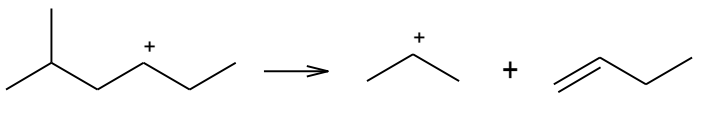
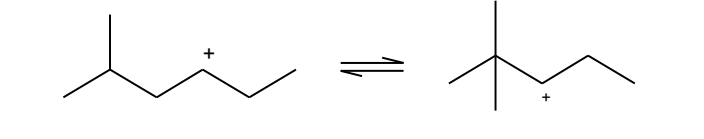
- Elementary steps involving tertiary carbenium ions, in which the carbon bearing the charge is tertiary, are fully suppressed due to the transitional-state shape selectivity effects [22];
- Methyl-shift reactions are not allowed to take place in shape selective catalysts due to steric hindrance effects [22];

3.3.2. Reaction Mechanism

As the Pt/ZSM-5 is a bifunctional catalyst, the reaction mechanism based on the carbenium ion chemistry can be used to describe the chemical phenomena involved in the catalytic

dewaxing process once it is a special case of hydrocracking. The common elementary steps taking place at both metal and acid sites on Pt/ZSM-5 catalysts are shown in Table 3-1.

Table 3-1: Assumed elementary steps promoted by metal and acid sites on Pt/ZSM-5

Dehydrogenation/Hydrogenation	
Protonation/Deprotonation	
Hydride shift	
β -scission	
PCP isomerization	

According to Kumar (2004) [32], the following assumptions can be made based on experimental evidences:

- Only methyl branches are considered and the maximum number of branches attached to the main chain is three;
- The carbenium ions are usually classified based on its stability. Hence, only elementary steps forming secondary carbenium ions, which the carbon bearing

the charge is secondary, are considered. Consequently, elementary reactions involving methyl and primary carbenium ions are excluded.

- The protonated cyclopropane (PCP) ring is the only intermediate structure considered to describe the isomerization steps;

If the catalyst particle is properly loaded with platinum, the elementary steps taking place at the metal sites reaches equilibrium and the rate-determining steps are fully located at the acid sites. Laxmin Narasimhan et al. (2003) showed that these assumptions are also valid for shape-selective catalysts, and thereby, it is going to be considered in this work. Also, the hydride-shift elementary steps are assumed to be in pseudo-equilibrium once they are faster than the PCP isomerization [32].

3.3.3. Reaction Network Generation

In this work, the reaction network was generated using the computer algorithm proposed by Baltanas and Froment (1985). Additionally, the shape-selectivity effects were incorporated by imposing the previously mentioned constraints suggested by Laxmin Narasimhan et al. (2003).

In order to build the reaction network, a computer representation for the hydrocarbons involved reaction mechanism is required. Boolean matrices are used in which each carbon-carbon bond in the molecular structure is represented by the number “1” (true) [5]. Also, the matrix must be unique for a given compound to prevent inconsistencies during the

network generation. Hence, the hydrocarbons must be labeled following a standard fashion to satisfy such condition [32]. In this work, the main chain is first enumerated from left to right end followed by the methyl branches. Then, the C-C bonds are identified to build the Boolean matrix for the molecule. This procedure is illustrated in Figure 3-1 for the carbenium ion 2-methyl-4-heptyl.

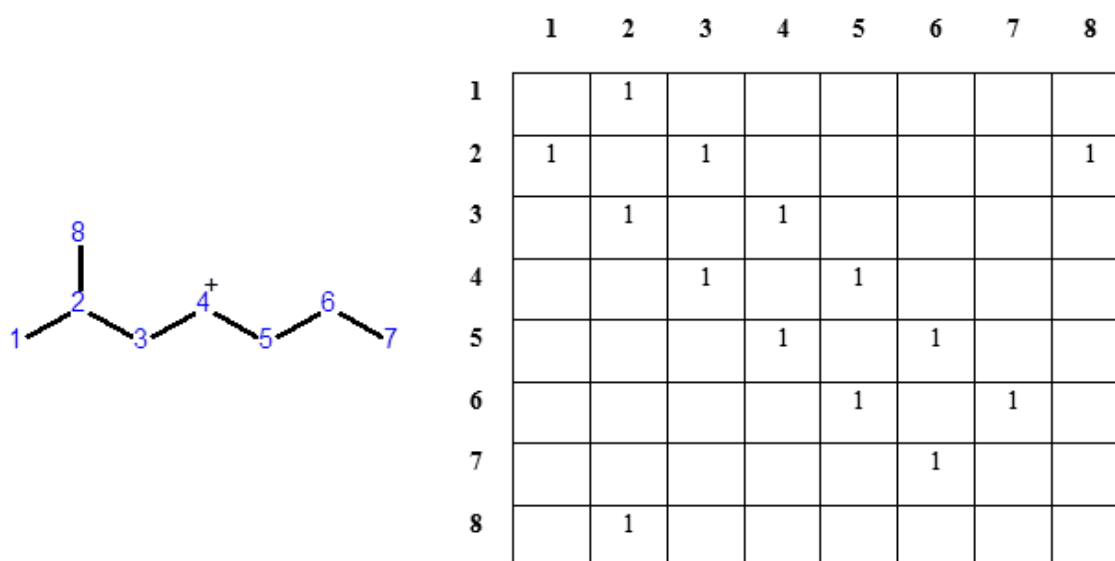


Figure 3-1: Boolean matrix representation for 2-methyl-4-heptyl

However, it is not possible distinguish different types of hydrocarbons using the Boolean matrix representation, which also requires large amount of memory for its storage when building the elementary steps involving long chain paraffinic compounds. To overcome these issues, the matrix can be converted to a simple characterization vector as showed in Figure 3-2 [5].

m	n	o	p	q	r	s
---	---	---	---	---	---	---

Figure 3-2: Characterization vector form

Where:

- m – position of the first methyl branch in the main chain;
- n – position of the second methyl branch in the main chain;
- o – position of third methyl branch in the main chain;
- p – total number of carbons in the molecule;
- q – position of the first carbon atom forming the double bond;
- r – position of the second carbon atom forming the double bond;
- s – position of positive charge;

Therefore, the characterization vector for the carbenium ion in consideration can be written as presented in Figure 3-3.

2	0	0	8	0	0	4
---	---	---	---	---	---	---

Figure 3-3: Characterization vector of 2-methyl-4-octyl

In this way, all possible elementary steps involved in the hydrodewaxing process can be easily identified and included to the reaction network. The chemical reactions are obtained by manipulating the Boolean matrices for the reactants and concatenating the resulting

characterization vectors [5]. To illustrate this procedure, consider the PCP isomerization of 3-methyl-4-heptyl whose Boolean matrix, characterization vector, and labeled molecular structure are presented in Figure 3-4.

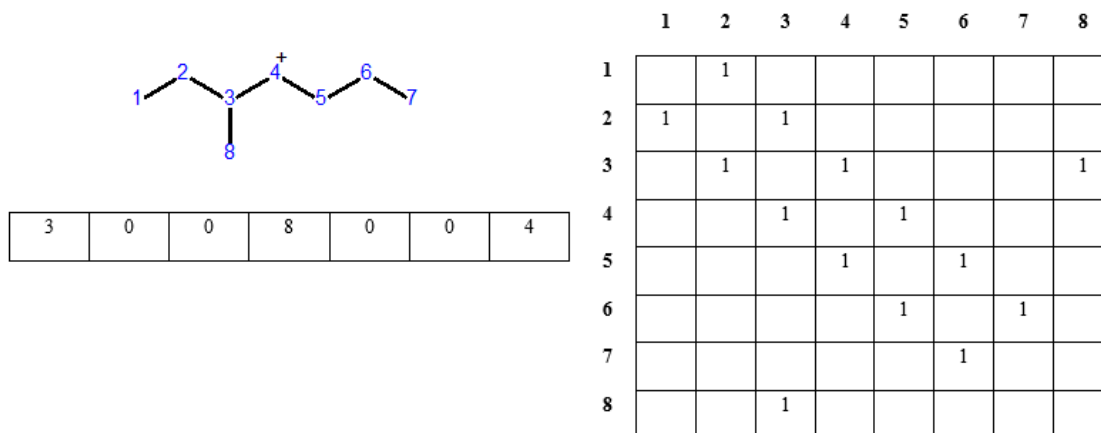


Figure 3-4: Molecular structure, characterization vector, and Boolean matrix for 3-methyl-4-heptyl

In order to computationally generate the PCP structures produced from this carbenium ion, all carbons in β position, which are defined as the second carbon atoms counting from the carbon bearing the charge, must be identified. It can be easily done using the matrix operation represented by Equation 3-1 [5].

$$\mathbf{M}^2 - \mathbf{I} \quad (3-1)$$

Where \mathbf{M} is the Boolean matrix for the reactant ion and \mathbf{I} is the identity matrix. By applying Equation 3-1, the β positions with respect to each carbon atom in the molecular structure are identified, which results in a Boolean matrix showed in Figure 3-5.

	1	2	3	4	5	6	7	8
1			1					
2				1				1
3	1				1			
4		1				1		1
5			1				1	
6				1				
7					1			
8		1		1				

Figure 3-5: Boolean matrix indicating the β -carbon positions in the molecular structure

By analyzing this matrix, it can be observed that the β -carbons with respect to the charged carbon atom at position 4 are located at positions 2, 6, and 8. Therefore, three PCP structures can be formed from this carbenium ion whose molecular representations are shown in Figure 3-6.

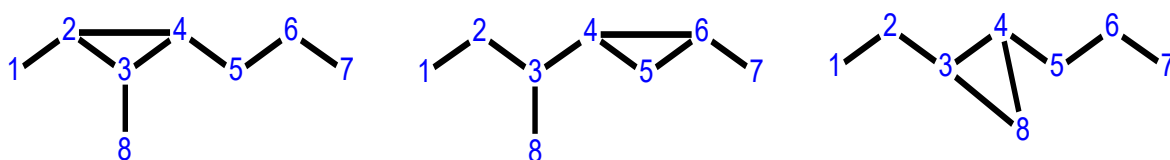


Figure 3-6: Possible PCP structures formed from 3-methyl-4-heptyl

Their Boolean matrices can be obtained by using the matrix operation expressed by Equation 3-2 [5].

$$m_{ij} = m_{ji} = 1 \quad (3-2)$$

Where m_{ij} is the entry in the reactant Boolean matrix representing the C-C bond between charged and β - carbons at positions “i” and “j”, respectively [5]. The second structure in Figure 3-6 is considered to further illustrate the procedure in this section whose Boolean matrix is given in Figure 3-7.

	1	2	3	4	5	6	7	8
1		1						
2	1		1					
3		1		1				1
4			1		1	1		
5				1		1		
6				1	1		1	
7						1		
8			1					

Figure 3-7: Boolean matrix for the PCP structure in consideration

This matrix was generated by placing the number “1” at the entries (4,6) and (6,4) in the reactant matrix. Once the PCP structure is formed, two reaction pathways can take place. In the α -cleavage, the bond linking the carbon bearing the charge and the one in α - position is broken. On the other hand, the β -cleavage takes place by eliminating the bond connecting both α - and β -carbons. These pathways are illustrated in Figure 3-8.

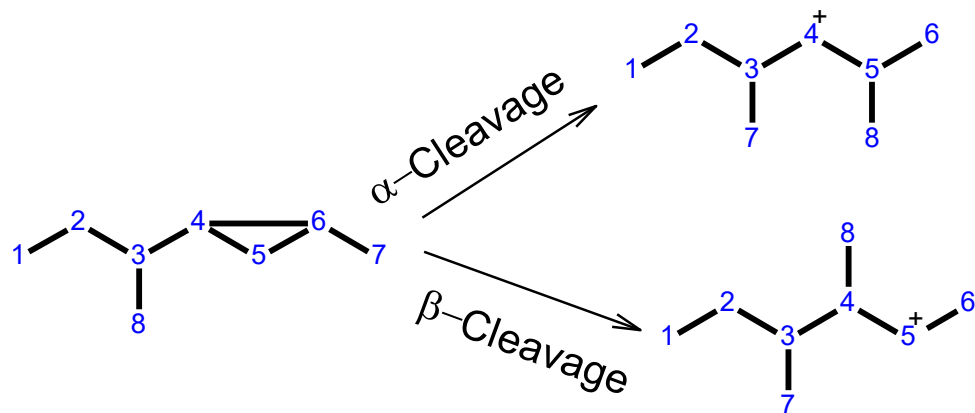


Figure 3-8: Isomerization pathways

Therefore, the product isomer is obtained by applying the following matrix operation to the Boolean matrix for the PCP structure in consideration [5].

$$m_{il} = m_{li} = 0 \quad (3-3)$$

Where the index “l” represents the position of either α - or β -carbons and “i” the position of charged carbon in the reactant ion. Hence, the Boolean matrix for the isomer produced through α -cleavage is represented by Figure 3-9.

	1	2	3	4	5	6	7	8
1		1						
2	1		1					
3		1		1				1
4			1			1		
5						1		
6				1	1		1	
7						1		
8			1					

Figure 3-9: Boolean matrix for the product isomer obtained through α -cleavage

It can be observed from this matrix that carbon “4” is connected to the ones at position “3” and “6”, which is inconsistent. It indicates that the resulted product ion is not enumerated in a standard fashion. Therefore, the Boolean matrix must be rearranged to the one shown in Figure 3-10.

	1	2	3	4	5	6	7	8
1		1						
2	1		1					
3		1		1			1	
4			1		1			
5				1		1		1
6					1			
7			1					
8					1			

Figure 3-10: Standardized Boolean Matrix for product ion resulted from the α -Cleavage pathway

Next, the Boolean matrix for the product ion is converted to characterization vector by identifying the location of its branches, double bonds, and charge, which is then concatenated to the one for the reactant ion. The resulting elementary step is stored as shown in Figure 3-11 [5].

3	0	0	8	0	0	4	3	5	0	8	0	0	4
---	---	---	---	---	---	---	---	---	---	---	---	---	---

Figure 3-11: Computer representation for the considered α -Cleavage elementary step

By applying the same procedure to other structures and pathways, all possible PCP isomerization steps for 3-methyl-4-heptyl can be obtained and stored in the reaction network. This procedure can be used to generate other types of elementary steps such as β -

scission, dehydrogenation and protonation. More information about the rules and matrix operations for the other types of elementary step are provided by Clymans and Froment (1984) and Baltanas and Froment (1985). The block diagram in Figure 3-12 summarizes the general procedure previously described.

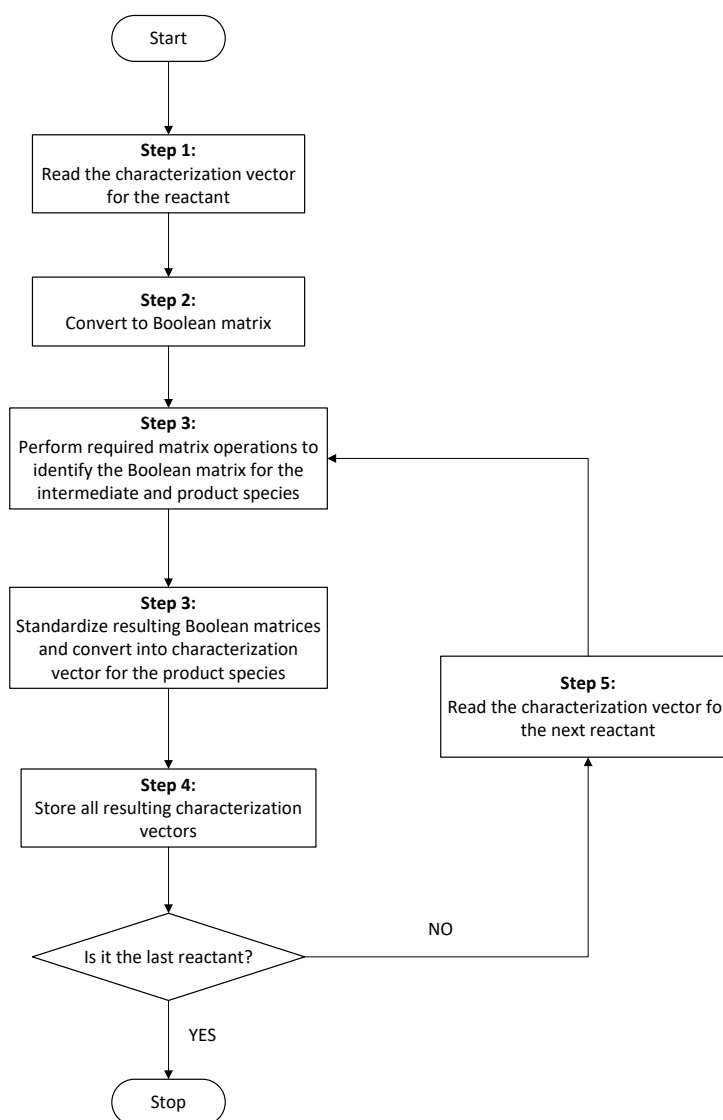


Figure 3-12: General algorithm to build the reaction network for an elementary step type

As n-hexadecane is selected as the model compound to estimate the single event kinetic parameters in this work, the number of elementary steps and species generated by the reaction network considering a pure feedstock for this compound are shown in Table 3-2 and Table 3-3, respectively.

Table 3-2: Number of elementary steps generated by the reaction network for n-hexadecane

Elementary step	Number of elementary steps
Dehydrogenation	4983
Deprotonation/Protonation	7358
Hydride-shift	4738
PCP-isomerization	8085
β -scission	1570
Hydrogenation	4983

Table 3-3: Number of species generated by the reaction network for n-hexadecane

Type	Number of Species
Paraffin	554
Carbenium ion	3680
Olefin	4983

To check if the reaction network algorithm used in this work was correctly implemented, the most general form of the algorithm was run using the carbenium ion chemistry rules for

hydrocracking of n-hexadecane on Pt/US-Y zeolites. The obtained number of elementary steps and species were compared to those obtained from Kumar and Froment (2007) as shown in Appendix A-2. The slight deviations among those values are related to the different standard fashion technique used to enumerate the carbon atoms in molecular structures applied in this work compared to the one used by those authors.

Based on the built reaction network, the single-event kinetic modelling can be applied to the catalytic dewaxing reactor model, which incorporates the mechanistic aspects of the chemical reactions involved in the process.

3.3.4. Single Event Kinetic Modelling

The single-event kinetic modeling was proposed by Froment and co-workers [7, 13, 14, 32] and has been extensively used to design, simulate, and optimize several industrial refining operations. Its formulation is based on the statistical thermodynamics and single event theory, which expresses the rate constant as given by Equation 3-4 [7].

$$k = \left(\frac{\sigma_{gl}^r}{\sigma_{gl}^\#} \right) \left(\frac{k_B T}{h} \right) \exp \left(\frac{\Delta \hat{S}^{0\#}}{R} \right) \exp \left(- \frac{\Delta H^{0\#}}{RT} \right) \quad (3-4)$$

The dependence of rate constant on the feedstock was factored out through the ratio of the global symmetry numbers represented by the first ratio in Equation 3-4, which is denominated as number of single events (n_e) and accounts for the changes in the reactant molecular structure due to chemical reaction. The other intrinsic terms are lumped into a

single-event rate constant (\tilde{k}), which is independent on the nature of the feedstock. Therefore, the rate constant can be rewritten as given by Equation 3-5 [7].

$$k = n_e \tilde{k} \quad (3-5)$$

This approach allows estimating a small set of kinetic parameters even if a large amount of elementary steps is taken into consideration. They are identified based on the type of elementary step and nature of the reactant and/or product carbenium ions involved in either PCP isomerization or β -scission reactions. Also, thermodynamic constraints are used to reduce even more the amount of parameters to be estimated [6].

Under "ideal" hydrocracking conditions, the rate-determining steps are located at the acid sites, and thereby, dehydrogenation/hydrogenation reactions taking place at the metal sites are assumed to be in pseudo-equilibrium [32]. In this way, the only kinetic parameters to be estimated are those related to the isomerization and cracking steps.

For PCP isomerization reactions, the difference in energy levels between reactant and product carbenium ions are only associated to the type of the carbon at which the positive charge is located at their structure i.e. only secondary due to the shape-selectivity effects [13]. On the other hand, the cracking steps are not only dependent on the nature of the ions but also on the type of olefin being produced, which can be classified as normal or branched [33]. As the hydride-shift reactions are assumed to be in pseudo-equilibrium, their rate constants are not included in the parameter estimation. Based on the previous information, Kumar (2004) concluded that 13 single-event rate and adsorption constants were necessary to model a conventional hydrocracking reactor. However, by adding the molecular shape and sizing constraints imposed by the shape-selectivity effects, less single-event rate

constants are required to describe the catalytic dewaxing, which are presented in Table 3-4.

Table 3-4: Single-event kinetic rate constants and Langmuir equilibrium coefficients for shape-selective Pt/ZSM-5

Rate-determining step	Single-event kinetic parameters
PCP-isomerization	$\tilde{k}_{PCP}(s, s)$
β -scission	$\tilde{k}_{cr}(s, s, no), \tilde{k}_{cr}(s, s, io)$
Langmuir equilibrium constants	$K_{L,np}, K_{L,mp}, K_{L,dp}, K_{L,tp}$

It can be observed that the Langmuir physisorption equilibrium constants are assumed to be only dependent on the nature of the paraffinic species [33].

3.3.5. Posteriori-Lumping

The amount of chemical species involved in the hydrocracking of petroleum fractions is extremely large and there is no analytical technique known so far that can measure their individual compositions. Therefore, the posteriori-lumping technique proposed by Vynckier and Froment (1991) is applied to group the paraffinic compounds with same degree of branching and carbon number into a single lump with internal composition distribution governed by the thermodynamic equilibrium. The equilibrium composition of

an individual paraffinic compound within lump L_m is calculated using Equation 3-6 proposed by Guillaume et al. (2011).

$$y_{i,L_m} = \frac{\exp\left(-\frac{\Delta G_{f,i}^{o,L}}{RT}\right)}{\sum_{i \in L_m} \exp\left(-\frac{\Delta G_{f,i}^{o,L}}{RT}\right)} \quad (3-6)$$

Therefore, it is possible to describe the reaction mixture involved in the dewaxing of n-hexadecane using 45 lumps, which includes one for hydrogen, making easier the validation with experimental data obtained from modern analytical techniques such as chromatography.

3.3.6. Rate Expressions and Kinetic Parameters

In this section, the rate expressions for consumption and formation of the paraffinic lumps involved in the hydrodewaxing process are presented based on the single event theory. The first step in the reaction mechanism is the physisorption of a particular paraffin into the zeolite cage whose sorbed and liquid phase concentrations are related based on the Langmuir isotherm given by Equation 3-7 [32].

$$[C_{P_i}] = \frac{C_{sat} K_{L,P_i} C_{P_i}^L}{1 + \sum_i K_{L,P_i} C_{P_i}^L} \quad (3-7)$$

Then, the sorbed paraffinic compound diffuses to a metal site where undergoes dehydrogenation, which is considered to be in pseudo-equilibrium as the catalyst has

enough metal sites to meet ideal hydrocracking conditions. Hence, the equilibrium concentration of the product olefin in liquid phase can be derived based on the dehydrogenation equilibrium coefficient as showed in Equation 3-8 [32].

$$C_{O_{ij}}^L = \frac{K_{DH}^{(P_i \leftrightarrow O_{ij})} C_{sat} K_{L,P_i} C_{P_i}^L}{C_{H_2}^L \left(1 + \sum_i K_{L,P_i} C_{P_i}^L \right)} \quad (3-8)$$

Next, the produced olefin migrates to an acid site where it is protonated into a carbenium ion, which reaction is also assumed to be in pseudo-equilibrium. Therefore, the ion concentration can be calculated based on the protonation/deprotonation equilibrium coefficient as given by Equation 3-9 [32].

$$C_{R_{ik}^+} = K_{pr/de}^{(O_{ij} \leftrightarrow R_{ik}^+)} C_{O_{ij}}^L C_{H^+} \quad (3-9)$$

As a particular carbenium ion can be generated from different olefins, it is convenient to express its concentration based on an average value as presented by Equation 3-10 [32].

$$C_{R_{ik}^+} = \frac{1}{n} \sum_{j=1}^n K_{pr/de}^{(O_{ij} \leftrightarrow R_{ik}^+)} C_{O_{ij}}^L C_{H^+} \quad (3-10)$$

Substituting Equation 3-8 into Equation 3-10, the average concentration of the carbenium ion can be written in terms of the one for the reactant paraffin in liquid phase by Equation 3-11 [32].

$$C_{R_{ik}^+} = \frac{1}{n} \sum_{j=1}^n \frac{K_{pr/de}^{(O_{ij} \leftrightarrow R_{ik}^+)} K_{DH}^{(P_i \leftrightarrow O_{ij})} C_{sat} C_{H^+} K_{L,P_i} C_{P_i}^L}{C_{H_2}^{liq} \left(1 + \sum_i K_{L,P_i} C_{P_i}^L \right)} \quad (3-11)$$

The equilibrium coefficients in Equation 3-11 are dependent on the molecular structures of the reactants and products. Hence, those effects can be factored out by writing those coefficients in their single-event form as presented by Equations 3-12 and 3-13 [6].

$$K_{pr/de}^{(O_j \leftrightarrow R_{ik}^+)} = \frac{\sigma_{O_j}^{gl}}{\sigma_{R_{ik}^+}^{gl}} \tilde{K}_{pr/de}^{(O_j \leftrightarrow R_{ik}^+)} \quad (3-12)$$

$$K_{DH}^{(P_i \leftrightarrow O_j)} = \frac{\sigma_{P_i}^{gl}}{\sigma_{O_j}^{gl} \sigma_{H_2}^{gl}} \tilde{K}_{DH}^{(P_i \leftrightarrow O_j)} \quad (3-13)$$

As proposed by Vynckier and Froment (1991), the protonation/deprotonation equilibrium coefficient can be rewritten considering an intermediate reference olefin, which is chosen such that the double bond is located between a secondary and a tertiary carbon atom, as given by Equation 3-14 [32]. This step is related to the concept that thermodynamic pathways are independent as long as the initial and final states are conserved.

$$\tilde{K}_{pr/de}^{(O_j \leftrightarrow R_{ik}^+)} = \tilde{K}_{pr/de}^{(O_r \leftrightarrow m_{ik})} \tilde{K}_{isom}^{(O_j \leftrightarrow O_r)} \quad (3-14)$$

Where m_{ik} is an intermediate carbenium ion obtained from the protonation/deprotonation reaction undergone by the reference olefin, which can be secondary or tertiary depending on the type of the product carbenium ion R_{ik}^+ [14]. Equation 3-14 is derived from the thermodynamic constraints involved in the protonation/deprotonation pathways and more details can be found in the work presented by Vynckier and Froment (1991).

By substituting Equations 3-13 through 3-14 into Equation 3-11, the average carbenium ion concentration can be expressed in terms of the global symmetry numbers, single-event equilibrium coefficients, and reactant paraffinic concentration in liquid phase by Equation 3-15 [32].

$$C_{R_{ik}^+} = \frac{1}{n} \left(\frac{\sigma_{P_i}^{gl}}{\sigma_{R_{ik}^+}^{gl} \sigma_{H_2}^{gl}} \right) \frac{\tilde{K}_{pr/de}^{(O_r \leftrightarrow m_{ik})} C_{sat} C_{H^+} K_{L,P_i} C_{P_i}^L}{C_{H_2}^L \left(1 + \sum_i K_{L,P_i} C_{P_i}^L \right)} \sum_{j=1}^n \tilde{K}_{isom}^{(O_j \leftrightarrow O_r)} \tilde{K}_{DH}^{(P_i \leftrightarrow O_j)} \quad (3-15)$$

As the rate-determining elementary steps are considered to follow first-order kinetics, the rate of consumption of a particular carbenium ion undergoing either PCP isomerization or cracking elementary steps can be expressed by using the single-event rate constants as showed by Equation 3-16 [32].

$$r_{R_{ik}^+} = n_e \tilde{k}(m, w) C_{R_{ik}^+} \quad (3-16)$$

Where the indices m and w represents the type of the reactant and product carbenium ions, which can be only secondary (s) based on the shape-selectivity constraints discussed in section 3.3.2. Therefore, by substituting Equation 3-15 into 3-16, this rate can be expressed in terms of the liquid concentration of the reactant paraffin as given in Equation 3-17 [32].

$$r_{R_{ik}^+} = n_e \tilde{k}(m, w) \frac{1}{n} \left(\frac{\sigma_{P_i}^{gl}}{\sigma_{R_{ik}^+}^{gl} \sigma_{H_2}^{gl}} \right) \frac{\tilde{K}_{pr/de}^{(O_r \leftrightarrow m_{ik})} C_{sat} C_{H^+} K_{L,P_i} C_{P_i}^L}{C_{H_2}^L \left(1 + \sum_i K_{L,P_i} C_{P_i}^{liq} \right)} \sum_{j=1}^n \tilde{K}_{isom}^{(O_j \leftrightarrow O_r)} \tilde{K}_{DH}^{(P_i \leftrightarrow O_j)} \quad (3-17)$$

For ideal hydrocracking of paraffinic species, the concentration of free active sites C_{H^+} can be assumed to be equal to the total concentration of active sites C_t once the concentration of adsorbed carbenium ions is small [32]. Also, the terms $\tilde{K}_{pr/de}^{(O_r \leftrightarrow m_{ik})}$, C_{sat} , and C_t are difficult to be analytically estimated, and thereby, they can be lumped with the single-event rate constant, which leads to the definition of the composite single-event rate constant expressed by Equation 3-18 [32].

$$\tilde{k}^*(m, w) = \tilde{k}(m, w) \tilde{K}_{pr/de}^{(O_r \leftrightarrow m_{ik})} C_{sat} C_t \quad (3-18)$$

Therefore, the final form for the rate of consumption for a particular carbenium ion can be expressed by Equation 3-19 by substituting Equation 3-18 into Equation 3-17 [32].

$$r_{R_{ik}^+} = n_e \tilde{k}^*(m, w) \frac{1}{n} \left(\frac{\sigma_{P_i}^{gl}}{\sigma_{R_{ik}^+}^{gl} \sigma_{H_2}^{gl}} \right) \frac{K_{L,P_i} C_{P_i}^L}{C_{H_2}^{liq} \left(1 + \sum_i K_{L,P_i} C_{P_i}^L \right)} \sum_{j=1}^n \tilde{K}_{isom}^{(O_j \leftrightarrow O_r)} \tilde{K}_{DH}^{(P_i \leftrightarrow O_j)} \quad (3-19)$$

It was showed in section 3.3.3 that thousands of paraffins, olefins, and carbenium ions are involved in the hydroconversion process, which leads to a prohibitive amount of kinetic parameters to be estimated. Instead, a global rate expression based on the conversion of a lump generated by the posteriori-lumping technique into another is used to build a reactor model.

The rate of consumption of a paraffinic lump L_m undergoing the elementary step type l involving the reactant and product carbenium ions of type m and w (secondary), respectively, can be obtained using the Equation 3-20 [32].

$$R_{L_m, l, m, w}^{Cons} = LCC_{L_m, l, m, w} \frac{\tilde{k}_l^*(m, w) K_{L, L_m} C_{L_m}^L}{C_{H_2}^L \left[1 + \sum_i K_{L, L_m} C_{L_m}^L \right]} \quad (3-20)$$

The Lumping Coefficient of Consumption (LCC) is only dependent on the information obtained from the reaction network and can be calculated by Equation 3-21 [32].

$$LCC_{L_m, l, m, w} = \sum_{q=1}^{q_r} n_{e,q} y_{i, L_m} \frac{1}{n} \left(\frac{\sigma_{P_i}^{gl}}{\sigma_{O_j}^{gl} \sigma_{H_2}^{gl}} \right) \sum_{j=1}^n \tilde{K}_{isom}^{(O_j \leftrightarrow O_r)} \tilde{K}_{DH}^{(P_i \leftrightarrow O_j)} \quad (3-21)$$

It is important to note that the rate of consumption for a given lump represents the rate at which all the carbenium ions of type m within the lump L_m are being converted into ions of type w within other lumps through elementary step l [32]. Similarly, the rate of formation for a given lump L_m produced from k different lumps L_k and the Lumping Coefficient of Formation (LCF) are expressed by Equation 3-22 and Equation 3-23, respectively [32].

$$R_{L_m, L_k, l, m, w}^{Form} = \sum_k LCF_{L_m, L_k, l, m, w} \frac{\tilde{k}_l^*(m, w) K_{L, Lk} C_{Lk}^{liq}}{C_{H_2}^{liq} \left[1 + \sum_i K_{L, Lk} C_{Lk}^{liq} \right]} \quad (3-22)$$

$$LCF_{L_m, L_k, l, m, w} = \sum_{q=1}^{q_T} n_{e, q} y_{i, Lk} \frac{1}{n} \left(\frac{\sigma_{P_i}^{gl}}{\sigma_{R_k}^{gl} \sigma_{H_2}^{gl}} \right) \sum_{j=1}^n \tilde{K}_{isom}^{(O_j \leftrightarrow O_r)} \tilde{K}_{DH}^{(P_i \leftrightarrow O_j)} \quad (3-23)$$

The net rate of formation for the lump L_m is obtained by summing the difference between rates of formation and consumption over all the elementary steps as showed by Equation 3-24 [32].

$$R_{L_m, net}^{Form} = \sum_{l=1}^{n_l} (R_{L_m}^{Form} - R_{L_m}^{Cons}) \quad (3-24)$$

To simplify the parameter estimation based on the type of experimental data available, the composite single-event rate and adsorption constants are rewritten based on the Arrhenius and Van't Hoff laws, respectively. It can be done by expressing the single-event rate constant $\tilde{k}_l(m, w)$ and the protonation/deprotonation equilibrium coefficients $\tilde{K}_{pr/de}^{(O_r \leftrightarrow m_{ik})}$ as a function of temperature, respectively, as showed by Equations 3-25 and 3-26 [32].

$$\tilde{k}_l(m, w) = \tilde{A}_l \exp\left(-\frac{E_l}{RT}\right) \quad (3-25)$$

$$\tilde{K}_{pr/de}^{(O_r \leftrightarrow m_{ik})} = \tilde{A}_{pr/de} \exp\left(-\frac{\Delta H_{pr/de}}{RT}\right) \quad (3-26)$$

Substituting Equations 3-25 and 3-26 into Equation 3-18, the Arrhenius equation for the composite single-event rate constant can be expressed by Equation 3-27 [32].

$$\tilde{k}_l^*(m, w) = \tilde{A}_l \tilde{A}_{pr/de} C_{sat} C_t \exp\left(-\frac{(E_l + \Delta H_{pr/de})}{RT}\right) \quad (3-27)$$

Hence, the composite single-event frequency factors and activation energy that must be estimated are represented by Equations 3-28 and 3-29, respectively.

$$\tilde{A}_l^* = \tilde{A}_l \tilde{A}_{pr/de} C_{sat} C_t \quad (3-28)$$

$$E_l^* = E_l + \Delta H_{pr/de} \quad (3-29)$$

Finally, the Langmuir equilibrium coefficients can be expressed in terms of Van't Hoff law represented in generic form by Equation 3-30.

$$K_{L,j} = K_{0,j} \exp\left(-\frac{\Delta H_{L,j}}{R} \frac{1}{T}\right) \quad (3-30)$$

Based on the rate constants showed in the Table 3-5, a total of 14 Arrhenius and Van't Hoff adsorption parameters must be estimated from experimental data, which are summarized in Table 3-5.

Table 3-5: Composite single-event Arrhenius and Langmuir adsorption parameters to be estimated

Rate-determining step	Kinetic Parameters
PCP-isomerization	$\tilde{A}_{PCP(s,s)}^*, \frac{E_{PCP(s,s)}^*}{R}$
β -scission	$\tilde{A}_{cr(s,s,no)}^*, \tilde{A}_{cr(s,s,io)}^*, \frac{E_{cr(s,s,no)}^*}{R}, \frac{E_{cr(s,s,io)}^*}{R}$
Langmuir equilibrium constants	$K_{0,np}, K_{0,mp}, K_{0,dp}, K_{0,tp},$ $\frac{\Delta H_{L,np}}{R}, \frac{\Delta H_{L,mp}}{R}, \frac{\Delta H_{L,dp}}{R}, \frac{\Delta H_{L,tp}}{R}$

A block diagram summarizing the calculation routine to obtain the lumping coefficients to compute the reaction rates during the kinetic parameter estimation is shown Figure 3-13.

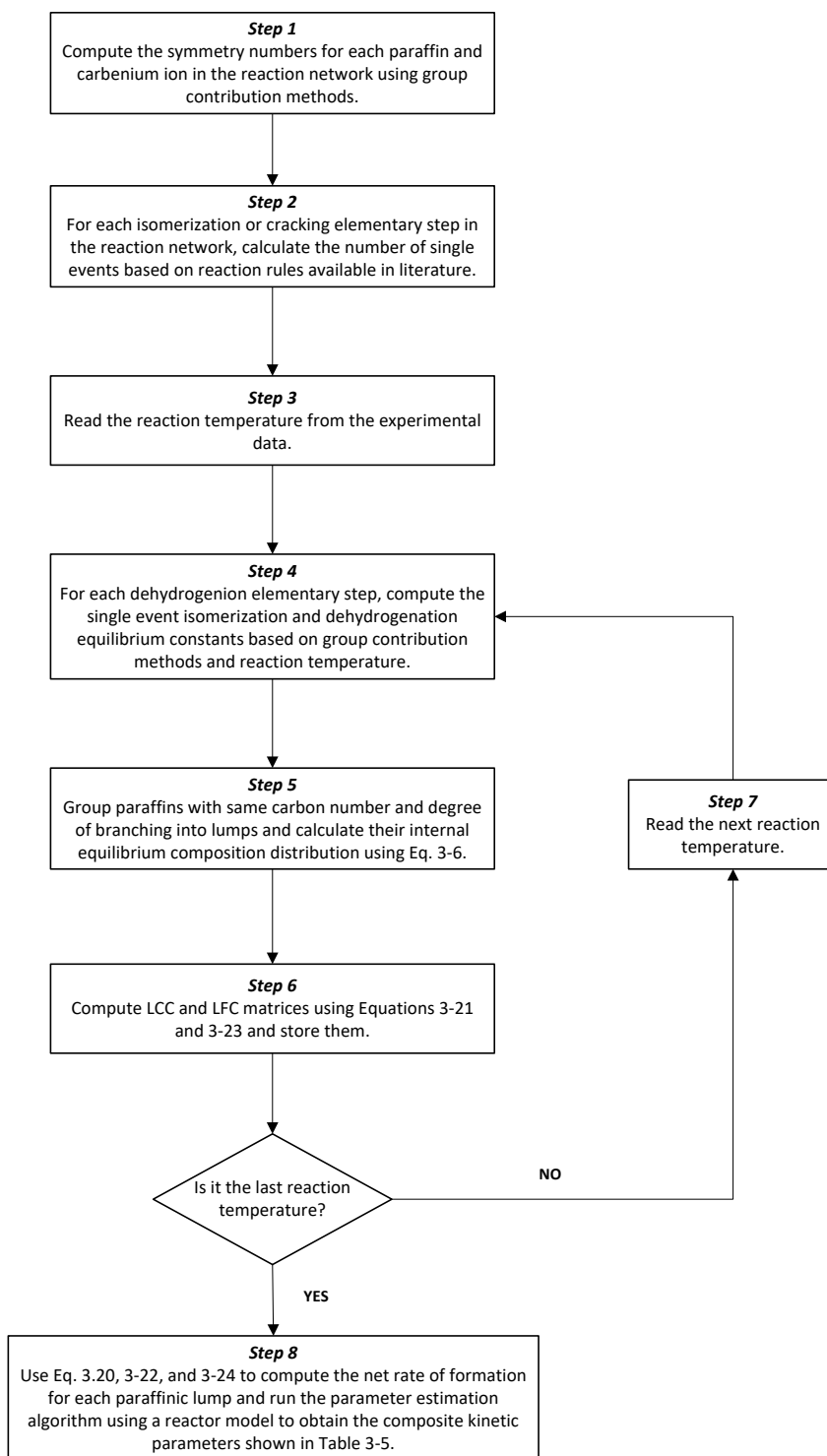


Figure 3-13: Calculation routine to obtain the lumping coefficients of consumption and formation

3.3.7. Reactor Model

In this section, the material balance equations representing the isothermal reactor model is presented. For a trickle bed reactor, the continuity equation for a given lump in both liquid and gas phases must account for the interphase mass transfer and the reaction kinetics. In order to simplify the model formulation, some assumptions must be imposed:

- Isothermal operation;
- The gas and liquid phases flow downwards in plug flow pattern;
- The gas phase is considered to be continuous while liquid is the dispersed phase;
- Trickle flow pattern is assumed for liquid phase;
- Due to the evaporation of light components and dissolution of hydrogen into the liquid phase, gas-liquid interphase mass transfer of the species is modeled based on the two-film theory;
- As the hydrogenation/dehydrogenation elementary steps are considered in pseudo-equilibrium, the hydrogen concentration in liquid phase is limited by its equilibrium value;
- Negligible pressure drop across the bed
- No diffusional limitations in the catalyst particle;

The interphase mass transfer flux was formulated based on the two-film theory, which is represented by Equation 3-31 [7].

$$N_i = k_{o,i} a_v \left(\frac{C_i^G}{K_i^{C,VLE}} - C_i^L \right) \quad (3-31)$$

The volumetric overall mass transfer coefficient can be calculated using the individual mass transfer film coefficients as given by Equation 3-32 [7].

$$\frac{1}{k_{o,i}a_v} = \frac{1}{K_i^{C,VLE}k_Ga_v} + \frac{1}{k_La_v} \quad (3-32)$$

The partitioning coefficients in Equation 3-30 and Equation 3-31 can be expressed in terms of the true equilibrium coefficient calculated from Peng-Robinson equation of state as shown in Equation 3-33 [35].

$$K_i^{C,VLE} = K_i^{VLE} \frac{\rho_{molar}^G}{\rho_{molar}^L} \quad (3-33)$$

The continuity equations for gas and liquid phases for a given lump can be expressed by Equations 3-34 and 3-35, respectively [7].

$$\frac{1}{A} \frac{dF_i^G}{dz} = -k_{o,i}a_v \left(\frac{C_i^G}{K_i^{C,VLE}} - C_i^L \right) \quad \text{at } z = 0, F_i^G = F_{i,0}^G \quad (3-34)$$

$$\frac{1}{A} \frac{dF_i^L}{dz} = k_{o,i}a_v \left(\frac{C_i^G}{K_i^{C,VLE}} - C_i^L \right) + R_{i,net}^{form} \quad \text{at } z = 0, F_i^L = F_{i,0}^L \quad (3-35)$$

The boundary conditions necessary to solve Equations 3-34 and 3-35 were obtained from VLE flash calculations as it was assumed that the initial mixture containing hydrogen and n-hexadecane flashes before reaching the catalytic bed. Also, as part of the liquid vaporizes along the reactor due to the high operating temperature, vapor-liquid equilibrium (VLE) calculations must be simultaneously performed while solving the set of differential equations. The calculation routine used to solve the continuity equations represented by Equations 3-34 and 3-35 is presented in Figure 3-14.

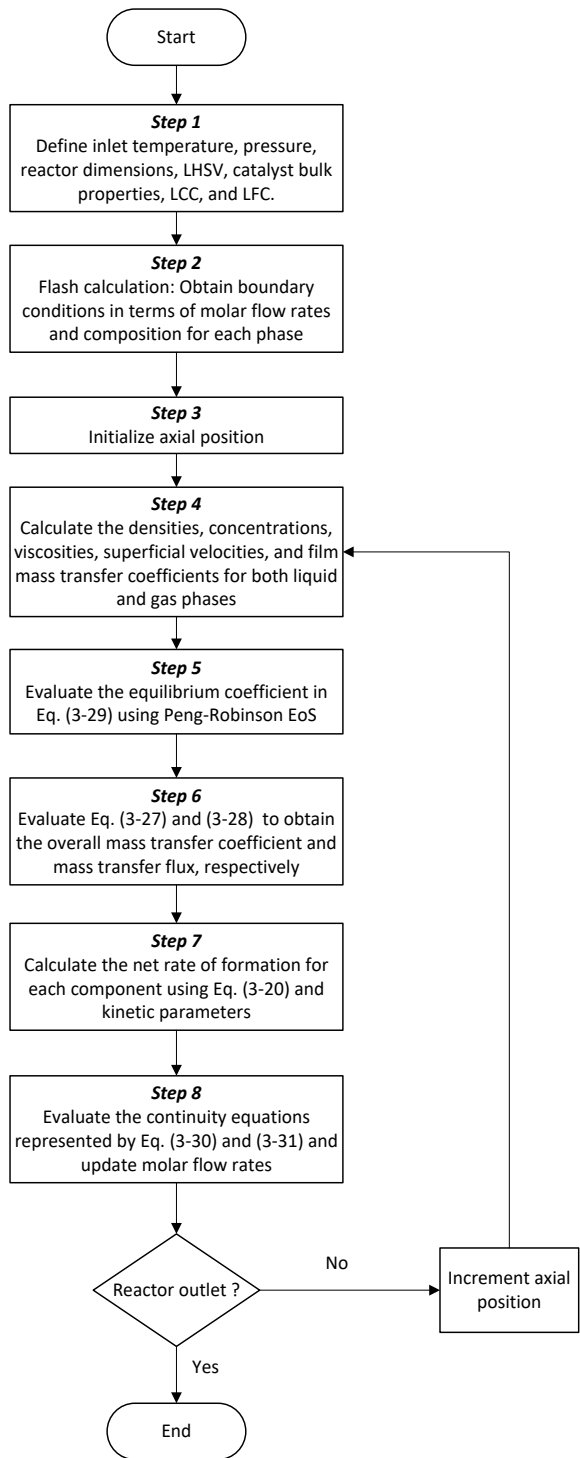


Figure 3-14: Schematic representation of the calculation routine adopted to solve the reactor model

3.3.8. Physical Properties Estimation

The physical and thermodynamic properties for the lumps/paraffinic molecules were evaluated using different sources as indicated below:

- The gas and liquid densities were evaluated using the Peng-Robinson equation of state and suitable mixing rules.
- The critical properties for a particular paraffinic molecule were calculated using the group contribution method proposed by Skander and Chitour (2002). Then, the mixing rules found in the American Petroleum Institute (1997) were applied to estimate the critical properties for the paraffinic lumps.
- The standard heat of formation and entropy for the pure paraffins were evaluated using the group contribution method developed by Domalski and Hearing (1988). To calculate these properties for the paraffinic lumps, the weighted average based on the paraffinic mole distribution within the lump was used. The equilibrium constants were evaluated by applying the Van't Hoff equation.
- The viscosity for gas and liquid phases were evaluated using the correlation presented by Poling et al. (2001) and Twu (1985), respectively.
- The correlations proposed by Reiss (1967) and Sato et al. (1972) were used to evaluate the volumetric mass transfer film coefficients for the gas and liquid sides, respectively.
- The symmetry numbers for the paraffinic species were calculated using the group contribution method proposed by Song (2004).

- The number of single events was estimated using the rules proposed by Martinis and Froment (2006) for the different types of elementary steps.

3.4. Results and Discussions

3.4.1. Parameter Estimation

In order to estimate the composite single event rate and Langmuir equilibrium constants, the sum of squares error between calculated and experimental values of total conversion and isomerization yields, respectively, was used as objective function for the minimization problem given by Equation 3-36.

$$\min_{\theta} SSE(\theta) = \sum_{i=1}^{N_{RES}} \sum_{j=1}^{N_{OBS}} (y_{ij} - \hat{y}_{ij})^2 \quad (3-36)$$

The definition of total conversion and isomerization yield used in the parameter estimation are given by Equations 3-37 and 3-38.

$$X_{tot} = \frac{(F_{n-C_{16},0}^G + F_{n-C_{16},0}^L) - (F_{n-C_{16},out}^G + F_{n-C_{16},out}^L)}{(F_{n-C_{16},0}^G + F_{n-C_{16},0}^L)} \quad (3-37)$$

$$Y_{iso} = \frac{\sum_{i=1}^{N_{iso}} (F_i^G + F_i^L)}{(F_{n-C_{16},0}^G + F_{n-C_{16},0}^L)} \quad (3-38)$$

Where N_{iso} represents the total number of monobranched, dibranched, and tribranched isomers of hexadecane. As the composite single event kinetic parameters do not depend on the feedstock type, the experimental values for total conversion of n-hexadecane and

isomerization yield were used to perform the parameter estimation. Those values were taken from Dougherty et al. (2001), who conducted catalytic activity studies feeding this component in a tubular reactor loaded with Pt/ZSM-5 catalyst. In total, 12 data points for six different temperatures were available. The authors carried out the shape-selective hydrocracking reactions in a ½” tubular reactor loaded with 5.7 g of catalyst and Liquid Hourly Space Velocity (LHSV) set to 0.4 h⁻¹. As the Hydrogen-to-Hydrocarbon (H₂/HC) ratio was not provided, it was predicted through the parameter estimation in order to maintain the accuracy of the model, which was found to be 2.016, which is reasonable for a pilot reactor operation. Single regression imputation was used to obtain four additional data points. Regression curves were fit to the available data set and the total conversion and isomerization yield for two unavailable temperatures (285°C and 312°C) were estimated using the obtained regressed expressions.

The objective function represented by Equation 3-36 is proven to be highly nonlinear and consistent lower and upper bounds were imposed to the parameters based on thermodynamic constraints so that realistic values could be obtained. The initial guess for optimization was chosen based on the kinetic parameters obtained by Kumar (2004) for Pt/US-Y zeolites and the constrained interior-point algorithm available in the MATLAB[®] optimization toolbox was used to minimize Equation 3-36. In order to test the sensitivity of the kinetic parameters, small random numbers were added to each total conversion and isomerization yield data point and the parameters were re-estimated five times so that their standard deviation could be calculated. This optimization framework adopted in this work is summarized in Figure 3-15 and the estimated parameters as well as their respective standard deviation are presented in Table 3-6.

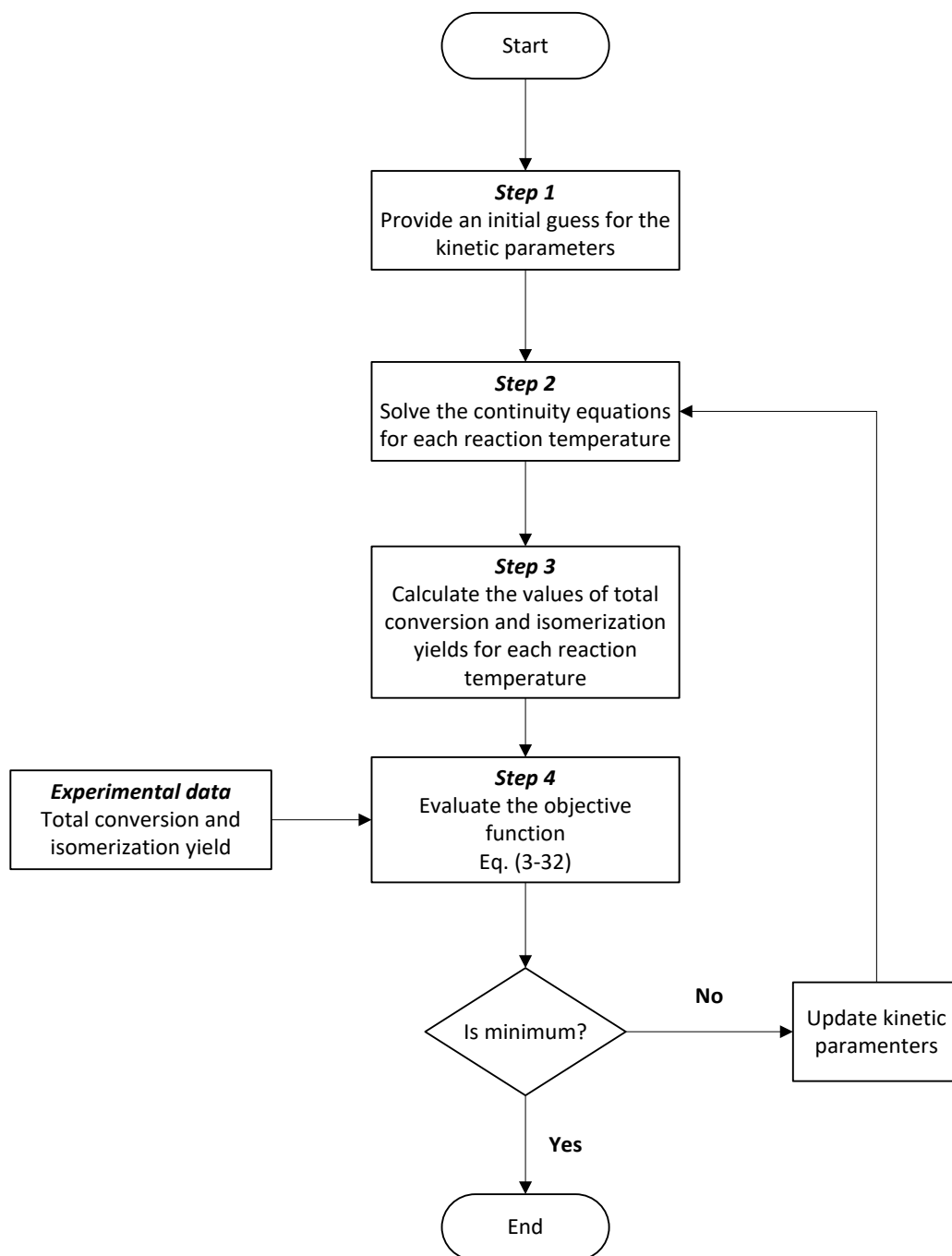


Figure 3-15: Optimization framework for kinetic parameter estimation

Table 3-6: Estimated single-event rate and Langmuir equilibrium constants for Pt/ZSM-5

Parameter	Estimated Value	Standard Deviation
$\tilde{A}_{PCP(s,s)}^*$	1.44x10 ⁸	0
$\frac{E_{PCP(s,s)}^*}{R}$	9782.7	0
$\tilde{A}_{cr(s,s,no)}^*$	54485.91	8.73x10 ⁻⁴
$\frac{E_{cr(s,s,no)}^*}{R}$	1754.4	0.105
$\tilde{A}_{cr(s,s,io)}^*$	1989.6	0.0171
$\frac{E_{cr(s,s,io)}^*}{R}$	8784.3	3.49x10 ⁻³
$K_{0,np}$	5.27x10 ⁻⁵	0
$\frac{\Delta H_{L,np}}{R}$	-4613.5	0
$K_{0,mp}$	6.87x10 ⁻⁷	0
$\frac{\Delta H_{L,mp}}{R}$	-6504.0	8.73x10 ⁻⁴
$K_{0,dp}$	4.93x10 ⁻⁰⁷	0
$\frac{\Delta H_{L,dp}}{R}$	-0.3562	6.98x10 ⁻³

$K_{0,tp}$	4.4693×10^{-07}	1.39×10^{-2}
$\frac{\Delta H_{L,tp}}{R}$	-296.3213	0

The comparison between experimental and calculated values for total conversion and isomerization yield can be seen in Figures 3-16 and 3-17, respectively.

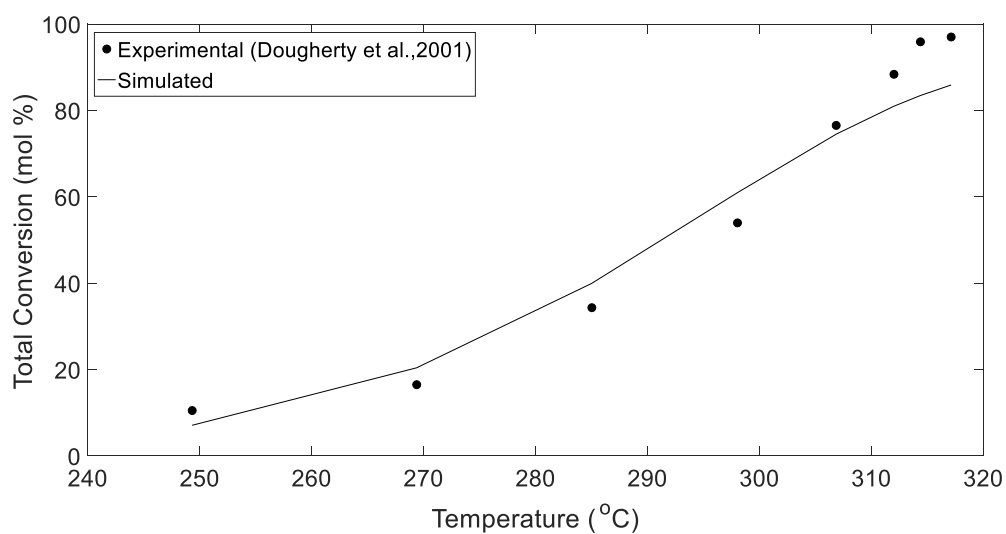


Figure 3-16: Total conversion profile for n-hexadecane feed

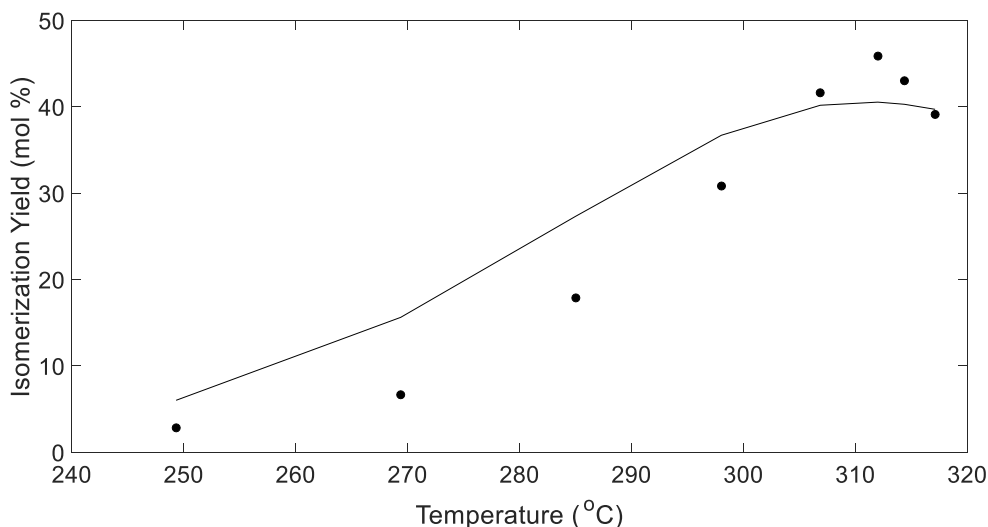


Figure 3-17: Isomerization yield profile for n-hexadecane feed

It can be observed from Figure 3-16 that the total conversion profile is in good agreement with the literature data for conversion up to 306°C and underpredicts for higher temperatures. The model for isomerization yield in Figure 3-17 overpredicts at low temperatures and underpredicts at high temperatures. Finally, it can be noted from Table 3-6 that most of the parameters have not changed except those related to cracking steps when small random numbers were added to the data points and they were re-estimated. Several reasons can be attributed to explain those deviations. The first one is related to the fact that the assumptions made regarding to the shape-selectivity effects may be too conservative for Pt/ZSM-5, which is classified as a 5-ring zeolite catalyst. It should be recalled that those assumptions were adopted based on studies done on shape-selective catalysis involving Pt/ZSM-22 catalysts, which have smaller pores for being 10-ring zeolites. Therefore, some of the suppressed elementary steps involving tertiary carbenium ions either for PCP isomerization or β -scission might be important for the hydroconversion

on Pt/ZSM-5. It was also realized through VLE calculations that most of the feedstock was flashed at high temperatures and the estimation of some physical properties such as viscosity became slightly inaccurate at such condition. As data set used for parameter estimation was small and the H_2/HC was also estimated, extra data points needed to be obtained by using simple regression imputation, which can be affecting the accuracy of the model. However, the profiles for total conversion and isomerization yield presented in this work agree with those commonly reported in literature for conventional and shape-selective hydrocracking processes.

Another possible explanation for the deviations observed in Figures 3-16 and 3-17 can be related to the mass transport limitations within the catalyst particle. As shown by Vandeghutche et al. (2014a), the pore structure of the Pt/ZSM-5 induces mass transport limitations as the main shape selectivity mechanism leading to higher selectivity towards 2-methyl-branched than 3-methyl-branched alkanes causing deviations from the thermodynamic equilibrium within the monobranched paraffinic lump. Therefore, the application of the posteriori-lumping approach to formulate the global rate of consumption and formation for monobranched lump may not be valid contributing to the errors observed in Figures 3-16 and 3-17. Also, if mass transport limitations were rate-determining step, lower values of the isomerization yield would be observed as the reaction rates would decrease, and thereby, improvements in the results could be expected. However, it has not been reported yet in the literature how to modify the posteriori-lumping approach to effectively decrease the number of continuity equations to be solved when dealing with large reaction networks while identifying the molecules within the lump that would diffuse slower within the catalyst pellet, which is going to be the scope for a future research.

3.4.2. Effect of Temperature

At low temperatures, the total conversion is low and the PCP-isomerization reactions does not take place at enough extension to allow cracking reactions to emerge as they are secondary reactions. On the other hand, at high temperatures, the n-hexadecane is quickly converted to monobranched paraffins, which are then converted to multibranched isomers through secondary PCP-isomerization steps. Consequently, the cracking reactions rates are high enough to make the isomerization yield to decrease as temperature is further raised. Therefore, the isomerization yield should present a maximum value as observed in Figure 3-17. A better view of this phenomena can be seen by analyzing the molar flow rate profiles across the reactor as shown in Figure 3-18 for temperatures at 298.03°C and 317.12°C, respectively. These profiles were obtained by summing the gas phase mole flows for each class to those for liquid phase.

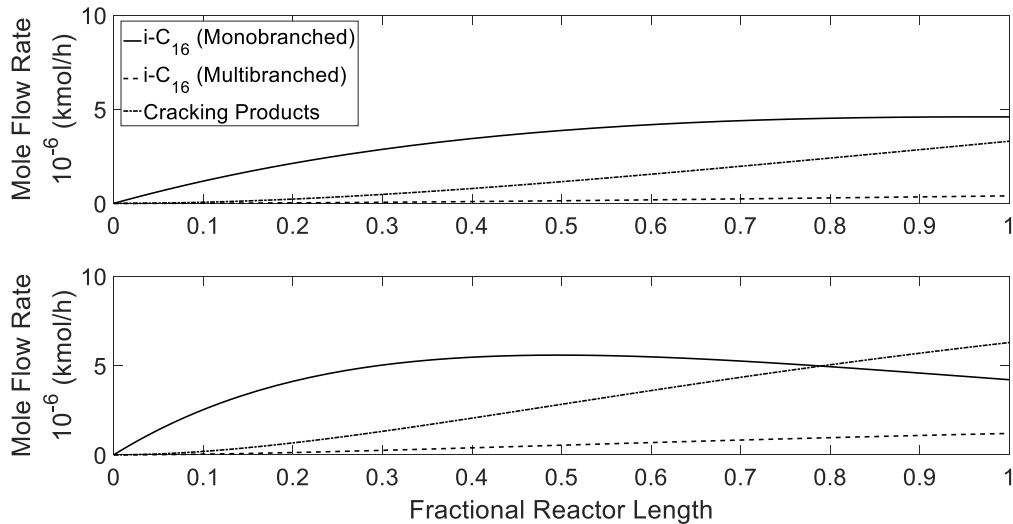


Figure 3-18: Combined molar flow rate profiles for reactor temperatures at 298.03°C (top) and 317.12°C (bottom)

It can be observed that at low temperature the cracking products start forming at 20% of catalytic bed when enough monobranched C₁₆ has been formed to allow β-scission reactions to take place. This is due to the fact that the cracking reactions can only form stable carbenium ions when the carbon located at the β position with respect to charged carbon atom is tertiary. As the formation of tertiary carbenium ions are suppressed in shape-selective catalyst, only few (s,s) PCP-isomerization steps are found in the reaction network forming dibranched and tribranched C₁₆ isomers, which are more likely to crack and explains their small values of molar flow rate along the reactor. When the temperature is raised, the reaction rates are increased so that C₁₆ isomers are quickly formed. However, the cracking reaction rates are also intensified so that their products become significant after 30% of the reactor length and they become faster than the PCP-isomerization rates at around 80% of the reactor length, which characterizes a maximum value of molar flow rate for monobranched C₁₆ isomers. Also, the quicker formation of multibranched C₁₆ isomers contributes to the higher cracking reaction rates once they have higher probability to crack. The zero slope of the molar flow rate curves for cracking and multibranched C₁₆ products indicates that they are secondary reaction products, which is related to the ideal hydrocracking assumption.

3.4.3. Effect of Pressure

The effect of pressure on the total conversion, isomerization and cracking yields is presented in Figure 3-19.

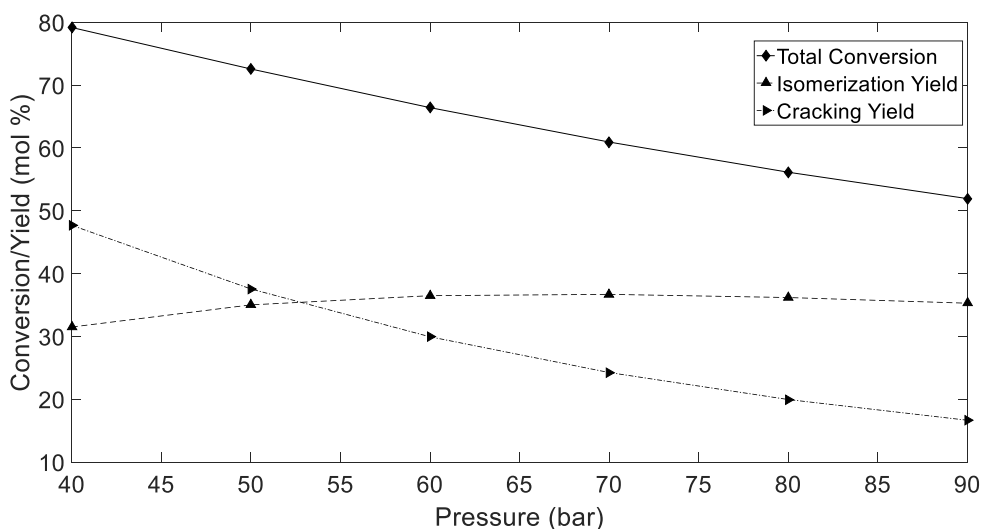


Figure 3-19: Effect of pressure on total conversion, isomerization, and cracking yields for n-hexadecane feed at LHSV = 0.4 h⁻¹, T = 298.03°C, and H₂/HC = 2.016

In trickle bed reactor operation, increasing the reactor pressure increases the solubility of hydrogen in liquid phase due to its higher fugacity value. Therefore, as the reaction order with respect to hydrogen is negative, the reaction rates and the total conversion of n-hexadecane decreases as pressure is increased, which explains the trends in Figure 3-19. At low pressures, the conversion is high enough to maintain the cracking yield higher than that for isomerization once enough branched paraffinic compounds are formed to promote the cracking steps. As the pressure is increased, the isomerization yield slightly increases until reaching a maximum once the cracking rates consuming the monobranched and multibranched C₁₆ isomers slow down allowing them to form at higher extension. This trend continues until the cracking yield become significantly low and the isomerization steps dominates the total conversion behavior, which starts dropping due to the slower isomerization rates caused by the higher hydrogen solubility.

Therefore, the reactor simulations performed in this section indicates that reactor pressure must be carefully selected during industrial catalytic dewaxing operations so that isomerization yields are maximized and yield losses are avoided while keeping an acceptable level of total conversion.

3.4.4. Effect of H₂/HC Ratio

The effect of the H₂/HC on the total conversion, isomerization, and cracking yields was studied through reactor simulations, which results are shown in Figure 3-20.

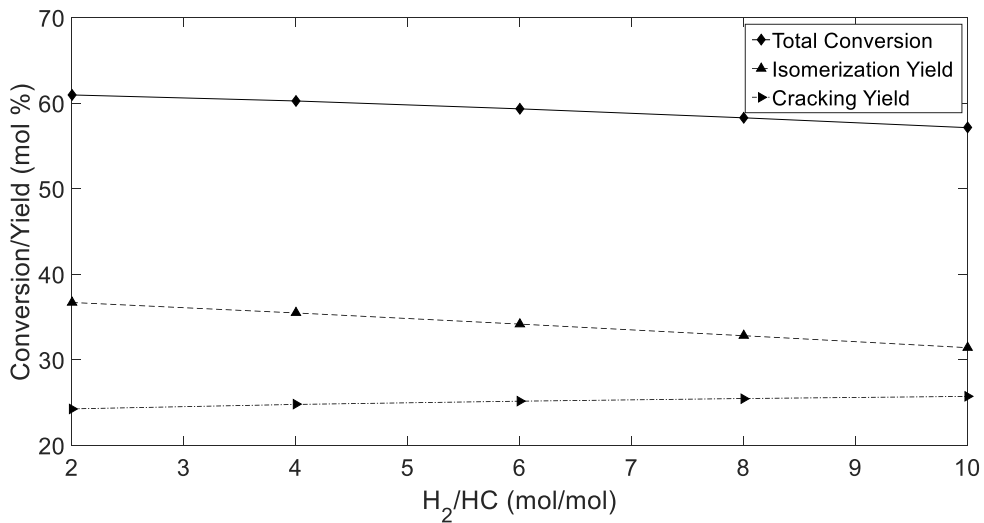


Figure 3-20: Effect of the H₂/HC ratio on total conversion, isomerization, and cracking yields for n-hexadecane feed at LHSV = 0.4 h⁻¹, T = 298.03°C, and P = 69.96 bar

It can be observed that the total conversion and yield values are not strongly affected by the changes in H₂/HC ratio, which is in agreement with the expected behavior for three-phase hydrocracking processes reported by Kumar and Froment (2007). In Figure 3-20, the

total conversion and isomerization yield slightly decreases while the cracking yield increases when the H_2/HC ratio is raised. The main explanation for such behavior lies on the fact that increasing this ratio enhances the overall mass transfer coefficient for interphase mass transfer, which intensifies the evaporation of light paraffinic compounds and increases the rate of secondary cracking explaining the increase in the cracking yield [7]. Also, the high value of H_2/HC ratio indicates that more hydrogen is fed to the system compared to n-hexadecane and the concentration of hydrogen in liquid phase is expected to be higher under such conditions, which justifies the decrease in total conversion. The combination of these two factors also explains the drop in the isomerization yield as the cracking steps are going to consume the C_{16} isomers faster as well as the higher concentration of hydrogen in liquid phase slow down the isomerization rates.

Therefore, the H_2/HC ratio does not strongly affect the reactor performance as long as the trickle flow conditions are found during the catalytic dewaxing operation. If the operation is carried out in gas phase, hydrogen becomes a reactant fed in excess and this parameter is going to significantly affect the reactions rates [32]. It can be mainly used to control the yield losses as it governs the rate of secondary cracking due the evaporation of light paraffinic compounds.

3.4.5. Effect of Liquid Hourly Space Velocity (LHSV)

The LHSV is a parameter associated with the residence time that reacting mixture spends within the catalytic bed. To study its effect on the reactor performance, several reactor

simulations were carried varying its value and keeping the other operating conditions such as pressure, H_2/HC ratio, and temperature constant. The results are shown in Figure 3-21.

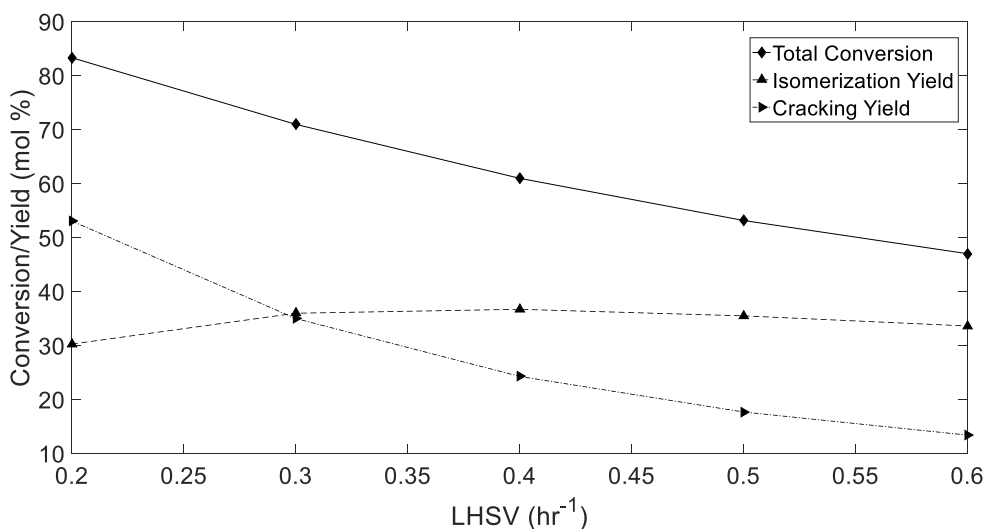


Figure 3-21: Effect of the LHSV on total conversion, isomerization, and cracking yields for n-hexadecane feed at $H_2/HC = 2.016$, $T = 298.03^\circ\text{C}$, and $P = 69.96$ bar

As the residence time is represented by the inverse of the LHSV value, it is expected that the total conversion decreases as the LHSV increases as shown in Figure 3-21. Lower values of LHSV indicates that the reactants are going to spend more time reacting inside the catalytic bed, and thereby, more branched isomers are formed to intensify the cracking reaction rates. It explains the higher value of cracking yield compared to the isomerization one at low LHSV. As the LHSV increases, the isomerization yield initially increases until a maximum value as the cracking reaction rates slow down but still dominating the conversion process. Therefore, less monobranched and multibranched C_{16} isomers are cracked down. Once the cracking yield is significantly lowered, the isomerization rates also

slow down due to the low residence time and starts decreasing following the trend for total conversion, which is mainly governed by the PCP-isomerization steps at such conditions. Therefore, the reactor simulations indicate that LHSV is also an important parameter when designing catalytic dewaxing reactors, which value must be carefully chosen so that the isomerization yield is maximized while keeping acceptable values of cracking yield and total conversion for the profitable operation.

3.4.6. Effect of Feed Carbon Number

In order to verify the effect of heavy paraffinic feedstocks on the reactor performance, simulations were carried out considering additional feeds constituted by pure n-C₂₂ and n-C₂₄ and the results were compared to those obtained for n-hexadecane using the same operating conditions, which are shown in Figure 3-22.

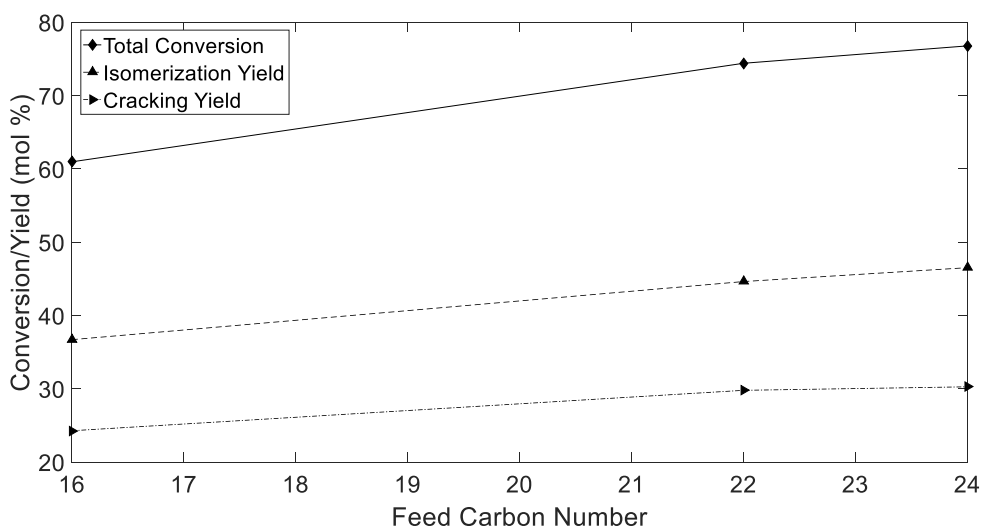


Figure 3-22: Effect of the feedstock carbon number on total conversion, isomerization, and cracking yields for LHSV = 0.4 h⁻¹, H₂/HC = 2.016, T = 298.03°C, and P = 69.96 bar

It can be observed that heavier paraffinic feedstocks lead to higher values of the total conversion, isomerization, and cracking yields. This can be explained by the fact that large hydrocarbons have higher reactivity once they undergo more isomerization and cracking elementary steps compared to the smaller ones. Similar results were observed by Kumar and Froment (2007) for conventional hydrocracking processes. Therefore, depending on the carbon number distribution of a diesel feed, heavy paraffinic molecules are going to be converted in higher extension than the smaller ones, which is in agreement with what is observed in industrial catalytic dewaxing operations.

3.4.7. Effect of Shape-Selectivity

In order to analyze the shape-selectivity features of the Pt/ZSM-5 catalyst, the Langmuir equilibrium constants were calculated at 249.32°C and compared to those calculated using the parameters estimated by Kumar (2004) for wide-pore Pt/US-Y zeolite catalyst used in conventional hydrocracking as shown in Table 3-8.

Table 3-7: Langmuir physisorption equilibrium constants for Pt/US-Y and Pt/ZSM-5 at T = 249.32°C

Physisorption Equilibrium Constant	Pt/US-Y [32]	Pt/ZSM-5
$K_{L,np}$	0.0822	0.3604
$K_{L,mp}$	0.2664	0.1751
$K_{L,dp}$	3.2089	4.9371×10^{-7}
$K_{L,tp}$	68.5223	7.8805×10^{-7}

It can be observed that the physisorption of normal paraffins are higher for Pt/ZSM-5 than for wide pore catalysts. Also, the monobranched species have comparable sorption features while dibranched and tribranched paraffinic compounds are weakly sorbed to the catalyst cages, which is in agreement with shape-selectivity theory once highly branched paraffins are sterically hindered into the catalyst pores.

3.5. Conclusion

In this work, the single-event kinetic modeling has been applied to estimate the kinetic parameters for the commercial Pt/ZSM-5 catalyst used in catalytic dewaxing reactors, which are independent on the feedstock type. A computer algorithm has been used to generate the reaction network comprising all the PCP-isomerization and β -scission elementary steps taking place at the catalyst surface. The shape-selectivity effects were incorporated based on rules proposed based on the key-lock and pore-mouth mechanisms in order to suppress elementary steps involving tertiary carbenium ions that are sterically hindered into the catalyst pores. A total of 14 independent parameters were estimated from experimental data for hydroconversion of n-hexadecane on Pt/ZSM-5 taken from literature using a multiphase reactor model. It has been observed from the reactor simulations that the cracking products and multibranched C₁₆ isomers are the secondary reaction products. Also, cracking reactions rates can become higher than those for PCP-isomerization when operating the reactor at high temperatures. Due to shape-selective nature of the catalyst, most of the reactions involving multibranched carbenium ions are suppressed and small amount of multibranched C₁₆ isomers are formed across the reactor. Finally, further reactor simulations confirmed that temperature, LHSV, and pressure are the main parameters affecting the catalytic dewaxing operation while the H₂/HC ratio only controls the rate at which the lighter compounds evaporates.

The kinetic parameters obtained in this work proved to be suitable to build a reactor model to design and optimize catalytic dewaxing reactors to improve the cold flow properties of

diesel fuels, which related product specification such as the cloud point temperature can be easily estimated from the estimated outlet mole flow rates.

Chapter 4

Development of a Diesel Cloud Point Soft-Sensor using Thermodynamic and Mechanistic Models

Eugenio Turco Neto, Syed Imtiaz, Salim Ahmed

Center for Risk, Integrity and Safety Engineering Group
Department of Process Engineering
Memorial University of Newfoundland, NL, St. John's, A1B 3X5, Canada.

4.1. Preface

This manuscript was submitted to the “Chemical Engineering Science” journal in February, 2017. The co-author of this work Dr. Salim Ahmed supervised the main author Eugenio Turco Neto through discussions regarding to the identification of the reactor operating conditions and bed lengths. The corresponding author Dr. Syed Imtiaz was the main supervisor of this work and provided all the knowledge and support about surrogate modelling.

4.2. Introduction

Catalytic dewaxing has become one of the major operations in oil refineries in North America due to the increasing demand on diesel fuels that can handle moderate to high temperature drop without causing wax formation during the winter season. The most used indicator to qualify the diesel cold flow properties is called cloud point, which is the highest

temperature at which the first wax crystal is formed in the fuel [2]. However, its measurement is still dependent on visual procedures defined by the standard ASTM D2500, which impacts the process control design stage due to the introduction of large time delays related to data acquisition and subjectiveness. In this context, a soft-sensor for on-line cloud point prediction would be beneficial not only to improve the quality control of the winterized diesel product but also to facilitate process design, optimization, and control of industrial catalytic dewaxing units.

Wax formation due to high concentration of long chain paraffins in petroleum fluids have been extensively studied and handled using the solid-liquid equilibrium theory. Pedersen (1995) proposed a vapor-liquid-solid thermodynamic model to describe the paraffinic wax formation process. The fugacity coefficients for liquid phase were evaluated using the Peng-Robinson equation of state while the fugacity for the compounds in solid phase were assumed to be a function of their fusion properties and pure state fugacity. The hydrocarbon fractions containing more than seven carbons in their molecular structure were grouped in a plus-fraction lump. This was further split into non-waxing and waxing forming fractions whose mole composition distributions were obtained through an empirical equation. Good agreement between experimental and predicted cloud point values was reported

Coutinho and Ruffier-Meray (1997) studied the solid-liquid region of heavy paraffinic solutions ranging from C_{19} to C_{48} dissolved in ethylbenzene using differential scanning calorimetry (DSC) to detect different solid phases. They proposed a thermodynamic model using the UNIFAC and Wilson models to describe the liquid and solid phases, respectively. For being predictive in nature, those models do not require parameter estimation, which is their main advantage. Good agreement between experimental and predicted values of cloud

point were reported. The authors also discussed the limitations of the Wilson model as it is not capable of describing well the mole composition distributions when multiple solid phases are formed.

Coutinho (2000) proposed a thermodynamic model that overcomes most of the issues found in previous methodologies and correlations used to describe wax formation, which are related to wrong assumptions regarding to the nature of the solid phase. By using the UNIQUAC model to describe the solid phase, the proposed thermodynamic model can predict well both cloud point value and mole composition distribution for solutions that formation of multiple solid phases is thermodynamically favorable. The authors compared the cloud point predictions with experimental values obtained for four jet fuels, two ship propulsion distillates, and three types of diesel fuels. In their analysis, branched paraffinic, naphthenic, and aromatic were grouped into a single lump based on the assumption that the PNA (paraffinic-naphthenic-aromatic) distribution or any other property of the fuel is available. They showed that the measured and calculated cloud point values as well as the mole composition distributions were in good agreement. Also, they showed that the results were independent of the type of pseudo-component used to represent the aromatic, naphthenic, and branched paraffinic compounds.

Ghanaei et al. (2007) formulated a thermodynamic model to predict the cloud point of hydrocarbon mixtures. The liquid phase was assumed to be ideal while the solid phase was described using the Wilson model. The effect of pressure on the cloud point was considered in the model by incorporating the Poynting correction in the solid phase fugacity formulation. The predicted values of cloud point were compared to experimental ones

obtained from binary mixtures consisting of C₁₄-C₁₅ and C₁₅-C₁₆ for different pressures ranging from 0.1 to 100 MPa, which were in good agreement.

In this work, a soft-sensor is proposed to predict on-line the cloud point of dewaxed diesel fuels produced from catalytic dewaxing reactors. Its framework integrates three different modules to estimate the product cloud point based on mechanistic models, reactor operating conditions, and feedstock distillation data. The sensor is then applied to study the performance of an industrial multi-bed reactor based on changes in the main process variables. Finally, a surrogate model is proposed to replace the mechanistic reactor and thermodynamic modules to reduce the sensor complexity and computing time so that it can be industrially implemented to perform on-line predictions. To carry out this step, a sequential design of experiments is used to properly handle the effect of nonlinearities on the accuracy of the surrogate model.

4.3. Cloud Point Soft-Sensor Design

4.3.1. Soft-Sensor Description

The schematic representation for the proposed cloud point soft-sensor is shown in Figure 4-1.

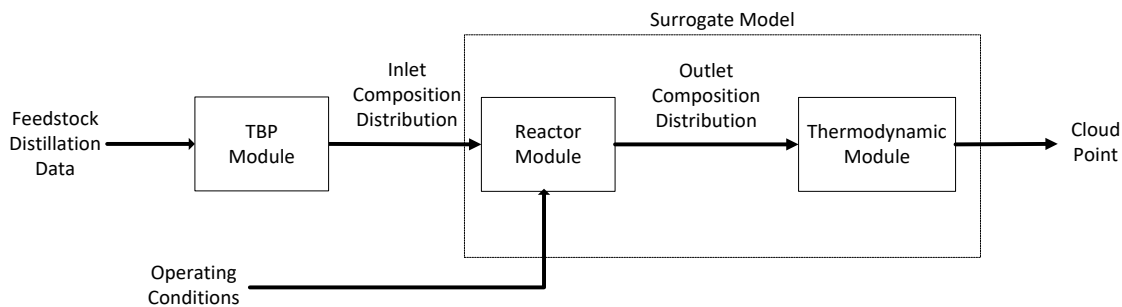


Figure 4-1: Schematic representation for the proposed cloud point soft-sensor framework

Each module in the sensor is described as follows:

- **TBP Module:** Receives the diesel feedstock distillation data and convert into detailed mole composition distribution in MTHS matrix form using the concepts described in section 4.3.2;
- **Reactor Module:** Reads the information regarding the process operating conditions and predicted inlet composition distribution. Then, these values are set as boundary conditions for the hydrodewaxing and hydrodesulfurization reactor models described in sections 4.3.3 and 4.3.4, respectively, to simulate the operation and predict the outlet composition of the diesel product;
- **Thermodynamic Module:** Accepts the simulated outlet composition distribution and uses this information as input for the solid-liquid equilibrium flash algorithm discussed in section 4.3.5 to estimate the cloud point of the dewaxed diesel product.

The integration of mechanistic models to predict the cloud point of dewaxed diesel fuels produced from catalytic dewaxing reactors has not been reported yet in literature and is one

of the main contributions of this work. It is assumed that all compounds in the diesel carbon range from C_8 to C_{24} are nearly fully recovered from the downstream separation processes so that the compositions required for the solid-liquid flash calculations are readily available after carrying out the reactor simulations. The reactor and thermodynamic modules are easily coupled to compute the cloud point of the dewaxed diesel for a given set of operating conditions and compositions.

However, the simulations can be computationally expensive due to the strong nonlinear behavior of the differential equations. Their complex functional form would also bring difficulties when implementing the sensor for on-line prediction purposes. To overcome these issues, the reactor and thermodynamic modules can be replaced by a simple surrogate model that is capable of reproducing the cloud point prediction when the sensor is intended to be used for on-line applications.

The first step in formulating a surrogate model is to define a design of experiments consisting of a small set of operating conditions and compositions to obtain few predictions using the original sensor framework so that initial information about the cloud point response becomes available. It can be done using either the one-shot or sequential design approaches.

In the one-shot approach, all the points in the experiment design are used at once to build the surrogate model [46]. The main drawback of this methodology lies on the fact that no information is available about the cloud point response before the reactor and thermodynamic simulations are carried out, and thereby, the ideal size for the design is unknown. Therefore, the design could either be oversampled and the advantages in using the surrogate model would be lost as solving the differential equations can be expensive or

undersampled resulting in an inaccurate surrogate model as the design would not properly cover the design space [47].

In the sequential design approach, additional points are iteratively added to an initial design of experiments based on the information obtained from the surrogate model built at the previous iteration [46]. In the context of this work, these extra samples must be added at regions where the cloud point response is nonlinear as those are usually harder to be described. The iterations are carried out until a convergence criterion based on the accuracy of the proposed surrogate model is reached. This technique does not require prior knowledge about the size of the design; however, it faces a trade-off problem related to the exploration and exploitation features [47].

The exploration feature induces the sequential design strategy to cover the model domain as uniformly as possible resulting in a global surrogate model capable of identifying all important regions containing nonlinearities or local optima in the surface response [47]. However, this methodology would fail in accurately describing those locations as it would not place enough points at those [47]. On the other hand, the exploitation capability would focus only on the nonlinear regions already identified at previous iterations and miss other ones not explored, which would result in a surrogate model that is only good for local predictions [46].

Therefore, building an on-line soft-sensor capable of providing global predictions as well as accurately describing highly nonlinear regions in the cloud point response is one of the main goals in this work. In this context, the fuzzy sequential design strategy proposed by van der Herten et al. (2015) was found to be suitable to achieve this objective, which is going to be described in sections 4.3.6 through 4.3.8.

4.3.2. Molecular Type and Homologous Series (MTHS) Matrix

In this work, the boundary conditions necessary to carry out the reactor simulations require detailed knowledge of the hydrocarbon mole distribution in the diesel feedstock. Even though advanced analytical techniques such as chromatography have considerably improved over the years, petroleum fractions are still being characterized using the ASTM-D86 distillation data and bulk properties such as specific gravity, cloud point, and viscosity. Hence, converting such compact and generalized information into detailed mole distribution is crucial to the soft-sensor development as the diesel properties vary from unit to unit as the streams can be blended before being sent to the catalytic dewaxing unit. However, these streams are usually constituted by thousands of hydrocarbons differing in type, sizing, and degree of branching, and thereby, such interconversion is not straightforward.

This task can be accurately done using a characterization technique initially proposed by Peng (1999). The approach consists on representing the compositions of a refining stream in matrix form denominated Molecular Type and Homologous Series (MTHS). Its columns represent the type of molecules that can be possibly found in a diesel stream such as paraffins, naphthenes, and aromatics while the rows represent their molecular size based on the carbon number [49]. For each molecular type and carbon number, several model compounds have been assigned based on synthetic and real diesel molecular information provided by Froment et al. (1994) and Ahmad et al. (2011). The entries in the matrix represent their overall mole fractions and are the unknown variables to be determined.

To illustrate the application of this approach to build the TBP module, the bulk information for an industrial diesel feedstock provided by a local refinery showed in Table 4-1 is used.

Table 4-1: Distillation curve and bulk properties for an industrial diesel feedstock

ASTM-D86 Distillation Curve (vol % distilled) (°F)	
Initial Boiling Point (IBP)	307.2
10%	412.3
30%	458.4
50%	493
70%	527.4
90%	564.1
Final Boiling Point (FBP)	617.2
Bulk Physical Properties	
Specific Gravity	0.8435
Cloud Point (°C)	-23.78
Sulfur Content (ppm)	4817.9
Nitrogen Content (ppm)	56.32
Paraffinic-Naphthenic-Aromatic (PNA) Analysis	
Paraffinic Content (mol%)	42.57
Naphthenic Content (mol%)	30.25
Aromatic Content (mol%)	27.18

It was observed from the industrial data that this feedstock was a blend of several heavy and light diesel streams produced from different units such as fluid catalytic cracking (FCC) and hydrocracking. Therefore, model compounds with carbon number ranging from C₈ to C₂₄ were considered to describe this industrial feed. The values for the average molecular weight and PNA compositions were estimated for this feedstock using correlations taken from American Petroleum Institute (1997). In order to obtain the entries of the MTHS matrix, an optimization procedure was used to minimize the objective function given by Equation 4-1 [49].

$$\begin{aligned}
 F = & \left(\frac{SG^{cal} - SG^{ind}}{SG^{ind}} \right)^2 + \left(\frac{M^{cal} - M^{ind}}{M^{ind}} \right)^2 + \left(\frac{x_S^{cal} - x_S^{ind}}{x_S^{ind}} \right)^2 + \left(\frac{x_{Nap}^{cal} - x_{Nap}^{ind}}{x_{Nap}^{ind}} \right)^2 \\
 & + \left(\frac{x_{aro}^{cal} - x_{aro}^{ind}}{x_{arom}^{ind}} \right)^2 + \left(\frac{x_{par}^{cal} - x_{par}^{ind}}{x_{par}^{ind}} \right)^2 + \sum_{i=1}^7 \left(\frac{V_{TBP,i}^{cal} - V_{TBP,i}^{ind}}{V_{TBP,i}^{ind}} \right)^2
 \end{aligned} \tag{4-1}$$

This equation represents the deviation between the industrial values for the properties in the Table 4-2 and the ones calculated using the optimal mole fraction distribution obtained from the minimization problem. The specific gravity can be evaluated by Equation 4-2 [49].

$$\frac{1}{SG^{cal}} = \sum_{i,j} \frac{w_{i,j}}{SG_{i,j}} \tag{4-2}$$

The density at 60°F for each model compound was calculated using Peng-Robinson equation of state and their individual critical properties were obtained using Joback's group contribution method [40]. The average molecular weight of the simulated diesel feed was obtained through Equation 4-3 [49].

$$M^{cal} = \sum_{i,j} x_{i,j} M_{i,j} \tag{4-3}$$

Finally, the total mole fraction of paraffins, aromatics, naphthenes, and sulfur compounds can be easily computed using Equation 4-4 [51]. It is important to mention that benzothiophene and 4,6-dimethyldibenzothiophene were assigned as model compounds to represent the sulfur content as they are extensively considered to formulate mechanistic kinetic models developed to simulate hydrotreating reactors.

$$x_j^{cal} = \sum_i x_{i,j} \quad (4-4)$$

The last term in Equation 4-1 represents the deviations related to industrial and calculated TBP curves. First, the ASTM D-86 distillation data from Table 4-1 is converted into TBP distillation curve using interconversion relationships found in the American Petroleum Institute (1997). Then, the cumulative percent volume distilled is calculated by sorting the normal boiling point temperature in ascending order with respect to volume fraction of each model compound and applying the cumulative summation [51].

To solve this optimization problem, two linear constraints must be imposed to obtain a realistic mole composition distribution. The first one is based on the fact that the sum of the mole fractions in the MTHS matrix must be equal to one as mathematically shown by Equation 4-5.

$$\sum_{i,j} x_{i,j} = 1 \quad (4-5)$$

The last constraint is related to the total nitrogen content in the diesel feed. As only quinoline has been assigned as model compound to represent the nitrogen content, its composition in the matrix must be equal to the total nitrogen content provided in Table 4-1.

The optimization problem was solved using the interior-point algorithm available in the MATLAB[®] optimization toolbox and the results are summarized in Table 4-2. The calculated cloud point value was obtained by applying the thermodynamic module described in section 4.3.5. The obtained MTHS matrix is shown in Appendix A-1.

Table 4-2: Validation results obtained from the MTHS algorithm

Property	Industrial Value	Calculated Value
MeABP (°C)	249.74	256.46
Cloud Point (°C)	-23.78	-23.42
Sulphur Content (ppm)	4817.9	4807.96
Paraffinic Content (mol%)	42.57	42.62
Naphthenic Content (mol%)	30.25	30.21
Aromatic Content (mol%)	27.18	27.17

It can be observed that the composition distribution along with selected model compounds were satisfactory to model the diesel feed with good accuracy. Figure 4-2 shows a comparison between calculated and industrial TBP curves confirming the accuracy of the methodology applied.

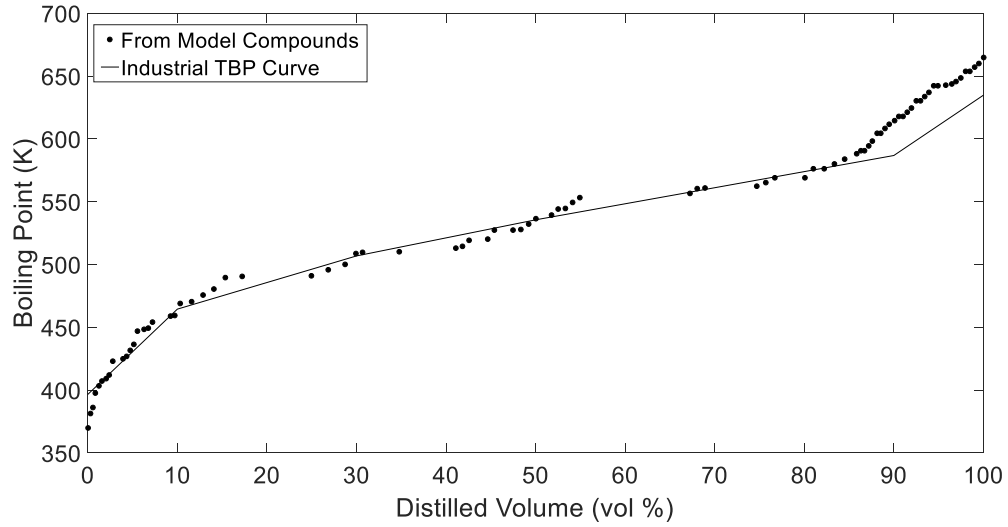


Figure 4-2: Comparison between industrial and calculated TBP curves

4.3.3. Hydrodewaxing (HDW) Reactor Model

The catalytic dewaxing reactor model is formulated based on the single event theory proposed by Froment and co-workers [7, 13, 14, 32]. In this approach, the rate constant is expressed as shown by Equation 4-6.

$$k = \left(\frac{\sigma_{gl}^r}{\sigma_{gl}^\#} \right) \left(\frac{k_B T}{h} \right) \exp\left(\frac{\Delta \hat{S}^{0\#}}{R} \right) \exp\left(-\frac{\Delta H^{0\#}}{RT} \right) \quad (4-6)$$

The first term in this equation represents the ratio between the global symmetry numbers for reactant and activated complex, which is denominated number of single events (n_e) and accounts for the effects related to the changes in molecular structure due to chemical reaction. The other terms are related to changes in intrinsic enthalpy and entropy and can

be lumped into the so-called single event rate constant (\tilde{k}), which is independent of the feedstock type. Hence, the Equation 4-6 can be rewritten as given by Equation 4-7 [32].

$$k = n_e \tilde{k} \quad (4-7)$$

The shape-selective cracking and isomerization are the main reactions taking place within the catalytic dewaxing unit, which follow the mechanisms governed by the carbenium ion chemistry. Those reactions are usually carried out on bifunctional shape-selective catalysts such as Pt/ZSM-5, which contain metal sites responsible for the formation of intermediate olefins due to dehydrogenation reactions and acid sites where the cracking and isomerization steps take place. The common elementary steps promoted by metal and acid sites on Pt/ZSM-5 are shown in Table 4-3.

Table 4-3: Common elementary steps promoted by metal and acid sites on Pt/ZSM-5

Dehydrogenation/Hydrogenation	
Protonation/Deprotonation	
Hydride shift	
β -scission	
PCP isomerization	

By assuming ideal hydrocracking conditions, the reaction network proposed by Baltanas and Froment (1985) was used to obtain all the individual elementary steps assuming that the reactions taking place at the metal sites are fast enough to be considered in pseudo-equilibrium. The shape-selectivity effects were incorporated into the reaction network by eliminating reactions involving reactants or products whose molecular structures are sterically hindered in the pore-mouths and micropores of the catalyst. The methyl-shift reactions were also suppressed as shifting the methyl branches can induce the ion to move outside the pore-mouth, which is not consistent with the reaction mechanism [22]. Better descriptions of these assumptions are given by Laxis Narasimham et al. (2003). Finally, the posteriori-lumping technique is used to lump the individual compounds identified in the reaction network into common groups based on the carbon number and degree of branching, whose internal composition distribution is governed by the thermodynamic equilibrium [6]. The rate expressions considered in this work to compute the net rate of formation for the components reacting in the HDW bed are given by Equations 4-8 through 4-10 [32].

$$R_{L_m, J_{m,w}}^{Cons} = LCC_{L_m, J_{m,w}} \frac{\tilde{k}_l^*(m, w) K_{L, L_m} C_{L_m}^L}{C_{H_2}^L \left[1 + \sum_i K_{L, L_m} C_{L_m}^L \right]} \quad (4-8)$$

$$R_{L_m, L_k, J_{m,w}}^{Form} = \sum_k LCF_{L_m, L_k, J_{m,w}} \frac{\tilde{k}_l^*(m, w) K_{L, L_k} C_{L_k}^L}{C_{H_2}^L \left[1 + \sum_i K_{L, L_k} C_{L_k}^L \right]} \quad (4-9)$$

$$R_{L_m, net}^{Form} = \sum_{l=1}^{n_l} \left(R_{L_m}^{Form} - R_{L_m}^{Cons} \right) \quad (4-10)$$

The Lumping Coefficients of Formation (LCF) and Consumption (LCC) can be calculated using the information obtained from the reaction network through Equations 4-11 and 4-12, respectively [32].

$$LCF_{L_m, L_k, l_{m,w}} = \sum_{q=1}^{q_T} n_{e,q} y_{i,L_k} \frac{1}{n} \left(\frac{\sigma_{P_i}^{gl}}{\sigma_{O_j}^{gl} \sigma_{H_2}^{gl}} \right) \sum_{j=1}^n \tilde{K}_{DH}^{(P_i \leftrightarrow O_j)} \tilde{K}_{isom}^{(O_j \leftrightarrow O_r)} \quad (4-11)$$

$$LCC_{L_m, l_{m,w}} = \sum_{q=1}^{q_T} n_{e,q} y_{i,L_m} \frac{1}{n} \left(\frac{\sigma_{P_i}^{gl}}{\sigma_{O_j}^{gl} \sigma_{H_2}^{gl}} \right) \sum_{j=1}^n \tilde{K}_{DH}^{(P_i \leftrightarrow O_j)} \tilde{K}_{isom}^{(O_j \leftrightarrow O_r)} \quad (4-12)$$

The single event kinetic parameters for catalytic dewaxing on Pt/ZSM-5 were obtained in our previous work [52] and are used to propose the hydrodewaxing reactor model in this section.

It is assumed that both gas and liquid phases flow down along the hydrodewaxing catalytic bed in plug flow pattern and that the catalyst particles are completely surrounded by liquid. The reactions involved in the catalytic dewaxing mechanism are usually endothermic; however, the overall conversion in this process usually ranges from low to moderate values to avoid yield losses. Therefore, it is assumed that the hydrodewaxing bed is nearly isothermal and the continuity equations required to obtain the composition profiles for a given lump in both gas and liquid phases are expressed by Equations 4-13 and 4-14, respectively [7].

$$\frac{1}{A} \frac{dF_i^G}{dz} = -k_{o,i} a_v \left(\frac{C_i^G}{K_i^{C,VLE}} - C_i^L \right) \quad \text{at } z = 0, F_i^G = F_{i,0}^G \quad (4-13)$$

$$\frac{1}{A} \frac{dF_i^L}{dz} = k_{o,i} a_v \left(\frac{C_i^G}{K_i^{C,VLE}} - C_i^L \right) + R_{i,net}^{form} \quad \text{at } z = 0, F_i^L = F_{i,0}^L \quad (4-14)$$

By considering the two-film theory to model gas-liquid interphase mass transfer, the overall mass transfer coefficient can be calculated based on the individual mass transfer film coefficients for both liquid and gas sides using Equation 4-15 [32].

$$\frac{1}{k_{o,i}a_v} = \frac{1}{K_i^{C,VLE} k_G a_v} + \frac{1}{k_L a_v} \quad (4-15)$$

These coefficients were estimated using the correlations proposed by Reiss (1967) and Sato et al. (1972), respectively. The equilibrium coefficient in concentration basis expressed by Equation 4-16 can be written as function of the true vapor-liquid equilibrium constant, which is calculated using the Peng-Robinson equation of state [35].

$$K_i^{C,VLE} = K_i^{VLE} \frac{\rho_{molar}^G}{\rho_{molar}^L} \quad (4-16)$$

This set of differential equations were solved using the Backward Differentiation Formula (BDF) available in MATLAB[®] to obtain the composition profiles along the HDW bed and the model was checked in our previous work [52].

4.3.4. Hydrodesulfurization Reactor Model

4.3.4.1. Reaction Network

In this work, the commercial CoMo/Al₂O₃ was selected as the catalyst to be used for hydrodesulfurization (HDS) in order to eliminate the sulfur compounds that can poison the dewaxing catalyst while producing Ultra Low Sulfur Diesel (ULSD). This catalyst contains two types of active sites [53]:

- The σ -sites where hydrogenolysis reactions take place, which are responsible for extracting the sulfur atom from the reactant molecular structure;
- The τ -sites where hydrogenation reactions take place, which are responsible for the saturation of the aromatic rings found in the molecular structure of sulfur compounds;

The model compounds used to represent the overall sulfur content in the diesel feedstock were dibenzothiophene and 4,6-dimethyldibenzothiophene as discussed in section 4.3. The reaction mechanism governing the conversion of dibenzothiophene to cyclohexylbenzene and H_2S was proposed by Vanrysselberghe and Froment (1996) as shown in Figure 4-3.

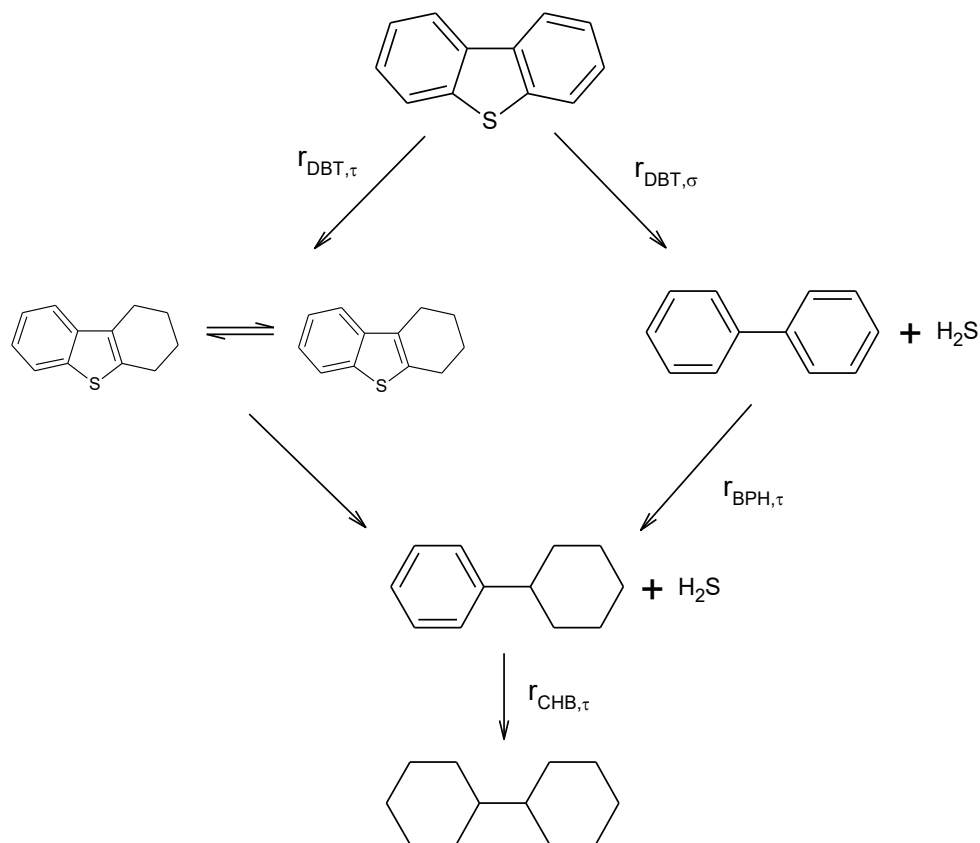


Figure 4-3: Mechanism for hydrodesulfurization of dibenzothiophene [54]

Likewise, the mechanism for the hydrodesulfurization of 4,6-dimethyldibenzothiophene, which is converted into bicyclohexyl, 3,3'-dimethylbicyclophenyl, and H₂S was proposed by Vanrylsselberghe and Froment (1998) and is illustrated by Figure 4-4.

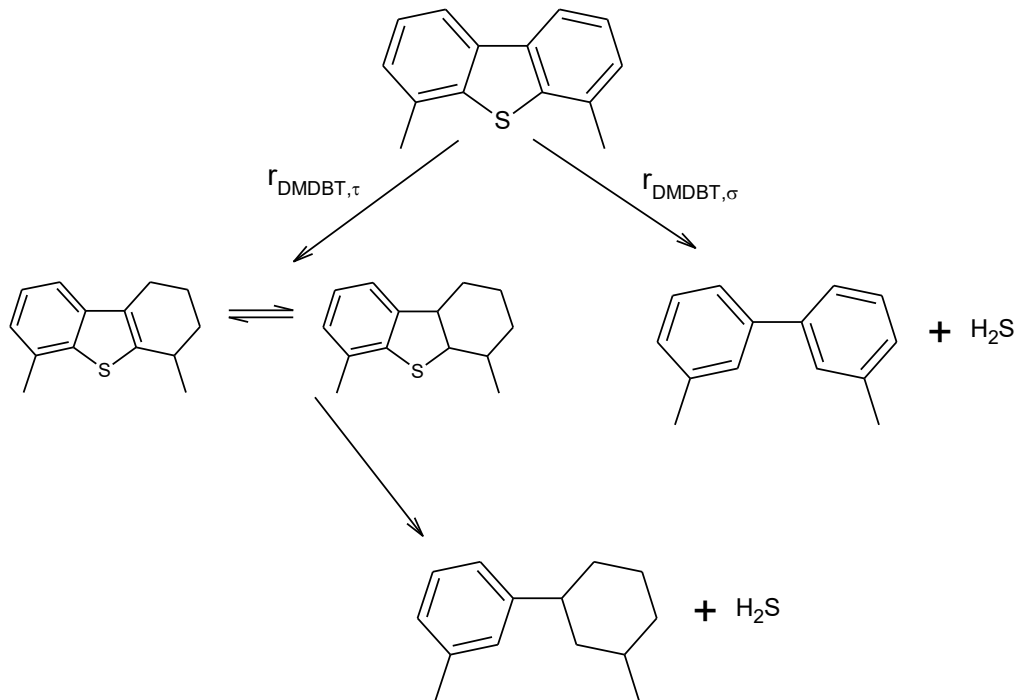


Figure 4-4: Mechanism for hydrodesulfurization of 4,6-dimethyldibenzothiophene [55]

According to Vanrylsselberghe and Froment (1998), the technical limitations in producing ULSD can be explained by the slow conversion of 4,6-dimethyldibenzothiophene as the methyl groups attached to its aromatic rings block the sulfur atom from being adsorbed at the active sites of the catalyst. These reactions were used as the basis to obtain the values of the net rate of consumption for each component involved in the HDS reaction mechanism. The rate equations and kinetic parameters are going to be discussed in the next section.

4.3.4.2. Kinetic Parameters and Rate Equations

The Hougen-Watson rate equations and kinetic parameters related to the previously discussed hydrodesulfurization mechanisms were taken from several sources available in the literature. The rate equations as well as the rate and adsorption equilibrium constants are shown in Tables 4-4 through 4-7.

Table 4-4: Hougen-Watson rate equations for the main reactions taking place in HDS process [54, 55]

Reaction Type	Hougen-Watson Rate Equation
Hydrogenolysis of dibenzothiophene	$r_{DBT,\sigma} = \frac{k_{DBT,\sigma} K_{DBT,\sigma} K_{H,\sigma} C_{DBT} C_{H_2}}{DEN_{\sigma}} \quad (4-17)$
Hydrogenation of dibenzothiophene	$r_{DBT,\tau} = \frac{k_{DBT,\tau} K_{DBT,\tau} K_{H,\tau} C_{DBT} C_{H_2}}{DEN_{\tau}} \quad (4-18)$
Hydrogenation of biphenyl	$r_{BPH,\tau} = \frac{k_{BPH,\tau} K_{BPH,\tau} K_{H,\tau} C_{BPH} C_{H_2}}{DEN_{\tau}} \quad (4-19)$
Hydrogenation of cyclohexylbenzene	$r_{CHB,\tau} = \frac{k_{CHB,\tau} K_{CHB,\tau} K_{H,\tau} C_{CHB} C_{H_2}}{DEN_{\tau}} \quad (4-20)$
Hydrogenolysis of 4,6-dimethyl-dibenzothiophene	$r_{DMBT,\sigma} = \frac{k_{DMBT,\sigma} K_{DMBT,\sigma} K_{H,\sigma} C_{DMBT} C_{H_2}}{DEN_{\sigma}} \quad (4-21)$
Hydrogenation of 4,6-dimethyl-dibenzothiophene	$r_{DMBT,\tau} = \frac{k_{DMBT,\tau} K_{DMBT,\tau} K_{H,\tau} C_{DMBT} C_{H_2}}{DEN_{\tau}} \quad (4-22)$

Table 4-5: Arrhenius expressions for the rate constants for the HDS mechanisms [54, 55]

Rate Constant	Arrhenius Expression
$k_{DBT,\sigma}$	$2.44336 \times 10^{10} \exp\left[-\frac{122770}{RT}\right]$ (4-23)
$k_{DBT,\tau}$	$2.86757 \times 10^{16} \exp\left[-\frac{186190}{RT}\right]$ (4-24)
$k_{BPH,\tau}$	$3.4112 \times 10^{23} \exp\left[-\frac{255714}{RT}\right]$ (4-25)
$k_{CHB,\tau} K_{CHB,\tau}$	3.38631×10^{-1}
$k_{DMDBT,\sigma}$	$6.4456 \times 10^7 \exp\left[-\frac{106223}{RT}\right]$ (4-26)
$k_{DMDBT,\tau}$	$3.68208 \times 10^{27} \exp\left[-\frac{299042}{RT}\right]$ (4-27)

Table 4-6: Van't Hoff expressions for the adsorption equilibrium constants for the HDS mechanisms [54, 55]

Adsorption Equilibrium Constant	Van't Hoff Expression
$K_{H,\sigma}$	$3.36312 \times 10^{-11} \exp\left[\frac{113232}{RT}\right]$ (4-28)
$K_{H,\tau}$	$1.40255 \times 10^{-15} \exp\left[\frac{142693}{RT}\right]$ (4-29)
$K_{H_2S,\sigma}$	$1.47118 \times 10^{-8} \exp\left[\frac{105670}{RT}\right]$ (4-30)
$K_{DBT,\sigma}$	7.5686×10^1
$K_{DBT,\tau}$	$2.50395 \times 10^{-7} \exp\left[\frac{76840}{RT}\right]$ (4-31)
$K_{BPH,\tau}$	$4.96685 \times 10^{-4} \exp\left[\frac{37899}{RT}\right]$ (4-32)
$K_{DMBT,\sigma}$	1.80397×10^1
$K_{DMBT,\tau}$	$1.58733 \times 10^{-8} \exp\left[\frac{90485}{RT}\right]$ (4-33)

The denominator in the rate equations can be expressed by Equations 4-34 and 4-35 [54, 55]

$$DEN_{\sigma} = \left(\frac{1 + K_{DBT,\sigma} C_{DBT} + K_{BPH,\sigma} C_{BPH} + \sqrt{K_{H,\sigma} C_{H_2}} + K_{H_2S,\sigma} C_{H_2S}}{K_{DMBT,\sigma} C_{DMBT}} \right)^3 \quad (4-34)$$

$$DEN_{\tau} = \left(1 + K_{DBT,\tau} C_{DBT} + K_{BPH,\tau} C_{BPH} + \sqrt{K_{H,\tau} C_{H_2}} + K_{DMDBT,\tau} C_{DMDBT}\right)^3 \quad (4-35)$$

Hence, by analyzing the reaction mechanisms and rate expressions, the stoichiometric table required to calculate the net rate of consumption for the several compounds involved in the hydrodesulfurization process can be built as presented in Table 4-7.

Table 4-7: Stoichiometric table for hydrodesulfurization reactions

	$r_{DBT,\sigma}$	$r_{DBT,\tau}$	$r_{BPH,\tau}$	$r_{CHB,\tau}$	$r_{DMDBT,\sigma}$	$r_{DMDBT,\tau}$
H ₂	1	1	0	0	1	1
H ₂ S	-2	-5	-3	-3	-2	-5
DBT	-1	-1	0	0	0	0
BPH	1	0	-1	0	0	0
CHB	0	1	1	-1	0	0
DMDBT	0	0	0	0	-1	-1
DMBPH	0	0	0	0	1	0
MCHT	0	0	0	0	0	1

The entries in Table 4-7 represent the stoichiometric coefficients for the different components reacting through the pathway indicated by reaction rate. Negative and positive numbers are related to reactants and products, respectively, while zero is used to indicate that a compound is not reacting in that pathway.

4.3.4.3. Reactor Model

The continuity and energy equations required to describe the conversion process in a HDS catalytic bed is similar to those presented to model the catalytic dewaxing one. To simplify the problem, the diffusion limitations in the catalyst pellet as well as the resistance to mass transport from the bulk of liquid phase to the surface of the pellet are not considered. Hence, the continuity equation for a given compound in liquid phase accounting for interphase mass transfer and reaction kinetics is expressed by Equations 4-36 [50].

$$\frac{1}{A} \frac{dF_i^L}{dz} = k_{o,i} a_v \left(\frac{C_i^G}{K_i^{C,VLE}} - C_i^L \right) - R_{i,HDS}^{net} (1 - \varepsilon_b) \quad \text{at } z = 0, F_i^L = F_{i,0}^L \quad (4-36)$$

Also, the continuity equation for the same component in gas phase is identical to the one presented by Equation 4-13. The net rate of consumption expressed by Equation 4-37 can be calculated using stoichiometry table and the Hougen-Watson rate expressions discussed in section 4.5.2 [56].

$$R_{i,HDS}^{net} = -\rho_P \sum_{j=1}^{N_R} S[i, j] r_j \quad (4-37)$$

The energy equations used to obtain the temperature distributions for gas and liquid phases are expressed by Equations 4-38 and 4-39, respectively, which account for the interphase convective heat transport and the heat effects due to the exothermic reactions [50]. Also, it is assumed that the temperature at the gas-liquid interface is equal to the one at liquid phase as the heat generated in the catalyst due to the HDS reactions is quickly transferred to this phase.

$$u_G \rho_G C_{pG} \frac{dT_G}{dz} = h_G a_v (T_L - T_G) + \sum_{i=1}^N N_i a_v C_{piG} (T_G - T_L) \quad \text{at } z = 0, T_G = T_{G,0} \quad (4-38)$$

$$u_L \rho_L C_{pL} \frac{dT_L}{dz} = \rho_B \sum_{j=1}^{N_R} r_j (-\Delta H_{Rj}) + \sum_{i=1}^N N_i a_v \Delta H_{vi} \quad \text{at } z=0, T_L = T_{L,0} \quad (4-39)$$

The gas phase heat capacity for each model compound was estimated applying the correlations given by Poling et al. (2001), which were then used along with the Peng-Robinson equation of state to calculate the heat capacity for the gas mixture. The interphase heat transfer coefficient was evaluated using the Chilton-Colburn analogy [35]. Finally, the heat of vaporization and formation for each component were obtained using the Joback's group contribution method [40]. The composition and temperature profiles along the HDS bed were obtained by solving set of differential equations represented by Equations 4-36 through 4-39, which were implemented and solved in MATLAB[®] using the Backwards Differentiation Formula (BDF) approach.

4.3.5. Solid-Liquid Equilibrium Thermodynamic Model

When the cloud point of a diesel mixture is reached, the first solidified paraffinic crystals are in thermodynamic equilibrium with the liquid phase. Therefore, the phase equilibrium criterion given by Equation 4-40 must be satisfied.

$$\hat{f}_i^L = \hat{f}_i^S \quad (4-40)$$

The fugacity of a given component can be written in terms of its activity coefficient and fugacity at pure state. Therefore, Equation 4-41 can be rearranged into Equation 4-43 [29].

$$x_i^L \gamma_i^L f_{i,pure}^L = x_i^S \gamma_i^S f_{i,pure}^S \quad (4-41)$$

The solid-liquid equilibrium constant can be calculated by rewriting Equation 4-41 into Equation 4-42, which determines how a particular compound is distributed between the phases [29].

$$K_i^{SL} = \frac{x_i^S}{x_i^L} = \frac{\gamma_i^L f_{i,pure}^L}{\gamma_i^S f_{i,pure}^S} \quad (4-42)$$

As confirmed by Coutinho (2000), isoparaffinic, aromatic, and naphthenic compounds act as solvent and have almost negligible impact on the cloud point temperature. Therefore, their composition can be lumped and represented by a single isoparaffinic pseudo-component selected to match the average molecular weight of the diesel fuel. Also, the solid phase is assumed to be only consisted of normal paraffins and the pseudo-component is avoided in this phase by setting its fugacity at pure state in Equation 4-42 to a large value as suggested by Pedersen (1995).

The fugacity ratio of each paraffinic component can be expressed as function of the fusion properties using an expression proposed by Coutinho (2000) and then modified by Ghanaei et al. (2007) represented by Equation 4-43.

$$\ln \frac{f_{i,pure}^S}{f_{i,pure}^L} = \frac{\Delta H_i^f}{RT_i^f} \left(1 - \frac{T_i^f}{T} \right) + \frac{1}{RT} \int_T^{T_i^f} \Delta C_{p,i}^{LS} dT - \frac{1}{R} \int_T^{T_i^f} \Delta C_{p,i}^{LS} \frac{dT}{T} + \frac{1}{RT} \int_P^{P_i^f} \Delta V_i dP \quad (4-43)$$

This equation represents the changes in enthalpy and entropy during the solidification process of a pure compound. The fusion enthalpy and temperature as well as the phase change heat capacity were estimated using the Equations 4-44 through 4-46 proposed by Won (1989) and Broadhurst (1962).

$$\Delta H_i^f = 0.1426M_i T_i^f \quad (4-44)$$

$$T_i^f = \begin{cases} 0.040C_n^3 - 2.2133C_n^2 + 46.197C_n - 45.777 & C_n < C_{16} \\ 0.0028C_n^3 - 0.3185C_n^2 + 13.559C_n + 143.15 & C_n \geq C_{16} \end{cases} \quad (4-45)$$

$$\Delta C_{P,i}^{LS} = 0.3033M_i T_i^f - 4.635 \times 10^{-4} M_i T_i^f \quad (4-46)$$

The last term in Equation 4-43 is denominated Poynting correction and represents the effect of pressure in the thermodynamic model [29]. In this work, this term has been neglected as the cloud point measurements are usually made at atmospheric pressure.

As the diesel product leaving the catalytic dewaxing reactor consists of several hydrocarbons differing in terms of size and degree of branching, non-ideal behavior is expected for both solid and liquid phases. Therefore, the activity coefficients for the components in liquid phase can be evaluated using Equation 4-47 [59].

$$\ln \gamma_i^L = \ln \gamma_i^{res} + \ln \gamma_i^{fv} \quad (4-47)$$

The first term in Equation 4-47 was evaluated using the UNIFAC model, which accounts for energetic interactions among the molecules [59]. The second one was calculated using Flory-free volume equation represented by Equation 4-48 and describes the effect of molecular size on the activity coefficient [59].

$$\ln \gamma_i^{fv} = \ln \frac{\phi_i}{x_i^L} + 1 - \frac{\phi_i}{x_i^L} \quad (4-48)$$

Where:

$$\phi_i = \frac{x_i^L \left(V_i^{1/3} - V_{wi}^{1/3} \right)}{\sum_j x_j^L \left(V_j^{1/3} - V_{wj}^{1/3} \right)} \quad (4-49)$$

The parameter V_{Wi} is the van der Waals volume for a pure compound and can be determined by the group contribution method proposed by Bondi (1968). The activity coefficients for the compounds in solid phase are estimated using the predictive Wilson model given by Equation 4-50 [29].

$$\ln \gamma_i^S = 1 - \ln \left(\sum_j x_j^S \Lambda_{ij} \right) - \sum_k \frac{x_k^S \Lambda_{kj}}{\sum_j x_j^S \Lambda_{kj}} \quad (4-50)$$

Where:

$$\Lambda_{ij} = \exp \left(- \frac{\lambda_{ij} - \lambda_{ii}}{RT} \right) \quad (4-51)$$

Equation 4-51 represents the characteristic energy parameter that is a function of the interaction energy for a pair of similar or different molecules, which can be evaluated by Equations 4-52 and 4-53, respectively [29].

$$\lambda_{ii} = - \frac{2}{6} (\Delta H_{sub,i} - RT) \quad (4-52)$$

$$\lambda_{ij} = \lambda_{ji} = \lambda_{jj} \quad (4-53)$$

The index “j” in Equation 4-52 represents the smallest normal alkane in the pair being compared. The sublimation enthalpy can be estimated using Equation 4-54 [29].

$$\Delta H_{sub,i} = \Delta H_{vap,i} + \Delta H_i^f + \Delta H_{tr,i} \quad (4-54)$$

The heat of vaporization in Equation 4-56 was evaluated using the correlation proposed by Morgan and Kobayashi (1994) given by Equations 4.55 through 4-61.

$$x = 1 - \frac{T}{T_C} \quad (4-55)$$

$$\Delta H_v^0 = 5.2804x^{0.3333} + 12.865x^{0.8333} + 1.171x^{1.2083} - 13.116x + 0.4858x^2 - 1.088x^3 \quad (4-56)$$

$$\Delta H_v^1 = 0.80022x^{0.3333} + 273.23x^{0.8333} + 465.08x^{1.2083} - 638.5x - 145.12x^2 + 74.049x^3 \quad (4-57)$$

$$\Delta H_v^2 = 7.2543x^{0.3333} - 346.45x^{0.8333} - 610.48x^{1.2083} + 839.89x + 160.05x^2 - 50.71x^3 \quad (4-58)$$

$$\frac{\Delta H_{vap}}{RT_C} = \Delta H_v^0 + \omega \Delta H_v^1 + \omega^2 \Delta H_v^2 \quad (4-59)$$

Finally, the transition enthalpy in Equation 4-54 can be calculated using the correlation formulated by Broadhurst (1962) represented by Equation 4-60.

$$\Delta H_{tr} = \begin{cases} 0.0009C_n^3 + 0.0011C_n^2 + 0.1668C_n + 3.693 & C_n < C_{19} \\ -0.0032C_n^3 + 0.2353C_n^2 - 3.912C_n + 25.261 & C_n \geq C_{19} \end{cases} \quad (4-60)$$

The solid-liquid flash algorithm proposed by Ghanaei et al. (2007) represented by the block diagram in Figure 4-5 was implemented in MATLAB[®] to perform the phase equilibrium calculations required to calculate the cloud point temperature.

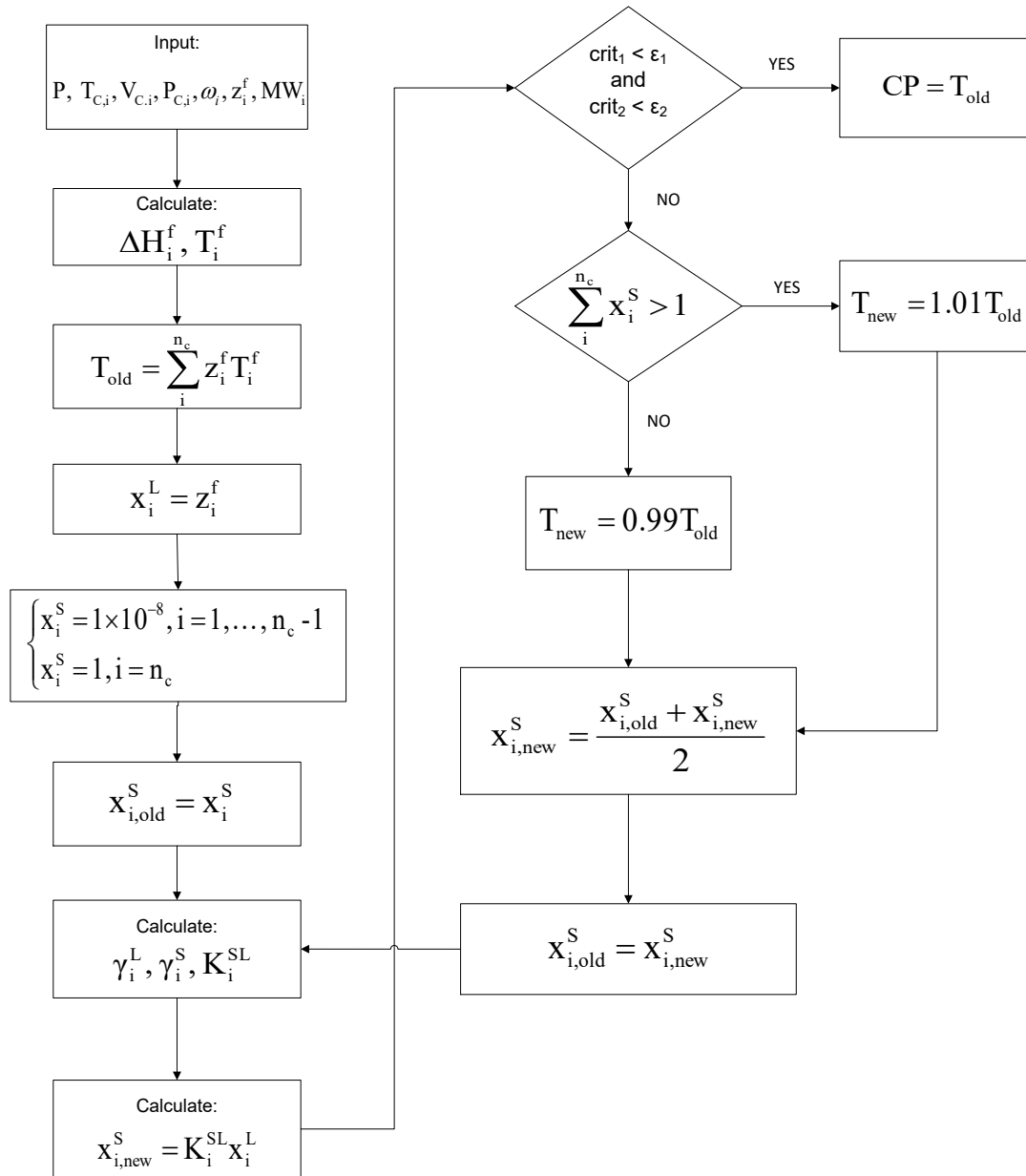


Figure 4-5: Solid-Liquid Equilibrium Calculation Algorithm [29]

The two convergence criteria used in this algorithm are expressed by Equation 4-61 and 4-62 [29].

$$crit_1 = \left| \sum_i x_i^S - 1 \right| \quad (4-61)$$

$$crit_2 = \max \left| \frac{x_{i,new}^S - x_{i,old}^S}{x_{i,old}^S} \right| \quad (4-62)$$

To check if the algorithm was correctly implemented, the experimental values of cloud point for two diesel feedstocks presented by Coutinho et al. (2000) were compared to the calculated ones, which are shown in Table 4-8.

Table 4-8: Validation of solid-liquid equilibrium algorithm for cloud point estimation

Diesel Feedstock	Experimental Cloud Point [59]	Calculated Cloud Point
Non-desulfurized	4.3°C	4.48°C
Desulfurized	5.5°C	4.86°C

Besides the measurement errors related to the experimental data, the deviations between experimental and calculated cloud point values can also be explained based on the accuracy of the correlations used to estimate the fusion properties of the pure compounds.

4.3.6. Fuzzy Local Linear Approximation (FLOLA)

The Local Linear Approximation (LOLA) algorithm was initially developed by Crombecq et al. (2011) and is widely used in the framework of several sequential design strategies to efficiently describe regions where a given function can be possibly nonlinear. In this approach, the region surrounding the high fidelity model response evaluated at a given

design point is linearized and the approximation error is taken as the metric to measure the degree of nonlinearity. In order to explain this methodology, consider the experiment design X with n_p points. Let \mathbf{x}_r be a reference design point with d components, whose vector representation is given by Equation 4-63 [47].

$$\mathbf{x}_r = [x_r^{(1)}, \dots, x_r^{(d)}] \quad (4-63)$$

In the context of this work, each component of this vector can represent a process variable such as pressure, temperature or composition of a compound of interest as will be discussed in the following sections. The region formed by a set containing the v nearest samples surrounding \mathbf{x}_r is called neighborhood and is represented in vector form by Equation 4-64 [47].

$$N(\mathbf{x}_r) = [\mathbf{x}_{r,1}, \dots, \mathbf{x}_{r,v}] \quad (4-64)$$

Hence, if the neighborhood of \mathbf{x}_r is known, the actual model response can be linearized by solving the least squares problem represented by Equation 4-65 [47].

$$\begin{bmatrix} x_{r,1}^{(1)} - x_r^{(1)} & \dots & x_{r,1}^{(d)} - x_r^{(d)} \\ \vdots & \ddots & \vdots \\ x_{r,v}^{(1)} - x_r^{(1)} & \dots & x_{r,v}^{(d)} - x_r^{(d)} \end{bmatrix} \begin{bmatrix} g^{(1)} \\ \vdots \\ g^{(d)} \end{bmatrix} = \begin{bmatrix} f(\mathbf{x}_{r,1}) - f(\mathbf{x}_r) \\ \vdots \\ f(\mathbf{x}_{r,v}) - f(\mathbf{x}_r) \end{bmatrix} \quad (4-65)$$

Where $f(\mathbf{x})$ represents the output of the actual model evaluated at \mathbf{x} . Therefore, the main objective in this method is to estimate the components for the gradient vector \mathbf{g} required for linearization.

Therefore, selecting the neighborhood is a crucial step in this procedure and must be carried out carefully. It can be done by considering a threshold value α defined as the maximum

Euclidian distance from the reference point that a potential neighbor can be found, which is mathematically represented by Equation 4-66 [47].

$$\|\mathbf{x} - \mathbf{x}_r\| < \alpha \quad (4-66)$$

This threshold value can be heuristically estimated using Equation 4-67 [47].

$$\alpha = \frac{2}{K} \sum_i^K \|\mathbf{n}_j - \mathbf{x}_r\| \quad (4-67)$$

Where \mathbf{n}_j is the j -th closest point from \mathbf{x}_r in terms of Euclidian distance. As the design space as well as the gradient vector have d components, the size of the neighborhood must be at least equals d to solve Equation 4-65. In this work, the value of K in Equation 4-67 is set as $4d$ at each iteration to attempt satisfying such condition at all iterations [47]. If a design point is very isolated, i.e. the number of neighbors is still lower than dimensions after evaluating Equation 4-67, the value of α is dynamically increased by 20% at each additional iteration until d neighbors are chosen. This step prevents Equation 4-65 to become undetermined.

At the beginning of the iterative procedure, the experiment design is still small and a point very far from the reference one can be selected as a neighbor, which would not provide much information about the degree of linearity at the region of interest [47]. In the conventional LOLA algorithm, two metrics named as cohesion and adhesion are used to determine the set of design points forming the so-called ideal neighborhood, which are mathematically expressed by Equations 4-68 and 4-69, respectively [47].

$$C = \|\mathbf{x} - \mathbf{x}_r\| \quad (4-68)$$

$$A_d = \min_{\mathbf{q} \in N(\mathbf{x}_r)} \|\mathbf{q} - \mathbf{x}_r\| \quad (4-69)$$

The cohesion criterion represents the Euclidian distance from a neighbor to \mathbf{x}_r , while the adhesion measures how distant neighbors are from each other [46]. The ideal neighborhood can be defined as set of points characterized by low cohesion and high adhesion values, which leads to a multi-objective optimization problem that has no closed solution [46].

To overcome this issue, van der Hertten et al. (2015) converted Equation 4-65 into weighted least square problem by assigning a weight values to each neighbor point, which were obtained using fuzzy logic. This extended methodology is called Fuzzy Local Linear Approximation (FLOLA).

In this method, linguistic variables or fuzzy sets are used to classify the cohesion and adhesion values as “high” or “low”, which are the core for the “fuzzyfication” step in the fuzzy theory. It can be easily done by associating them to continuous membership functions whose output varies from 0 to 1 and give a measure for the degree of truth for a given statement [62]. In this work, these membership functions are expressed by Equations 4-70 through 4-73 [47].

$$C_{high} = \exp\left[-\frac{(C - \alpha)^2}{2(\alpha\sigma_{ch})}\right] \quad (4-70)$$

$$A_{high} = \exp\left[-\frac{(A - A_{max})^2}{2(A_{max}\sigma_{ah})}\right] \quad (4-71)$$

$$A_{low} = \exp\left[-\frac{A^2}{2(A_{max}\sigma_{al})}\right] \quad (4-72)$$

For the scope of this work, the fuzzy parameters σ_{ch} , σ_{ah} , and σ_{al} were assumed to be 0.3, 0.27, and 0.3, respectively [47]. Also, two fuzzy sets were attributed to adhesion once high values for this variable are usually difficult to be achieved and requires better control [47]. Next, the Mandani Fuzzy Inferential System (FIS) is applied to compile and map the fuzzy sets for cohesion and adhesion into the one corresponding to the weighting factors, which is defined as “low”, “average”, or “high” using three triangular membership functions represented by Equations 4-73 through 4-75, respectively [47].

$$W_{low} = \max\left[\frac{0.13-w}{0.13}, 0\right] \quad (4-73)$$

$$W_{low} = \max\left[\min\left(\frac{w-0.13}{0.4-0.13}, \frac{0.6-w}{0.6-0.4}\right), 0\right] \quad (4-74)$$

$$W_{high} = \max\left[0, \frac{w-0.57}{1-0.57}\right] \quad (4-75)$$

In these equations, three intervals were used to classify the weighting factors whose width values were suggested by van der Hertten et al. (2015). The inferential process is carried out based on several “if-then” rules, which are presented as follows [47]:

- If cohesion is high AND adhesion is low, THEN weight is high;
- If cohesion is high AND adhesion is high, THEN weight is average;
- If cohesion is NOT high AND adhesion is low, THEN weight is average;
- If cohesion is NOT high AND adhesion is high, THEN weight is low.

The combined evaluation each of these rules provides the final membership value for the weighting factor corresponding to each neighbor point [62]. Finally, they are converted to numerical weight value using a “defuzzification” approach called centroid method [62]. Once weights have been assigned to each neighbor, the estimated gradient vector can be obtained by solving the weighted least square problem given by Equations 4-76 [47].

$$\mathbf{g} = (\mathbf{D}^T \mathbf{W} \mathbf{D})^{-1} \mathbf{D}^T \mathbf{W} \mathbf{Y}_D \quad (4-76)$$

Where:

$$\mathbf{g} = \begin{bmatrix} \mathbf{g}^{(1)} \\ \vdots \\ \mathbf{g}^{(d)} \end{bmatrix} \quad (4-77)$$

$$\mathbf{W} = \begin{bmatrix} w_{r1} & \cdots & 0 \\ \vdots & \ddots & \vdots \\ 0 & \cdots & w_{rv} \end{bmatrix} \quad (4-78)$$

$$\mathbf{D} = \begin{bmatrix} x_{r,1}^{(1)} - x_r^{(1)} & \cdots & x_{r,1}^{(d)} - x_r^{(d)} \\ \vdots & \ddots & \vdots \\ x_{r,v}^{(1)} - x_r^{(1)} & \cdots & x_{r,v}^{(d)} - x_r^{(d)} \end{bmatrix} \quad (4-79)$$

$$\mathbf{Y}_D = \begin{bmatrix} f(\mathbf{x}_{r,1}) - f(\mathbf{x}_r) \\ \vdots \\ f(\mathbf{x}_{r,v}) - f(\mathbf{x}_r) \end{bmatrix} \quad (4-80)$$

Finally, the approximation error due to linearization at \mathbf{x}_r can be calculated by Equation 4-81 [46].

$$E(\mathbf{x}_r) = \sum_{j=1}^v |f(\mathbf{x}_{r,j}) - (f(\mathbf{x}_r) + (\mathbf{x}_{r,j} - \mathbf{x}_r) \cdot \mathbf{g})| \quad (4-81)$$

The FLOLA algorithm was implemented in MATLAB[®] and the fuzzy operations were carried out using the Fuzzy Logic Toolbox.

4.3.7. Monte-Carlo Voronoi Approximation

The FLOLA approach includes the exploitation capability to the sequential design strategy, which focus on the locations already identified as nonlinear. However, pure exploitation designs would not be able to globally explore the design space. Therefore, the contribution of exploration must also be integrated to the overall sequential strategy algorithm, which is easily done by applying the Monte-Carlo Voronoi approximation proposed by Crombecq et al. (2011).

This technique uses the Voronoi Tessalation approach to identify the distribution pattern of points at each portion of the response domain. The Voronoi cell is defined as the sub-region in the design space containing all the points that are located as closer to x_r than any other ones [46].

The union of all Voronoi cells defines the Voronoi Tessellation and the volume of a particular Voronoi cell gives a quantitative measure of the density of samples at the region where it is located [46]. If the design points are close to each other, their Voronoi cells are going to be small while larger volumes would be observed for those that are isolated. Therefore, unexplored regions would be characterized by large Voronoi cells and a sequential design focusing on exploration would attempt to increase density of points at those regions [47]. However, computing the Voronoi Tessellation and the volume of each

cell can be computationally expensive [47]. According to Crombecq et al. (2011), the sequential design strategy only requires an approximation for the Voronoi volume, which can be obtained by using the Monte-Carlo Voronoi algorithm showed in Figure 4-6.

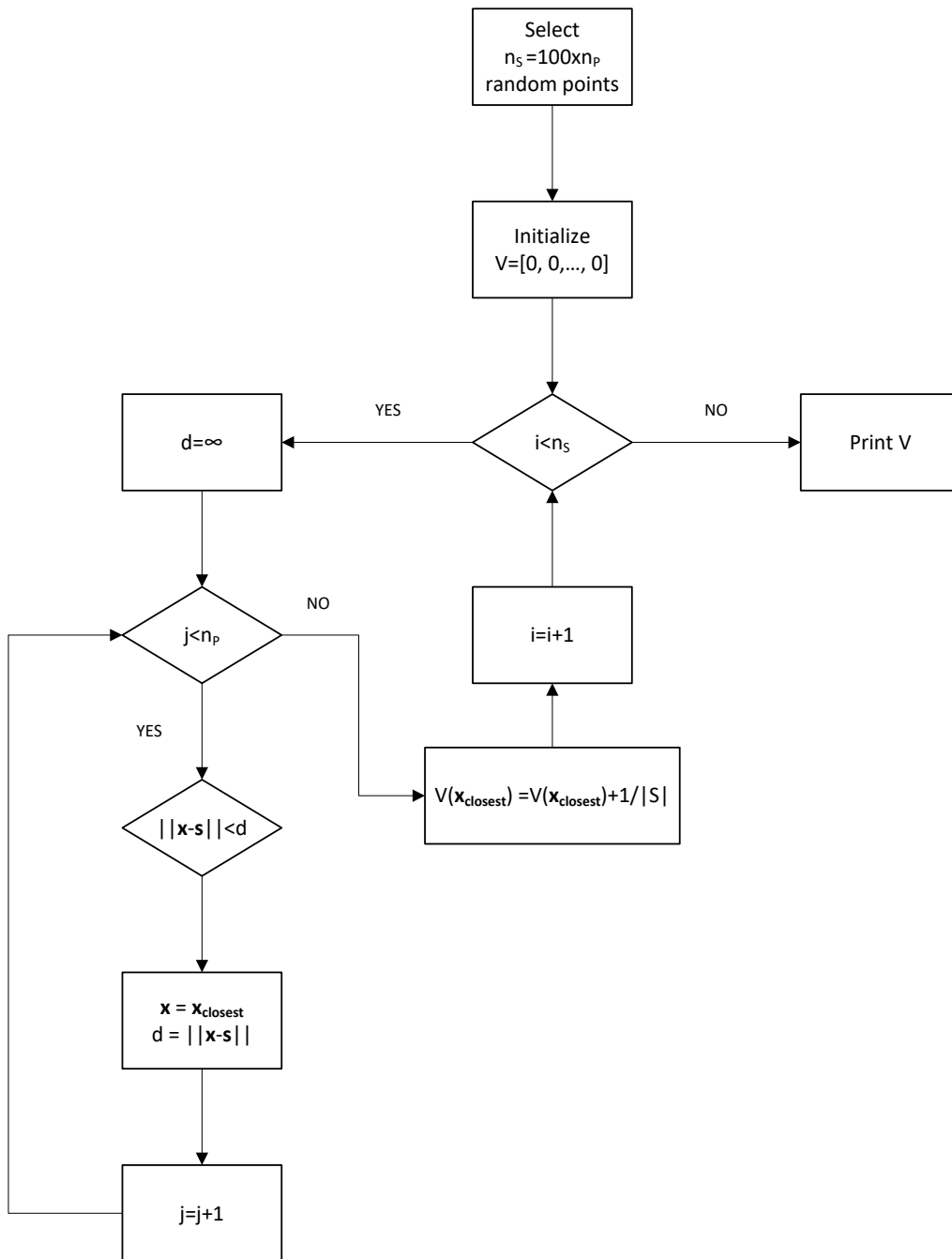


Figure 4-6: Algorithm to estimate the Voronoi cell volume [46]

In this algorithm, the design space is populated with n_s random points generated following the uniform distribution, which form a subset named S . Crombecq et al. (2011) recommended that the required number of random samples to be generated must be 100 times bigger than the size of the initial experiment design. Then, for each random point in S , its Euclidian distance to each design point is computed and used to estimate the volume of its closest Voronoi cell.

4.3.8. FLOLA-Voronoi Sequential Design Strategy

At each iteration, the new additional points to be augmented to the experiment design must be selected based on a criterion that balances the contributions from both exploitation and exploration features. This step is carried out by using Equation 4-82, which is an objective function obtained by combining the linear approximation errors and the estimated Voronoi cell volumes computed for each design point [47].

$$H(\mathbf{x}_r) = V(\mathbf{x}_r) + \frac{E(\mathbf{x}_r)}{\sum_{i=1}^{n_p} E(\mathbf{x}_i)} \quad (4-82)$$

Where $V(\mathbf{x}_r)$ is the approximated volume for the Voronoi cell containing \mathbf{x}_r . First, this equation is evaluated for all the points in the current experiment desing and the obtained values are ascendingly sorted. Then, the additional point x_{new} is selected as one of the random points used to calculated the Voronoi cell volume for the sample having the highest value of $H(\mathbf{x}_r)$, which has the maximum distance from the reference point and its

neighbors, simultaneously [46]. The full algorithm proposed by van der Hertten et al. (2015) was implemented in MATLAB[®] and applied in this work, which the full calculation routine is represented in the block diagram in Figure 4-7.

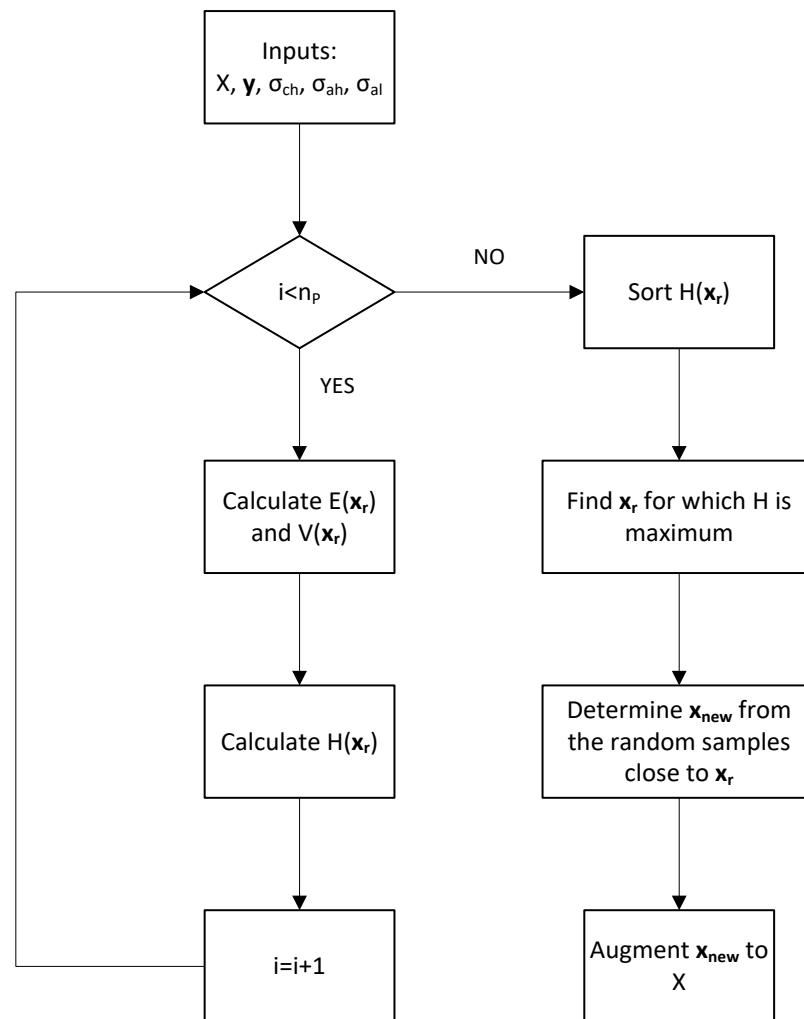


Figure 4-7: FLOLA-Voronoi Sequential Design Strategy [47]

4.3.9. Gaussian Process Surrogate Model

The Gaussian process surrogate model is a stochastic approach extensively used to approximate the response of deterministic models. The predicted cloud point obtained by solving the coupled reactor and thermodynamic modules for a given set of operating conditions and paraffinic compositions can be generically represented by Equation 4-83 [63].

$$y(\mathbf{x}) = \sum_h \beta_h f_h(\mathbf{x}) + \varepsilon(\mathbf{x}) \quad (4-83)$$

For deterministic models, no random or measurement errors affects the model response and the lack of fit is equal to modelling error itself, i.e. if several reactor simulations are performed for the same set of operating conditions and compositions, the same cloud point value would be obtained for all runs. In this case, the prediction errors are said to be correlated and the degree of correlation between two points within the design space is a function of Euclidian distance between them, which defines the so-called Kernel function [64]. In this work, the ARD Squared Exponential Kernel given by Equation 4-84 was selected as the correlation function to build the cloud point surrogate model due to its extensive application [65].

$$K(\mathbf{x}_i, \mathbf{x}_j) = \sigma_f^2 \exp \left[-\frac{1}{2} \sum_{h=1}^d \frac{|x_i^{(h)} - x_j^{(h)}|^2}{\theta_h^2} \right] \quad (4-84)$$

This function allows to obtain a metric to compute the magnitude of the effect of each input variable on the predicted cloud point behavior. The parameter σ_f represents the signal standard deviation and θ_h is the characteristic length scale. The prior parameter is a

quantitative measurement on how an input variable is affecting the model response [65]. Each index “h” represents a selected process input variable. Also, the error can be considered as a random variable following a normal distribution with mean zero and variance σ^2 , which is mathematically represented by Equation 4-85 [63].

$$\varepsilon(\mathbf{x}) \sim N(0, \sigma^2) \quad (4-85)$$

By using the Equation 4-84 to estimate the level of uncertainty for cloud point prediction, the first term in Equation 4-83 can be replaced by a constant and the regression equation for the cloud point response can be rewritten as shown by Equation 4-86 [63].

$$y(\mathbf{x}) = \mu + \varepsilon(\mathbf{x}) \quad (4-86)$$

In order to obtain the final form for the surrogate model, the hyperparameters μ , σ , σ_f , and θ_h must be estimated by maximizing the likelihood function given by Equation 4-87 [64].

$$L = \frac{1}{(2\pi)^{n_p/2} (\sigma^2)^{n_p/2} |\mathbf{R}|^{1/2}} \exp \left[-\frac{(\mathbf{y} - \mathbf{v}\mu)^T \mathbf{R}^{-1} (\mathbf{y} - \mathbf{v}\mu)}{2\sigma^2} \right] \quad (4-87)$$

Where \mathbf{V} is a vector whose entries are equal to one while the matrix \mathbf{R} is the correlation matrix defined by Equation 4-88 [63].

$$\mathbf{R} = \begin{bmatrix} K(\mathbf{x}_1, \mathbf{x}_1) & \cdots & K(\mathbf{x}_1, \mathbf{x}_{n_p}) \\ \vdots & \ddots & \vdots \\ K(\mathbf{x}_{n_p}, \mathbf{x}_1) & \cdots & K(\mathbf{x}_{n_p}, \mathbf{x}_{n_p}) \end{bmatrix} \quad (4-88)$$

Assuming that the parameters θ_h are known, the values of μ and σ can be easily estimated by taking the first derivative of Equation 4-87 and setting it to zero, which leads to Equations 4-89 and 4-90, respectively [64].

$$\hat{\mu} = \frac{\mathbf{v}^T \mathbf{R}^{-1} \mathbf{y}}{\mathbf{v}^T \mathbf{R}^{-1} \mathbf{v}} \quad (4-89)$$

$$\hat{\sigma}^2 = \frac{(\mathbf{y} - \mathbf{v}\hat{\mu})^T \mathbf{R}^{-1} (\mathbf{y} - \mathbf{v}\hat{\mu})}{n_p} \quad (4-90)$$

By substituting Equations 4-89 and 4-90 into Equation 4-87, the resulting equations is maximized to obtain the Kernel parameters σ_f and θ_h . Once all the required parameters are estimated, the cloud point response at any arbitrary point \mathbf{x}^* can be predicted using the unbiased predictor expressed by Equation 4-91 [63].

$$\hat{y}(\mathbf{x}^*) = \hat{\mu} + \mathbf{r}^T \mathbf{R}^{-1} (\mathbf{y} - \mathbf{v}\hat{\mu}) \quad (4-91)$$

The first term in this equation represents the estimated value for the mean of the stochastic process while the second one adjusts this value so that it becomes as close as possible to the actual response. The vector \mathbf{r} represents a vector whose elements are the correlation values between the \mathbf{x}^* and the points in the experimental design expressed by Equation 4-92 [63].

$$\mathbf{r} = [K(\mathbf{x}^*, \mathbf{x}_1), \dots, K(\mathbf{x}^*, \mathbf{x}_{n_p})] \quad (4-92)$$

The main advantage in using the Gaussian process over other surrogate models to approximate deterministic models is that it provides a way to estimate the level of uncertainty for the deterministic prediction as the actual response y is treated as a random variable [64]. Therefore, it is possible to calculate the variance for the prediction using Equation 4-93 [64].

$$s^2(\mathbf{x}^*) = \hat{\sigma}^2 \left(1 - \mathbf{r}^T \mathbf{R}^{-1} \mathbf{r} + \frac{(1 - \mathbf{v}^T \mathbf{R}^{-1} \mathbf{r})}{\mathbf{v}^T \mathbf{R}^{-1} \mathbf{v}} \right) \quad (4-93)$$

4.4. Results and Discussions

4.4.1. Industrial Case Study

The proposed cloud point soft-sensor is developed for the industrial reaction unit shown in Figure 4-8, which consists of two multi-bed reactors with two HDS and one HDW sections each.

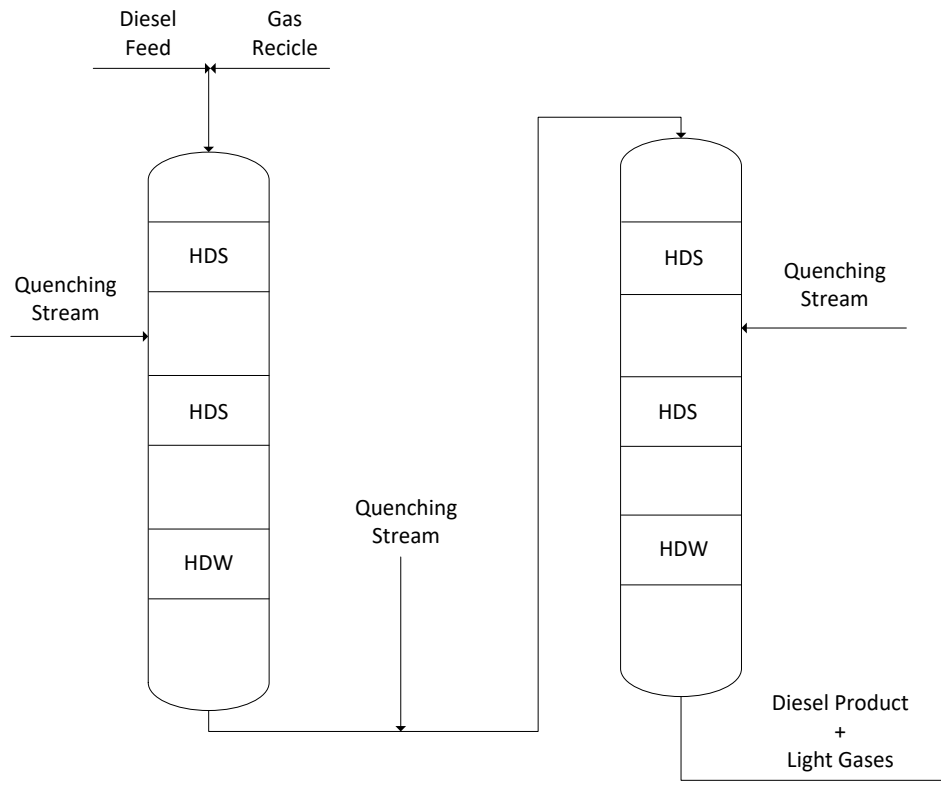


Figure 4-8: Schematic representation of the industrial reactor unit under study

In a typical operation, the gas recycle and diesel streams are first mixed and it is assumed that the resulting mixture reaches thermodynamic equilibrium at the distribution plate, which is used to obtain a good liquid distribution along the beds. As hydrodesulfurization reactions are severely exothermic, quenching streams are injected into the system to control

the bed temperatures and avoid catalyst deactivation. It is assumed that only one stream is injected between the HDS beds as the reactions taking place at the catalytic dewaxing ones are endothermic and requires high operating temperature to provide significant level of conversion. It is also considered that the quenching fluid has the same composition as the gas recycle and temperature as 40°C [11]. The quenching mole flow rate required to bring the outlet bed temperature to that of reactor inlet can be easily calculated using the energy balance expressed by Equation 4-94 assuming that only a small amount of liquid is flashed after mixing.

$$F_{quench}^G = \frac{[F_{total}^G C_{pG} (T_G^{out} - 40) + F_{total}^L C_{pL} (T_L^{out} - 40)]}{C_{pG} (T_{in} - 40)} \quad (4-94)$$

The values for the reactor operating conditions and bed lengths were not provided by the local refinery where similar reactor is applied; however, they can be estimated from target values of product sulfur concentration and cloud point. Hence, it can be done by minimizing the objective function represented by Equation 4-95.

$$F = \left(\frac{C_S^{ind} - C_S^{cal}}{C_S^{ind}} \right)^2 + \left(\frac{CP^{ind} - CP^{cal}}{CP^{ind}} \right)^2 \quad (4-95)$$

As this equation can be highly nonlinear, bound constraints must be applied to the decision variables chosen as inlet pressure, temperature, H₂/Oil ratio, and bed lengths to obtain a realistic solution. These constraints were chosen based on common industrial values reported by Satterfield (1975). Also, the industrial value of Liquid Hourly Space Velocity (LHSV) was found to be 3.25. After performing several reactor simulations for different conditions, the constraints summarized in Table 4-9 were selected based on the limitations related to vapor-liquid equilibrium and reactor operation.

Table 4-9: Adopted constraints for operating conditions and reactor dimensions

Process Variable	Constraint
Inlet Pressure (bar)	$40 \leq P_{reactor} \leq 60$
Inlet Temperature (K)	$603.15 \leq T_{in} \leq 623.15$
Hydrogen-to-Oil ratio (scf/bbl)	$1000 \leq H_2/Oil \leq 2500$
Catalytic Bed Length (m)	$3 \leq L_i \leq 6$
Reactor Diameter (m)	$1 \leq D \leq 3$

The performance of hydrodewaxing reactors are usually given in terms of cloud point improvement, which is represented by Equation 4-96.

$$CP_{imp} = |CP_{feed} - CP_{prod}| \quad (4-96)$$

The improvement reported in the industrial data was around -3°C , which indicates small conversions in the HDW beds. To have a better application example, the optimization procedure applied in this section was performed using the same industrial distillation data and sulfur content reported for the diesel feedstock described in section 4.3 while assuming the feed and product cloud points as -20°C and -35°C , respectively. The gas recycle composition was taken directly from the industrial data, which is not reported in this work due to proprietary reasons. The calculated values of outlet sulfur concentration and cloud point for the dewaxed diesel product were obtained by applying the developed soft-sensor containing both reactor and thermodynamic modules described in section 4.7. The constrained interior-point algorithm available in the MATLAB[®] Optimization Toolbox was

used to solve the minimization problem. The estimated reactor dimensions and operating conditions are shown in Table 4-10.

Table 4-10: Reactor dimensions and operating conditions for the industrial reactor unit

Process Parameter	Value
1 st HDS Bed Length (m)	5.04
2 nd HDS Bed Length (m)	5
3 rd HDS Bed Length (m)	5
4 th HDS Bed Length (m)	5.03
1 st HDW Bed Length (m)	4.84
2 nd HDW Bed Length (m)	4.90
Reactor Diameter (m)	2.06
Reactor Pressure (bar)	54
Reactor Inlet Temperature (K)	612.84
Hydrogen-to-Oil Ratio (scf/bbl)	1320

By simulating the reactor operation using the proposed sensor and the previous dimensions and operating conditions, the calculated outlet sulfur concentration and cloud point temperature were checked with the target values as shown in Table 4-9.

Table 4-11: Comparison between target and calculated values for the output variables

Outlet Variable	Target Value	Calculated Value
Sulfur Content (ppm)	4.8	4.81
Cloud Point (°C)	-35	-32.47

The calculated sulfur content is very close to the target one while the cloud point is deviated by approximately 2.5°C. It can be explained based on conflicting objectives between the hydrodesulfurization and hydrodewaxing processes in terms of pressure. The rate equations for HDS and HDW are directly and inversely proportional to the hydrogen solubility in liquid phase, respectively. Hence, decreasing the hydrogen concentration in that phase by lowering the pressure within the reaction system would decrease the sulfur conversion but significantly increase the cloud point improvement.

The temperature profile obtained by simulating the industrial unit using the estimated dimensions and operating conditions is shown in Figure 4-9.

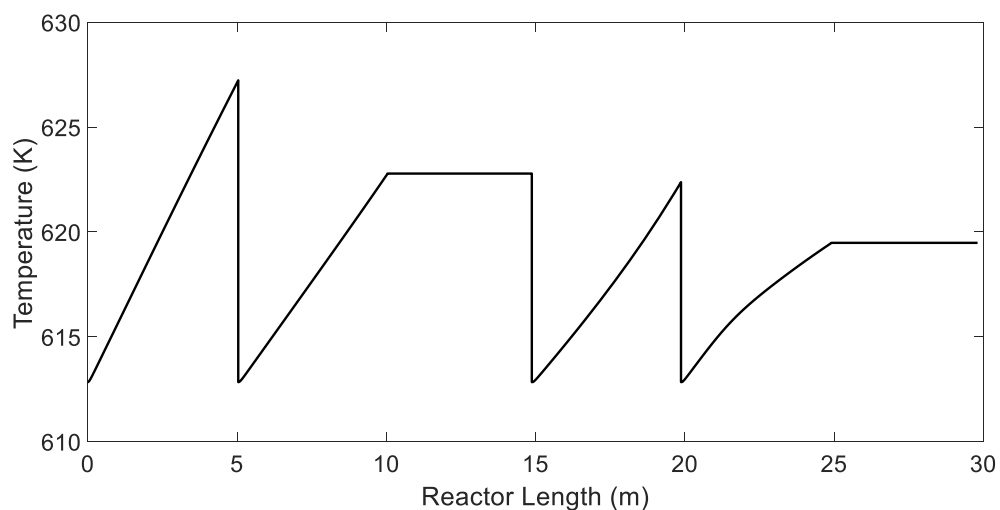


Figure 4-9: Simulated temperature profile across the industrial unit

It was observed from the simulation that the temperature difference between gas and liquid phases were very small meaning that the resistance for interphase heat transfer was not significant, and for this reason, only the temperature profile for the liquid phase is showed in Figure 4-9. The regions of temperature raise correspond to the HDS beds while the flat ones are related to the isothermal HDW sections. Also, the quenching locations can be identified by the regions of sudden temperature drop. The overall profile satisfies the common technical constraints imposed in industry once the temperature raise in each HDS section is below the maximum allowed value of 30°C to preserve the catalyst activity [66]. Finally, the temperature profile for the last HDS bed presents more nonlinearity than the other ones as the amount of sulfur compounds is very low in that section and the heat effects due to evaporation becomes comparable to those related to the exothermic reactions.

To assess the performance of the reactor in producing ULSD, the simulated sulfur concentration profile as well as the evolution of the total mole flow rate for the individual

sulfur compounds along the industrial unit are shown in Figures 4-10 and 4-11, respectively.

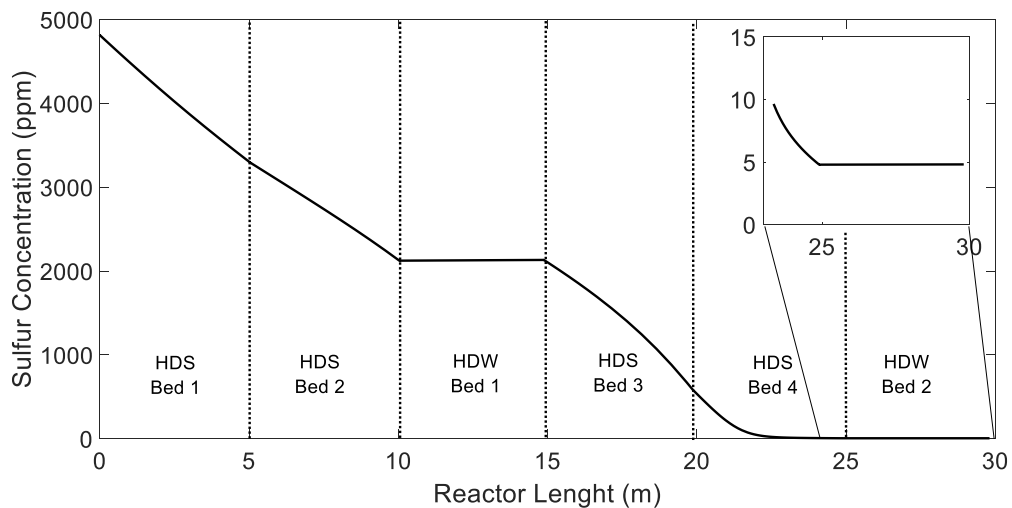


Figure 4-10: Simulated sulfur concentration profile along the industrial reactor

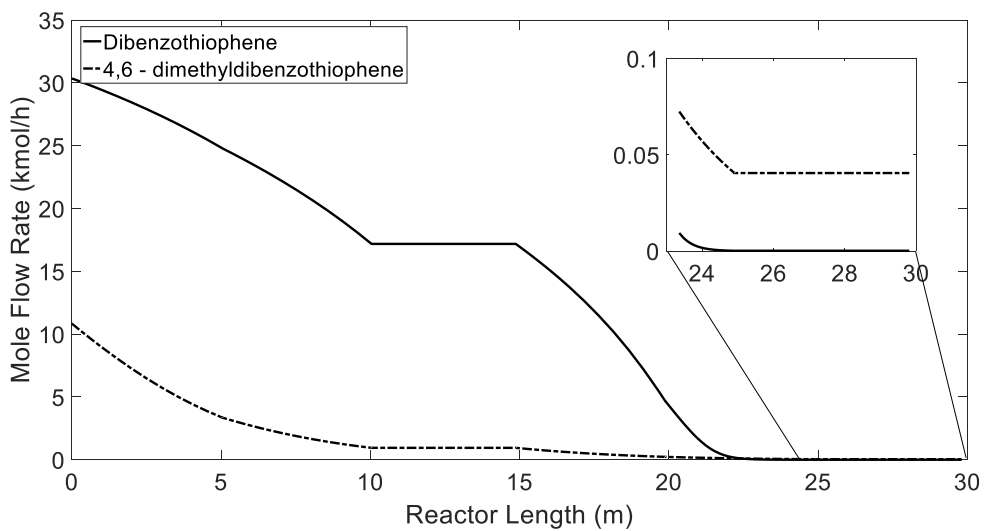


Figure 4-11: Mole flow rate evolution for the sulfur compounds along the industrial reactor

Figure 4-10 shows that the operating conditions and reactor dimensions found in this section led to an industrial reaction unit that satisfactorily reaches the target sulfur concentration to produce diesel with ultra low sulfur content while reducing the cloud point to desired values. The first reactor reduces the sulfur concentration from 4807.96 to 2000 ppm and the second one from 2000 to 4.81 ppm. By analyzing Figures 4-10 and 4-11, it can be observed that hydrodesulfurization of dibenzothiophene controls the processes up to the 3rd HDS bed. At the last HDS section, that compound reaches full conversion and the slow conversion of 4,6-dimethyldibenzothiophene becomes the main limiting mechanism, which explains the technical limitations common found in refineries when attempting to further reduce the sulfur content below 8 ppm identified as ULSD region.

To further illustrate the application of the proposed soft-sensor, a sensitivity analysis study involving the changes in LHSV, reactor inlet temperature, and pressure was performed as the hydrodewaxing conversion are mostly affected by those variables based on the results obtained in our previous work [52]. Figure 4-12 shows the effect of temperature on the product cloud point and the sulfur content for three different reactor pressures keeping the LHSV at its nominal value of 3.25 hr⁻¹.

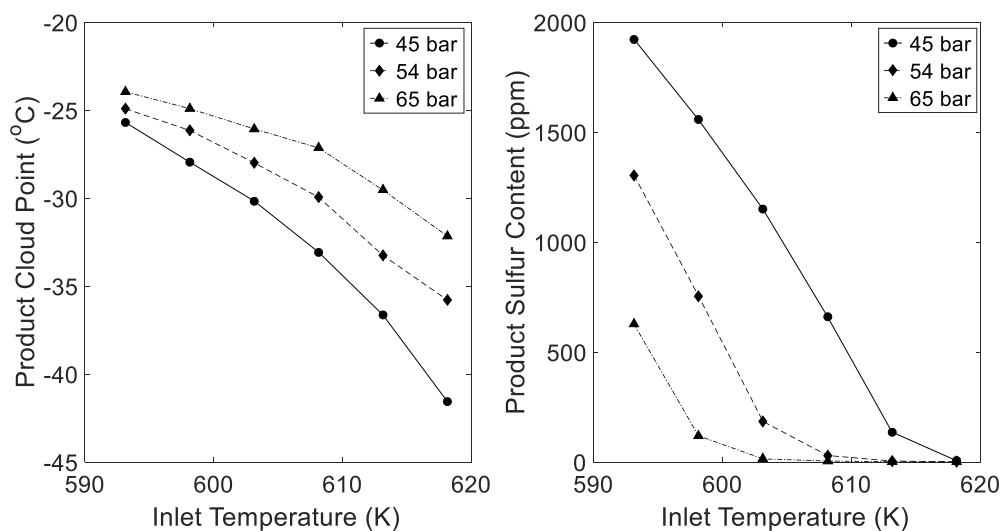


Figure 4-12: Effect of inlet temperature on the product cloud point and sulfur content at different pressures for $LHSV = 3.25 \text{ hr}^{-1}$

It can be observed that both sulfur content and cloud point of the diesel product can be simultaneously reduced by increasing the reactor inlet temperature for all levels of reactor pressure. The main explanation for this behavior is related to the strong dependence of the HDS and HDW reaction rates on temperature. Higher reactor inlet temperature leads to higher temperature profiles at all catalytic beds within the unit and the reaction rates become faster, which explains the motivation in refineries to manipulate the reactor temperature to control the quality of the diesel product. Also, it can be observed that reducing the pressure can lead to a diesel product having better cold flow properties due to the lower value of cloud point but higher sulfur content.

The effect of pressure on the product quality can be better viewed in Figure 4-13.

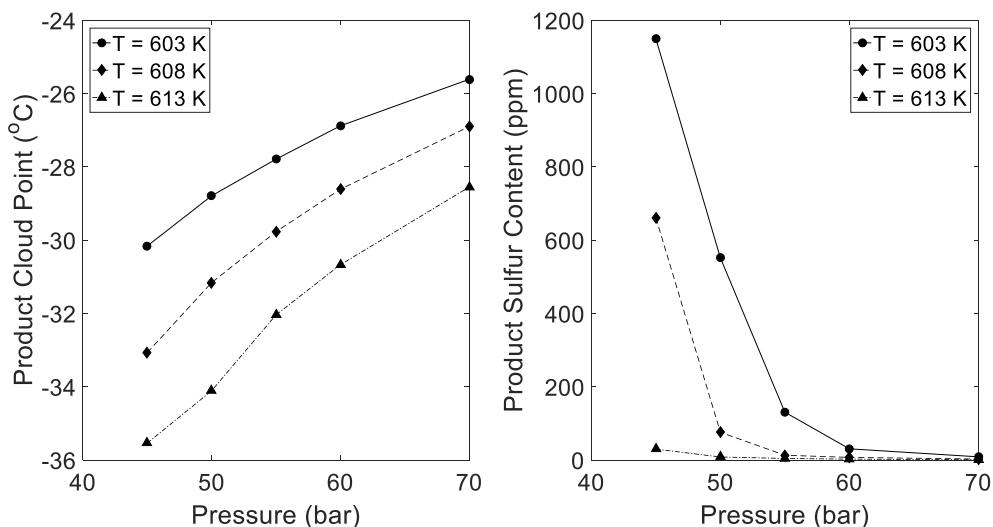


Figure 4-13: Effect of inlet pressure on the product cloud point and sulfur content at different temperatures for $LHSV = 3.25 \text{ hr}^{-1}$

It can be observed that the reactor pressure can considerably affect the quality of the diesel product specially when operating at high inlet temperatures and the conflicting objectives between the HDW and HDS mechanisms seem to be related to this variable. If the reactor inlet temperature is kept at 613 K and pressure is reduced, the unit produces diesel having better cold flow properties but richer in sulfur compounds. As previously discussed, decreasing the pressure reduces the solubility of hydrogen in liquid phase, and consequently, the reaction rates in the HDW beds becomes faster while the conversion of sulfur compounds slows down at the HDS ones. Therefore, the reactor pressure must be carefully selected to produce diesel fuels that meet the desired specifications related to sulfur concentration and cloud point.

The effect of LHSV on the product quality was also studied based on changes in temperature or pressure as shown in Figure 4-14 and Figure 4-15, respectively.

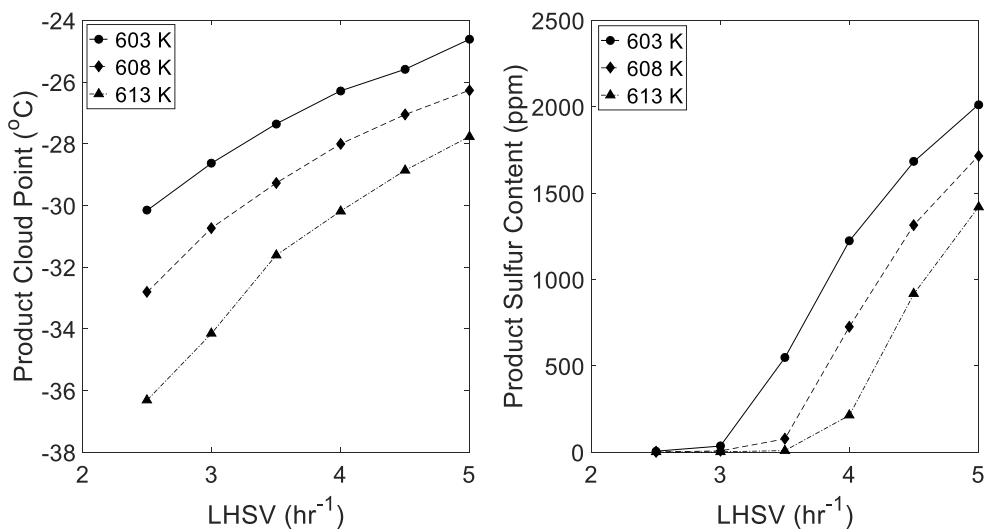


Figure 4-14: Effect of LHSV on the product cloud point and sulfur content at different temperature conditions at $P_{\text{reactor}} = 54$ bar

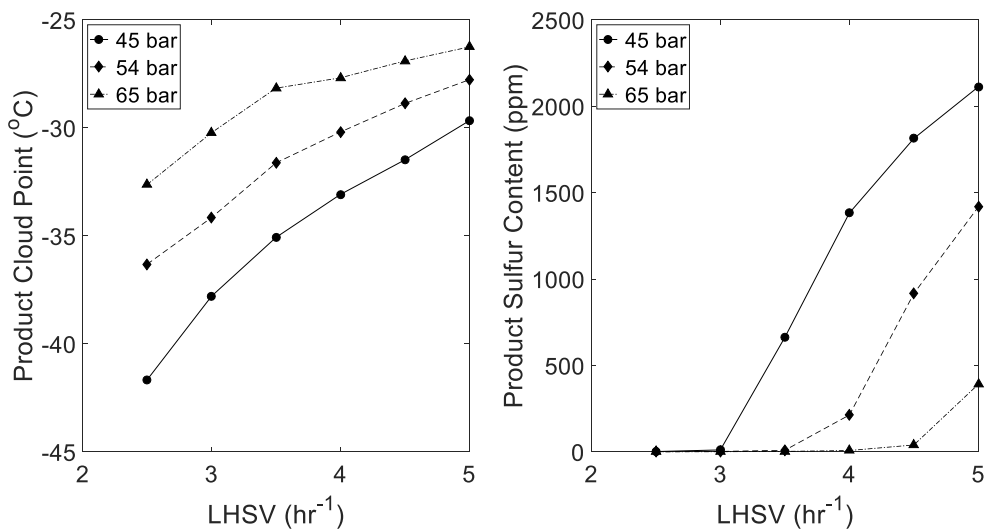


Figure 4-15: Effect of LHSV on the product cloud point and sulfur content at different pressure conditions at $T_{\text{in}} = 613$ K

It can be noted in both figures that decreasing the LHSV indeed reduces the values of both product cloud point and sulfur concentration for all different inlet temperature and pressure conditions as the sulfur and heavy normal paraffinic compounds spend more time reacting within the catalytic beds due to the higher residence time. The interaction between LHSV and reactor pressure must also be carefully analyzed. It can be observed from Figure 4-15 that the effect of LHSV on the reactor performance is strongly affected by the trade-off between the HDS and HDW objectives when the reactor pressure is changed and such interaction mostly affects the sulfur concentration of the diesel product.

Therefore, the soft-sensor proposed in this work can be used to easily design, simulate and analyze the reactor operation based on changes in different process variables. However, the high complexity of the differential equations and thermodynamic calculations can make difficult its implementation to perform on-line cloud point estimation. Also, the reactor simulations can be time-consuming as the reactor model is highly nonlinear. In order to overcome these drawbacks, a surrogate model that has simpler functional form and capable of reproducing the results with good accuracy is developed in the next sections.

4.4.2. Design of Computer Experiments

The first step in applying the sequential design strategy is to create an initial design of experiments considering the changes in the most important process variables affecting the product cloud point response. This procedure provides initial knowledge about its functional form using only few solutions obtained by using the original sensor framework.

The LHSV, reactor inlet temperature, and pressure are selected as the main process variables in this work as they strongly affect the conversion profiles specially in the HDW beds responsible to reduce the cloud point of the diesel product.

Also, the effect of the feed paraffinic composition distribution must be incorporated to the on-line soft-sensor design due to its impact on both solid-liquid equilibrium behavior and HDW conversion. However, it is not possible to consider the composition of all 24 normal paraffinic compounds due to the dimensionality constraints. To overcome this issue, only the mole fractions for the heavy normal paraffins ranging from C₂₀ to C₂₄ are chosen for the analysis as they have major impact on the cloud point response.

As an application example, the ranges for the process parameters chosen to build the surrogate model to replace the reactor and thermodynamic modules in the current sensor framework are shown in Table 4-12.

Table 4-12: Process variables and ranges adopted to develop the diesel cloud point predictor

Process variable	Range
Mole fraction of n-C ₂₀	$7.22 \times 10^{-5} \leq x_{n-C_{20}}^{inlet} \leq 1.8 \times 10^{-3}$
Mole fraction of n-C ₂₁	$6.9 \times 10^{-5} \leq x_{n-C_{21}}^{inlet} \leq 1.8 \times 10^{-3}$
Mole fraction of n-C ₂₂	$7.6 \times 10^{-5} \leq x_{n-C_{22}}^{inlet} \leq 1.9 \times 10^{-3}$
Mole fraction of n-C ₂₃	$3.9 \times 10^{-5} \leq x_{n-C_{23}}^{inlet} \leq 3.2 \times 10^{-3}$
Mole fraction of n-C ₂₄	$1.3 \times 10^{-4} \leq x_{n-C_{24}}^{inlet} \leq 3.2 \times 10^{-3}$

Inlet Pressure (bar)	$45 \leq P_{reactor} \leq 70$
Reactor Inlet Temperature (K)	$593.15 \leq T_{in} \leq 633.15$
LHSV (h^{-1})	$2 \leq LHSV \leq 5$

The initial experiment design chosen to initialize the sequential design algorithm was a “maxmin” Latin Hypercube containing 35 sample points. Once cloud point responses were obtained for all design points, the hyperparameters of the Gaussian process surrogate model were estimated by maximizing the likelihood function using the MATLAB® Statistical and Machine Learning Toolbox. At each iteration, the root relative square error (RRSE) given by Equation 4-97 was calculated by comparing the predicted cloud point values evaluated from the surrogate model with those obtained from the original sensor integrating the mechanistic models using a validation data set containing 30 data points different than those adopted for training purposes.

$$RRSE = \sqrt{\frac{\sum_i (y_i - \hat{y}_i)^2}{\sum_i (y_i - \bar{y})^2}} \quad (4-97)$$

If the RRSE is higher than the threshold value set as 0.07, the obtained surrogate model is used by the FLOLA-Voronoi algorithm to obtain information about the neighborhood surrounding the cloud point response evaluated at each design point and the degree of nonlinearity is measured at those locations. At this stage, a new point is augmented to the current design considering the exploration and exploitation trade-offs. Finally, the cloud point for this new sample is evaluated using the integrated reactor and thermodynamic models and the hyperparameters are re-estimated. The iterations are carried out until the

convergence criterion is reached. The block-diagram representing this iterative procedure is shown in Figure 4-16.

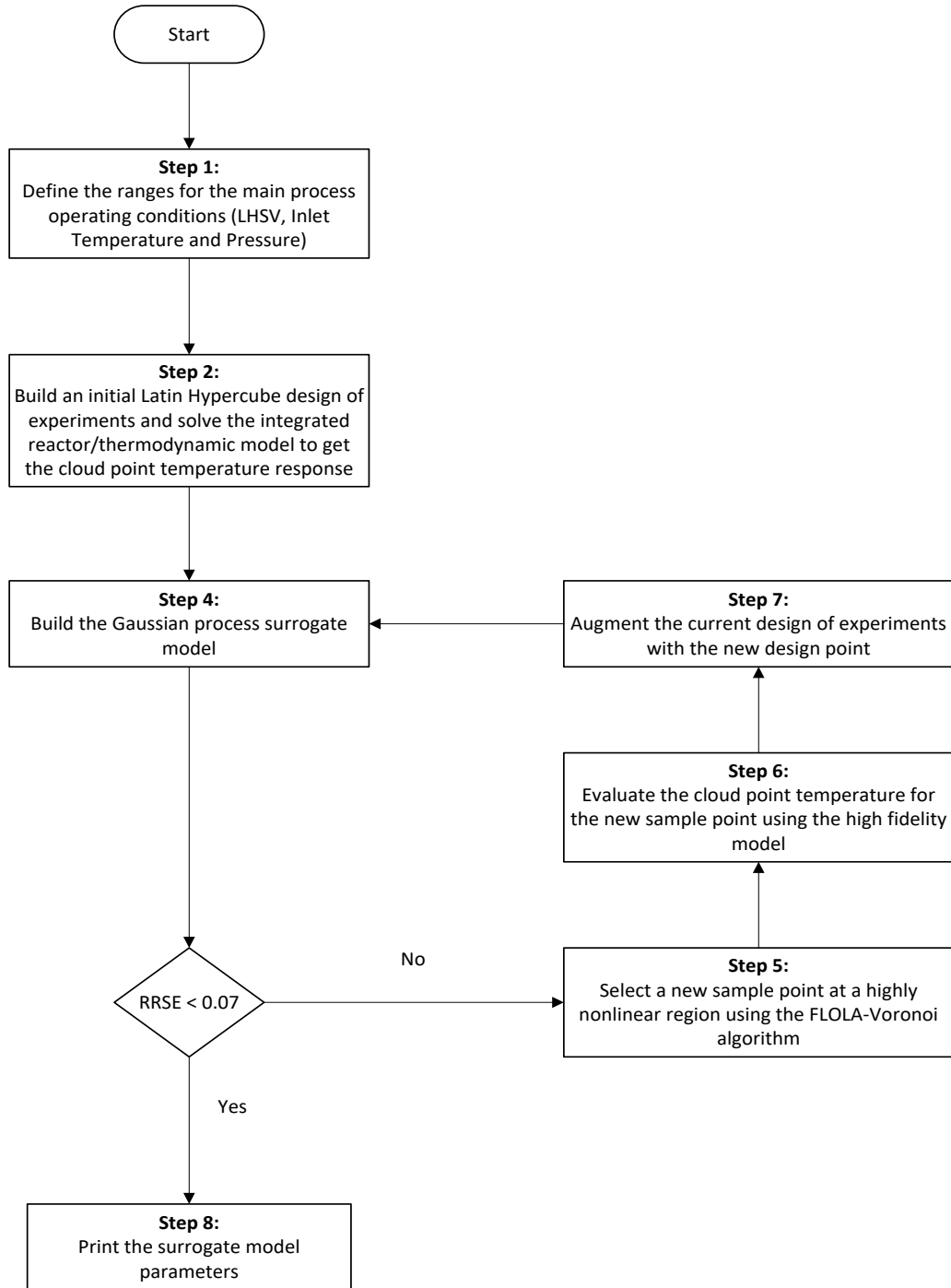


Figure 4-16: Overall algorithm for the cloud point surrogate model development

4.4.3. Nonlinearity Tracking and Exploration Capability

As building a surrogate model to reproduce the original sensor response involves a high dimensional design space, it would be difficult to show if highly nonlinear or unexplored regions are actually being tracked by the overall algorithm presented in Figure 4-16. In order to check if the sequential design strategy adopted in this work was correctly implemented, the algorithm was tested using the benchmark function “Peaks” whose functional form is expressed by Equation 4-98.

$$y = 3(1 - x_1)^2 \exp[-x_1^2 - (x_2 + 1)^2] - 10 \left(\frac{x_1}{5} - x_1^2 - x_2^2 \right) \exp(-x_1^2 - x_2^2) - \frac{1}{3} \exp[(x_1^2 + 1)^2 - x_2^2] \quad x_1, x_2 \in [-5, 5] \quad (4-98)$$

The procedure started with a Latin hypercube design with 15 points augmented with a 2^2 factorial design [47]. The membership functions and their parameters are the same as those presented in section 4.7.4 and the convergence threshold was set to 0.05 as the low dimensionality of the problem allows tighter convergence criterion. The comparison between the actual function and surrogate model responses are presented in Figure 4-17.

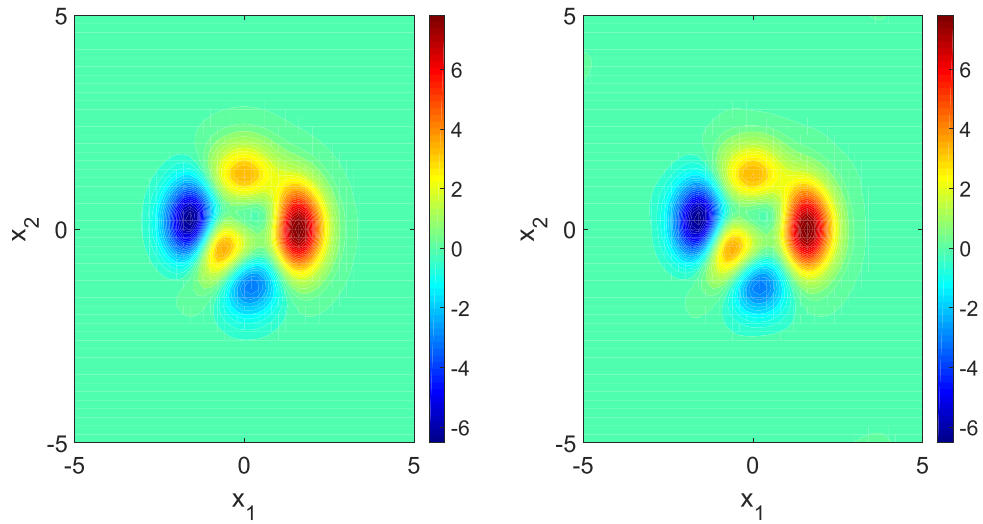


Figure 4-17: Contour plots for the true “Peaks” function (left) and surrogate model (right)

It can be observed that an almost perfect match between true and predicted responses were obtained by using the FLOLA-Voronoi algorithm. In order to check how the additional points were placed in the design space, the initial and final experiment designs were plotted and compared as shown in Figure 4-18.

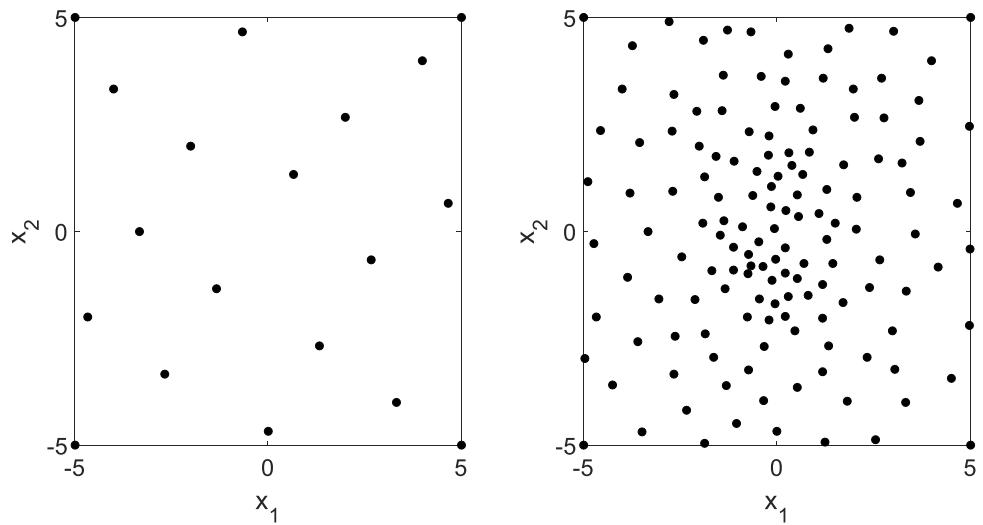


Figure 4-18: Comparison between initial (left) and final (right) experiment designs

It can be observed that the density of points is higher at the center of the design space where the nonlinear peaks are located and they are spread in such way that all of those regions are explored. Also, some additional points are placed outside the nonlinear regions because the Voronoi cells tends to be large close to the boundaries and the exploration feature of the algorithm tries to reduce their sizes as much as it can. Therefore, it can be concluded that the chosen fuzzy parameters and sequential design algorithm satisfies the conditions necessary to track nonlinearity while exploring the whole design space and it is suitable to be applied in this work.

4.4.4. On-line Cloud Point Soft-Sensor Application

Once the ranges for the main process variables are included in the FLOLA-Voronoi algorithm, the iterative procedure is initialized and additional points are added to the initial design until the accuracy of the surrogate model achieves the RRSE value of 0.07. A total of 117 additional points were needed to reach the desired convergence and the estimated parameters for the cloud point surrogate model are shown in Table 4-13.

Table 4-13: Estimated hyperparameters of the cloud point surrogate model

Parameter	Value
$\hat{\mu}$	-39.5969
$\hat{\sigma}$	0.5111

σ_f	17.6824
$\theta_{n-C_{20}}$	47.8151
$\theta_{n-C_{21}}$	69.1604
$\theta_{n-C_{22}}$	26.0629
$\theta_{n-C_{23}}$	26.0071
$\theta_{n-C_{24}}$	4.4899
θ_P	5.5723
θ_T	2.6925
θ_{LHSV}	1.8166

If the characteristic length scale related to a process variable is low, it indicates that the prior strongly affects the cloud point prediction [65]. By comparing the values of these parameters for the selected paraffinic compounds, they indicate that the composition of n-C₂₄ is the one having most impact on sensor output compared to the other normal paraffins. Likewise, the cloud point response seems to be strongly dependent on inlet temperature, pressure, and LHSV, which is expected as these variables have major impact on the reactor conversion.

Also, the composition of n-C₂₀ is shown to be slightly more important than that for n-C₂₁. It can be related to the limitations of the predictive Wilson model used to describe the solid phase behavior in the thermodynamic module. As reported by Coutinho and Ruffier-Meray

(1997), heavy paraffinic compounds can form multiple solid phases due to differences in the solidification process and this phenomenon cannot be well described by that thermodynamic model. However, it can be observed that the difference between those parameters is not very large, which also can be linked to their experimental observation that the formation of multiple solid phases does not affect much the cloud point of the mixture [27].

To check if using the surrogate model would affect the accuracy of the sensor, its response was compared with that evaluated using the original sensor framework integrating the reactor and thermodynamic modules for both training and validation data sets as shown in Figure 4-19 and 4-20.

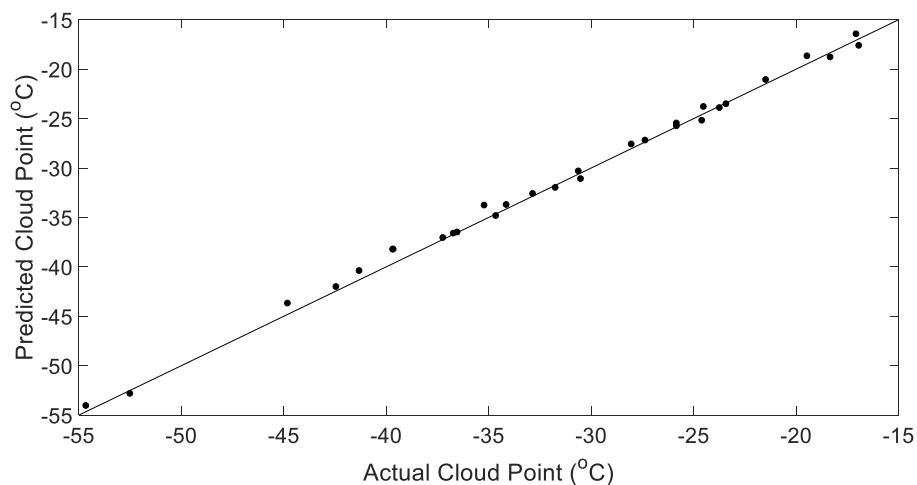


Figure 4-19: Parity plot comparing the cloud point response for the product diesel obtained from surrogate model (Predicted) and detailed model (Actual) for the validation data set

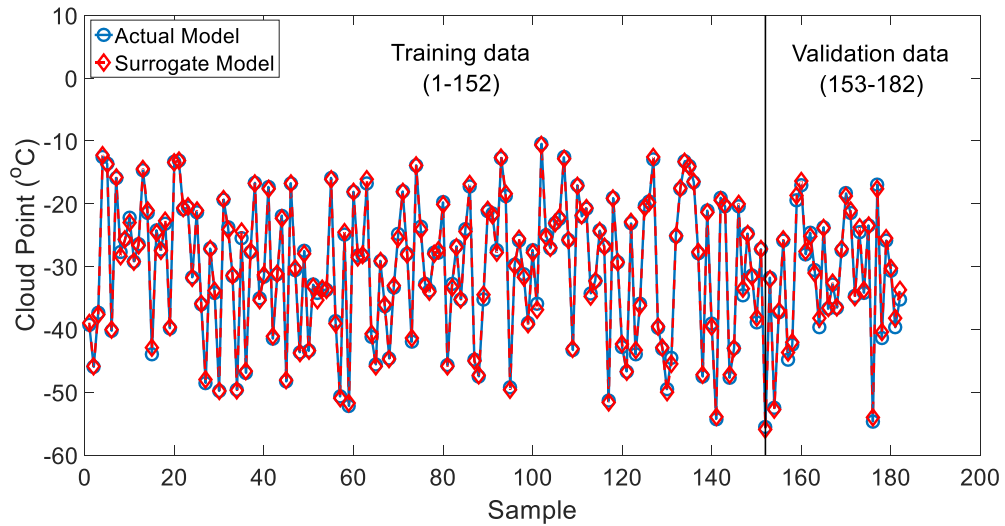


Figure 4-20: Comparison between surrogate model and original soft-sensor responses for both training and validation data sets

It can be observed in Figure 4-19 and 4-20 that the surrogate model can accurately reproduce the response obtained from the original sensor for both validation and training data sets. In order to get a quantitative view about the accuracy of the proposed surrogate model, Figure 4-21 shows the residuals between their responses for both training and validation data sets.

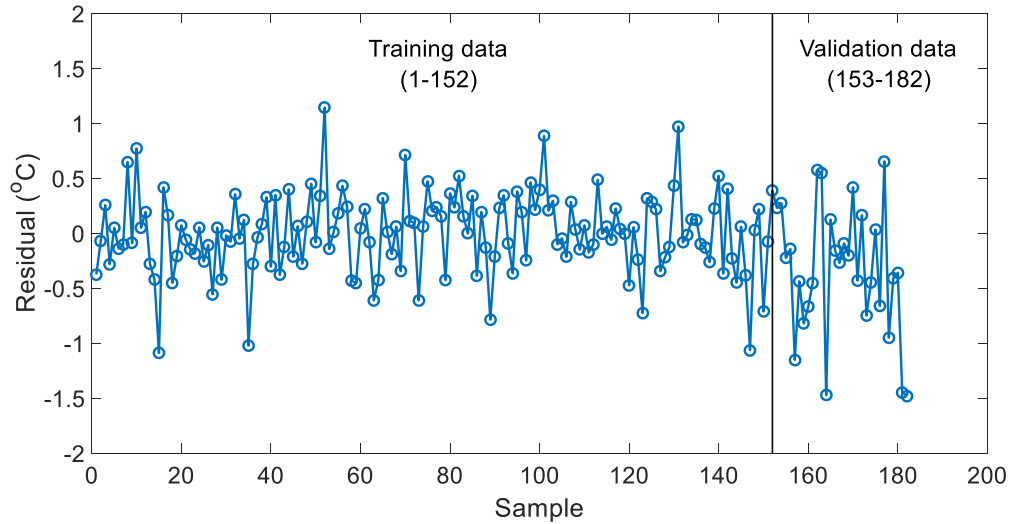


Figure 4-21: Residuals between the responses obtained from surrogate and reactor model-based soft-sensors

The maximum residual observed is approximately 1.5°C when adopting RRSE equals to 0.07 as convergence criteria for the FLOLA-Voronoi algorithm. Therefore, replacing the reactor and thermodynamic modules by the surrogate model do not affect the accuracy of the sensor and results in a sensor framework that has simpler formulation and can be easily implemented when intended to be used for on-line cloud point predictions.

To check if there are nonlinear regions affecting the accuracy of the surrogate model, the RRSE values for both training and validation data sets were also calculated for a metamodel built using the “maxmin” Latin Hypercube having same size as the final design obtained from sequential approach. This comparison is showed in Figure 4-22.

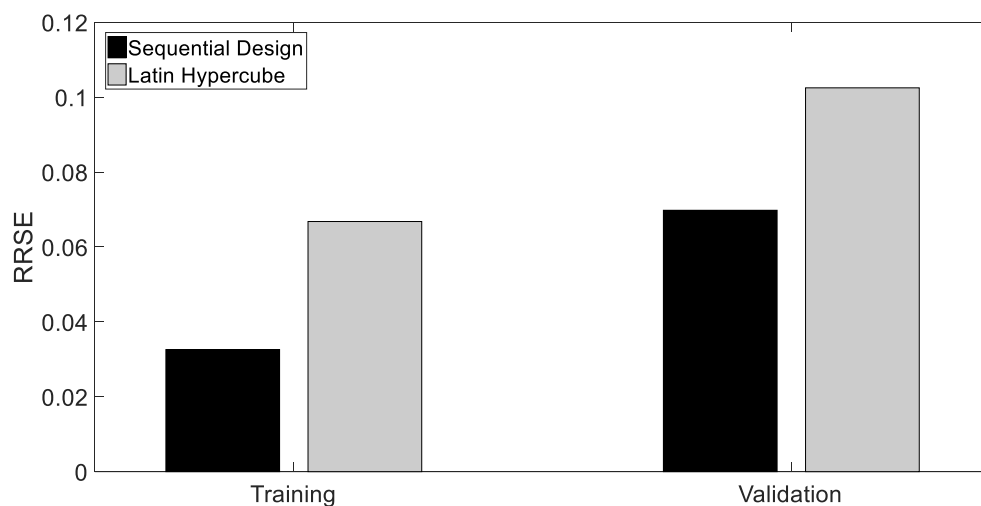


Figure 4-22: Comparison between FLOLA-Voronoi and Latin Hypercube designs in terms of surrogate model accuracy

The RRSE values obtained applying the FLOLA-Voronoi algorithm are approximately 50% and 30% lower than those observed when using the “maxmin” Latin Hypercube for both training and validation data sets, respectively. As the Latin Hypercube is a pure explorative design, it attempts to explore the design space as uniformly as possible and a surrogate model built using this type of design may not properly describe highly nonlinear regions. Therefore, the accuracy of the soft-sensor is affected by the nonlinear behavior of the cloud point response and must be properly handled.

Finally, to assess the performance of the cloud point soft-sensor in terms of computing time, the sensors integrating reactor/thermodynamic and surrogate models, respectively, were run five times in an Intel® Xeon® 3.5 GHz with 32 GB RAM using the validation data set and the average time to obtain the solutions were measured, which is reported in Table 4-14.

Table 4-14: Comparison between each type of model considered in the sensor framework in terms of computing time

Type of model	Average computing time (s)
Integrated reactor/thermodynamic model	635.79
Gaussian process surrogate model	0.03

Table 4-14 shows that there is a drastically reduction in computing time when replacing the reactor and thermodynamic modules by the surrogate model. This is another advantage in using the surrogate model developed in this section for on-line applications as cloud point predictions can be made in real time during the industrial catalytic dewaxing operation.

Therefore, it is concluded that proposed cloud point soft-sensor can be a powerful tool to be used by oil refineries attempting to have better quality control of the produced winterized diesel and monitoring the cloud point of the product in real-time.

4.5. Conclusions

A soft-sensor was proposed to predict the cloud point of dewaxed diesel fuels produced from catalytic dewaxing units. Its framework integrates three different modules to carry out the predictions based on mechanistic models. The sensor was successfully applied to study the effects of LHSV, inlet temperature, and pressure on the reactor performance. The results showed trade-off between the hydrodesulfurization and the hydrodewaxing mechanisms related to the changes in the reactor pressure. Moreover, the inlet temperature was found to

be the major factor controlling the simultaneous reduction in cloud point and sulfur concentration during the reactor operation. The proposed surrogate model drastically reduced the computing time and complexity of the sensor when replacing the mechanistic ones. The maximum residuals between their responses was 1.5°C meaning that the surrogate model does affect the accuracy of the sensor. The sequential FLOLA-voronoi and a pure explorative “maxmin” Latin Hypercube designs were compared based on the accuracy of their resulting surrogate models and the results showed that the first one reduced the RRSE values by 50% and 30% for both training and validation data sets, respectively. This outcome indicates that the surrogate model is highly affected by the nonlinearities on the cloud point response and design of experiment must be properly chosen to handle them.

The results presented in this work confirms that the proposed soft-sensor can effectively replace the visual procedures commonly adopted in petroleum refineries to measure the cloud point of diesel fuels processed in catalytic dewaxing units. Also, it can be easily implemented to control, design, and optimize the hydrodewaxing units without depending on costly and time-consuming experiments carried out in pilot reactors.

Conclusions and Recommendations

5.1. Conclusions

The catalytic dewaxing reactor is a crucial unit that allows petroleum refineries to produce diesel products with acceptable cold flow properties during winter season. However, it has not been extensively studied in terms of reactor modelling and reaction kinetics. A reactor model can be an asset to assist process engineers to design and optimize the reactor unit reducing the time and costs related to experiments carried out in pilot ones. Also, a mechanistic single-event kinetic model would allow to easily incorporate the chemistry of the process into the model formulation and eliminate the dependence of the kinetic parameters on the feedstock type. Furthermore, the outlet composition distribution obtained from the simulation can be used to determine the quality of the dewaxed diesel product. In petroleum refineries, this is done by measuring its cloud point, which involves visual procedures that are prone to large experimental errors. Hence, the first part of this thesis aimed to develop a single event kinetic model to describe the catalytic dewaxing mechanisms taking place on Pt/ZSM-5 catalysts, which no study regarding such application has been published yet in the scientific literature. The obtained kinetic parameters were then used in the second part to propose a reactor model for an industrial hydrodewaxing unit and develop a soft-sensor to perform on-line cloud point predictions during the real operation. The main contributions for the first work are:

- A total of 14 single-event kinetic parameters were estimated using experimental data for hydroconversion of n-hexadecane on shape-selective commercial Pt/ZSM-5, which are independent on the feedstock type;
- The simulations using the estimated kinetic parameters were in reasonable agreement with the experimental results, which proves that they can be used to design and optimize industrial catalytic dewaxing units;
- The reactor simulations allowed to explore and recognize the dominant reaction mechanisms at molecular-level for different operating conditions;
- The performed sensitivity analysis indicated that temperature, pressure, and LHSV are the main process variables affecting the catalytic dewaxing reactor performance in terms of total conversion and isomerization/cracking yields. The ratio H_2/HC was found to be a weak factor once it only controls the evaporation of light products due to the gas-liquid mass transfer phenomena;

The main contributions of the second study are:

- By incorporating the hydrodesulfurization kinetics as well as a solid-liquid equilibrium flash algorithm to the proposed hydrodewaxing reactor model, it was possible to analyze the performance of an industrial catalytic dewaxing unit at molecular level as well as predict the cloud point for the product diesel. The integration of such mechanistic models for the diesel dewaxing application allows easy scale-up, design, and optimization.

- By integrating three separated modules, an cloud point soft-sensor was proposed whose inputs are the measured operating conditions of the industrial unit as well as the distillation data for the feedstock. As the sensor incorporates the mechanistic features from the reactor model, it can be used for on-line cloud point prediction in different hydrodewaxing units regardless the feedstock type;
- Using the sensor to study the performance of the reactor unit, it was identified that the reactor inlet temperature, pressure, and LHSV affects the quality of the dewaxed diesel product. It was also found that that changes in the reactor pressure can lead to conflicting objectives when attempting to produce diesel with good cold flow properties and low sulfur content, and thereby, it must be carefully selected.
- The proposed Gaussian process surrogate model accurately reproduced the cloud point values obtained by solving the mechanistic models and can replace them without affecting the accuracy of the sensor. It also drastically reduced the computing time required by the sensor to carry out the cloud point estimation. It also made the sensor framework simple, which allows easy implementation to perform on-line predictions;
- The performance comparison between FLOLA-Voronoi algorithm and “maxmin” Latin Hypercube design revealed that the degree of nonlinearity is indeed significant and can affect the accuracy of the proposed soft-sensor if it is not properly handled.

5.2. Recommendations and Future Work

As this operation has not been extensively studied, the experimental data available for parameter estimation was extremely limited and several assumptions had to be made when building the reaction network in order to satisfy the required number of degrees of freedom. Attempts were made in acquiring in-house data; however, the available bench scale reactor presented several technical issues and it was not possible to be used for the purpose of this work. Therefore, obtaining more reliable experimental data using a bench scale tubular reactor is a next step for this work.

Also, the available industrial data was too generalized and incomplete once dimensions and operating conditions for the real industrial reactor were not provided. Although, optimization was used to estimate their values in the present work, the high number of degrees of freedom could lead to several different reactor configurations. Hence, it is intended to test the proposed soft-sensor using more reliable industrial data and make improvements if necessary as a future work;

Obtaining experimentally the cloud point for industrial diesel feed and products is another step for this research. After the industrial data was analyzed, it was realized that the local refinery calculated the cloud point of the reactor feedstock using a correlation, which accuracy is questionable, assuming a mixing rule that considers the feedstock as blend of several streams with fixed cloud point. Hence, acquiring in-house data under controlled conditions would assist in obtaining more accurate parameters for the proposed on-line soft-sensor;

Finally, the proposed reactor models in this work were developed considering steady state operation and cannot track the time-dependent mechanisms observed in real operations. Therefore, extending the present model and reconstruction of the soft-sensor for transient operation is the next goal for this project. Also, the reaction network is going to be modified to include possible hydrogenation steps involving aromatics in the reaction mechanism, which were not considered in this work.

Bibliography

- [1] J. A. Rob van Veen, J. K. Minderhoud, L. G. Huve and W. H. J. Stork, "Hydrocracking and Catalytic Dewaxing," in *Handbook of Heterogeneous Catalysis*, New York, VCH, 2008, pp. 2778-2808.
- [2] R. A. Rakoczy and P. M. Morse, "Consider catalytic dewaxing as a tool to improve diesel cold flow properties," *Hydrocarbon Processing*, pp. 67-69, 2013.
- [3] J. Ancheyta, S. Sanchez and M. A. Rodriguez, "Kinetic Modeling of Hydrocracking of Heavy Oil Fractions: A Review," *Catalysis Today*, vol. 109, no. 1-4, pp. 76-92, 2005.
- [4] P. J. Clymans and G. F. Froment, "Computer Generation of Reaction Paths and Rate Equations in Thermal Cracking of Normal and Branched Paraffins," *Computers & Chemical Engineering*, vol. 8, no. 2, pp. 137-142, 1984.
- [5] M. A. Baltanas and G. F. Froment, "Computer Generation of Reaction Networks and Calculation of Product Distributions in the Hydroisomerization and Hydrocracking of Paraffins on Pt-containing Bifunctional Catalysts," *Computers & Chemical Engineering*, vol. 9, no. 1, pp. 71-81, 1985.
- [6] E. Vynckier and G. F. Froment, "Modeling of the Kinetics of Complex Processes Based Upon Elementary Steps," in *Kinetic and Thermodynamic Lumping of Multicomponent Mixtures*, G. Astarita and S. I. Sandler, Eds., Amsterdam, Elsevier Publishers B.V., 1991, pp. 131-161.

- [7] H. Kumar and G. F. Froment, "A Generalized Mechanistic Kinetic Model for the Hydroisomerization and Hydrocracking of Long-Chain Paraffins," *Industrial & Engineering Chemistry Research*, vol. 46, no. 12, pp. 4075-4090, 2007.
- [8] S. A. Qader and G. R. Hill, "Hydrocracking of Gas Oil," *Industrial & Engineering Chemistry Process Design and Development*, vol. 8, no. 1, pp. 98-105, 1969.
- [9] M. A. Callejas and M. T. Martinez, "Hydrocracking of a Maya Residue. Kinetics and Product Yield Distributions," *Industrial & Engineering Chemistry Research*, vol. 38, no. 9, pp. 3285-3289, 1999.
- [10] S. Sanchez, M. A. Rodriguez and J. Ancheyta, "Kinetic Model for Moderate Hydrocracking of Heavy Oils," *Industrial & Engineering Chemistry Research*, vol. 44, no. 25, pp. 9409-9413, 2005.
- [11] H. Kumar and G. F. Froment, "Mechanistic Kinetic Modeling of the Hydrocracking of Complex Feedstocks, such as Vacuum Gas Oils," *Industrial and Engineering Chemistry Research*, vol. 46, no. 18, pp. 5881-5897, 2007.
- [12] C. S. Laxminarasimhan and R. P. Verma, "Continuous Lumping Model for Simulation of Hydrocracking," *AIChE Journal*, vol. 42, no. 9, pp. 2645-2653, 1996.
- [13] M. A. Baltanas, K. K. Van Raemdonck, G. F. Froment and S. R. Mohedas, "Fundamental Kinetic Modeling of Hydroisomerization and Hydrocracking on Noble Metal-Loaded Faujasites. 1. Rate Parameters for Hydroisomerization," *Industrial & Engineering Chemistry Research*, vol. 28, no. 7, pp. 899-910, 1989.

- [14] G. D. Svoboda, E. Vynckier, B. Debrabandere and G. F. Froment, "Single-Event Rate Parameters for Paraffin Hydrocracking on a Pt/US-Y Zeolite," *Industrial & Engineering Chemistry Research*, vol. 34, no. 11, pp. 3793-3800, 1995.
- [15] J. M. Schweitzer, P. Galtier and D. Schweich, "A Single Events Kinetic Model for the Hydrocracking of Paraffins in a Three-Phase Reactor," *Chemical Engineering Science*, vol. 54, no. 13-14, pp. 2441-2452, 1999.
- [16] N. V. Dewachtere, F. Santaella and G. F. Froment, "Application of a Single- Event Kinetic Model in the Simulation of an Industrial Riser Reactor for the Catalytic Cracking of Vacuum Gas Oil," *Chemical Engineering Science*, vol. 54, no. 15-16, pp. 3653-3660, 1999.
- [17] J. M. Martinis and G. F. Froment, "Alkylation on Solid Acids. Part 1. Experimental Investigation of Catalyst Deactivation," *Industrial & Engineering Chemistry Research*, vol. 45, no. 3, pp. 940-953, 2006.
- [18] J. M. Martinis and G. F. Froment, "Alkylation on Solid Acids. Part 2. Single-Event Kinetic Modeling," *Industrial & Engineering Chemistry Research*, vol. 45, no. 3, pp. 954-967, 2006.
- [19] T. Park and G. F. Froment, "Kinetic Modeling of the Methanol to Olefins Process. 1. Model Formulation," *Industrial & Engineering Chemistry Research*, vol. 40, no. 20, pp. 4172-4186, 2001.

- [20] T. Park and G. F. Froment, "Kinetic Modeling of the Methanol to Olefins Process. 2. Experimental Results, Model Discrimination, and Parameter Estimation," *Industrial & Engineering Chemistry Research*, vol. 40, no. 20, pp. 4187-4196, 2001.
- [21] D. N. Gerasimov, V. V. Fadeev, A. N. Loginova and S. V. Lysenko, "Hydroisomerization of Long-Chain Paraffins: Mechanism and Catalysts. Part I," *Catalysis in Industry*, vol. 7, no. 2, pp. 128-154, 2015.
- [22] C. S. Laxmi Narasimhan, J. W. Thybaut, G. B. Marin, P. A. Jacobs, J. A. Martens, J. F. Denayer and G. V. Baron, "Kinetic Modeling of Pore Mouth Catalysis in the Hydroconversion of n-octane on Pt-H-ZSM-22," *Journal of Catalysis*, vol. 220, no. 2, pp. 399-413, 2003.
- [23] C. S. Laxmi Narasimhan, J. W. Thybaut, G. B. Marin, J. F. Denayer, G. V. Baron, J. A. Martens and P. A. Jacobs, "Relumped Single-Event Microkinetic Model for Alkane Hydrocracking on Shape-Selective Catalysts: Catalysis on ZSM-22 Pore-Mouths, Bridge Acid-Sites and Micropores," *Chemical Engineering Science*, vol. 59, no. 22-23, pp. 4765-4772, 2004.
- [24] B. D. Vandergehuchte, J. W. Thybaut and G. B. Marin, "Unraveling Diffusion and Other Shape Selectivity Effects in ZSM5 Using n-Hexane Hydroconversion Single-Event Microkinetics," *Industrial & Engineering Chemistry Research*, vol. 53, no. 40, pp. 15333-15347, 2014a.
- [25] B. D. Vandegehuchte, I. R. Choudhury, J. W. Thybaut, J. A. Martens and G. B. Marin, "Integrated Stefan-Maxwell, Mean Field, and Single-Event Microkinetics

- Methodology for Simultaneous Diffusion and Reaction inside Microporous Materials," *The Journal of Physical Chemistry C*, vol. 118, no. 38, pp. 22053-22068, 2014b.
- [26] K. S. Pedersen, "Prediction of Cloud Point Temperatures and Amount of Wax Formation," *SPE Production & Facilities*, vol. 10, no. 1, pp. 46-49, 1995.
- [27] J. A. P. Coutinho and V. Ruffier-Meray, "Experimental Measurements and Thermodynamic Modeling of Paraffinic Wax Formation in Undercooled Solutions," *Industrial & Engineering Chemistry Research*, vol. 36, no. 11, pp. 4977-4983, 1997.
- [28] J. A. P. Coutinho, "A Thermodynamic Model for Predicting Wax Formation in Jet and Diesel Fuels," *Energy & Fuels*, vol. 14, no. 3, pp. 625-631, 2000.
- [29] E. Ghanaei, F. Esmailzadeh and J. Fathi Kaljahi, "A New Predictive Thermodynamic Model in the Wax Formation Phenomena at High Pressure Condition," *Fluid Phase Equilibria*, vol. 254, no. 1-2, pp. 126-137, 2007.
- [30] W. Souverijns, J. A. Martens, G. F. Froment and P. A. Jacobs, "Hydrocracking of Isoheptadecanes on Pt/H-ZSM-22: An Example of Pore Mouth Catalysis," *Journal of Catalysis*, vol. 174, no. 2, pp. 177-184, 1998.
- [31] J. A. M. Arroyo, G. G. Martens, G. F. Froment, P. A. Jacobs and J. A. Martens, "Hydrocracking and Isomerization of n-Paraffin Mixture and a Hydrotreated Gasoil on Pt/HZSM-22: Confirmation of Pore Mouth and Key-Lock Catalysis in Liquid Phase," *Applied Catalysis A: General*, vol. 192, no. 1, pp. 9-22, 2000.

- [32] H. Kumar, "Single Event Kinetic Modeling of the Hydrocracking of Paraffins," M. S. Thesis, Texas A&M University, College Station, 2004.
- [33] J. Govindhakannan, "Modeling of a Hydrogenated Vacuum Gas Oil Hydrocracker," Ph.D. dissertation, Texas Tech University, Lubbock, 2003.
- [34] D. Guillaume, E. Valery, J. J. Verstraete, K. Surla, P. Galtier and D. Schweich, "Single Event Kinetic Modelling without Explicit Generation of Large Networks: Applications to Hydrocracking of Long Chain Paraffins," *Oil & Gas Science and Technology*, vol. 66, no. 11, pp. 399-422, 2011.
- [35] G. F. Froment, J. De Wilde and K. B. Bischoff, *Chemical Reactor Analysis and Design*, Hoboken, New Jersey: Willey, 2010.
- [36] D. Peng and D. B. Robinson, "A New Two-Constant Equation of State," *Industrial & Engineering Chemistry Fundamentals*, vol. 15, no. 1, pp. 59-64, 1976.
- [37] N. Skander and C. E. Chitour, "A New Group-Contribution Method for the Estimation of Physical Properties of Hydrocarbons," *Oil & Gas Science and Technology*, vol. 57, no. 4, pp. 369-376, 2002.
- [38] American Petroleum Institute, *Technical Data Book, Petroleum Refining*, Washington: API, 1997.
- [39] E. S. Domalski and E. D. Hearing, "Estimation of the Thermodynamic Properties of Hydrocarbons," *Journal of Physical and Chemical Reference Data*, vol. 17, no. 4, pp. 1637-1678, 1988.

- [40] B. E. Poling, J. M. Prausnitz and J. P. O'Connell, *The Properties of Gases and Liquids*, New York: McGraw-Hill, 2001.
- [41] C. H. Twu, "Internally Consistent Correlation for Predicting Liquid Viscosities of Petroleum Fractions," *Industrial & Engineering Chemistry Process Design and Development*, vol. 24, no. 4, pp. 1287-1293, 1985.
- [42] L. P. Reiss, "Cocurrent Gas-Liquid Contacting in Packed Columns," *Industrial & Engineering Chemistry Process Design and Development*, vol. 6, no. 4, pp. 486-499, 1967.
- [43] Y. Sato, H. Hirose, F. Takahashi and M. Toda, in *First Pacific Chemical Engineering Congress*, 1972.
- [44] J. Song, "Building Robust Chemical Reaction Mechanisms: Next Generation of Automatic Model Construction Software," Ph.D. Dissertation, Massachusetts Institute of Technology, Cambridge, 2004.
- [45] R. C. Dougherty, D. N. Mazzone, R. F. Socha and H. K. C. Timken, "Production of High Viscosity Lubricating Oil Stock with Improved ZSM-5 Catalyst". United States Patent 6,294,077 B1, 25 September 2001.
- [46] K. Crombecq, D. Gorissen, D. Deschrijver and T. Dhaene, "A Novel Hybrid Sequential Design Strategy for Global Surrogate Modeling of Computer Experiments," *SIAM Journal on Scientific Computing*, vol. 33, no. 4, pp. 1948-1974, 2011.

- [47] J. van der Herten, I. Couckuyt, D. Deschrijver and T. Dhaene, "A Fuzzy Hybrid Sequential Design Strategy for Global Surrogate Modeling of High-Dimensional Computer Experiments," *SIAM Journal on Scientific Computing*, vol. 37, no. 2, pp. A1020-A1039, 2015.
- [48] B. Peng, "Molecular Modeling of Refining Processes," Ph.D. Dissertation, The University of Manchester, Manchester, 1999.
- [49] M. I. Ahmad, N. Zhang and M. Jobson, "Molecular Components-based Representation of Petroleum Fractions," *Chemical Engineering Research and Design*, vol. 89, no. 4, pp. 410-420, 2011.
- [50] G. F. Froment, G. A. Depauw and V. Vanrysselberghe, "Kinetic Modeling and Reactor Simulation in Hydrodesulfurization of Fractions," *Industrial & Engineering Chemistry Research*, vol. 33, no. 12, pp. 2975-2988, 1994.
- [51] Y. Wu, "Molecular Management for Refining Operations," Ph.D. Dissertation, The University of Manchester, Manchester, 2010.
- [52] E. Turco Neto, S. Imtiaz and S. Ahmed, "Single Event Kinetic Modelling of Catalytic Dewaxing on Commercial Pt/ZSM-5". Unpublished.
- [53] I. A. Van Parijs and G. F. Froment, "Kinetics of Hydrodesulfurization on a CoMo/Al₂O₃ Catalyst. 1. Kinetics of the Hydrogenolysis of Benzothiophene," *Industrial & Engineering Chemistry Product Research & Development*, vol. 25, no. 3, pp. 437-443, 1986.

- [54] V. Vanrysselberghe and G. F. Froment, "Hydrodesulfurization of Dibenzothiophene on a CoMo/Al₂O₃ Catalyst: Reaction Network and Kinetics," *Industrial & Engineering Chemistry Research*, vol. 35, no. 10, pp. 3311-3318, 1996.
- [55] V. Vanrysselberghe, R. Le Gall and F. G. F. Froment, "Hydrodesulfurization of 4-Methyldibenzothiophene and 4,6-Dimethyldibenzothiophene on a CoMo/Al₂O₃ Catalyst: Reaction Network and Kinetics," *Industrial & Engineering Chemistry Research*, vol. 37, no. 4, pp. 1235-1242, 1998.
- [56] R. R. Boesen, "Investigation and Modelling of Diesel Hydrotreating Reactions," Technical University of Denmark, Lyngby, 2010.
- [57] K. W. Won, "Thermodynamic Calculation of Cloud Point Temperatures and Wax Phase Composition of Refined Hydrocarbon Mixtures," *Fluid Phase Equilibria*, vol. 53, pp. 377-396, 1989.
- [58] M. G. Broadhurst, "An Analysis of the Solid Phase Behavior of the Normal Paraffins," *Journal of Research of the National Bureau of Standards*, vol. 66A, no. 3, pp. 241-249, 1962.
- [59] J. A. P. Coutinho, C. Dauphin and J. L. Daridon, "Measurements and Modelling of Wax Formation in Diesel Fuels," *Fuel*, vol. 79, no. 6, pp. 607-616, 2000.
- [60] A. Bondi, "van der Waals Volumes and Radii," *The Journal of Physical Chemistry*, vol. 68, no. 3, pp. 441-451, 1964.

- [61] D. L. Morgan and R. Kobayashi, "Extension of Pitzer CSP Models for Vapor Pressures and Heats of Vaporization to Long-Chain Hydrocarbons," *Fluid Phase Equilibria*, vol. 94, no. 15, pp. 51-87, 1994.
- [62] R. Fuller, Neural Fuzzy Systems, Abo Akademis tryckeri, 1995.
- [63] D. R. Jones, M. Schonlau and W. J. Welch, "Efficient Global Optimization of Expensive Black-Box Functions," *Journal of Global Optimization*, vol. 13, no. 4, pp. 455-492, 1998.
- [64] A. I. J. Forrester, A. Sobester and A. J. Keane, Engineering Design via Surrogate Modelling: A Practical Guide, Chichester: J. Willey, 2008.
- [65] The Mathworks, Inc., "Statistics and Machine Learning Toolbox: User's Guide (r2016b)," [Online]. Available: <https://www.mathworks.com/help/stats/>. [Accessed 20 November 2017].
- [66] C. N. Satterfield, "Trickle-Bed Reactors," *AIChE Journal*, vol. 21, no. 2, pp. 209-228, 1975.

Appendix A-1. Industrial Diesel Feedstock MTHS Matrix

	NP	IP	MA	DA	TA	A_A	A_AA	A_N	AN	MN	DN	TN	N_N	SI	SII	NI
C8	0.0321	0.0067	0.0054	*	*	*	*	*	*	*	*	*	*	*	*	*
C9	0.0042	0.0073	*	*	*	*	*	*	0.00525	0.00903	*	*	*	*	*	0.07725
C10	0.0019	0.0119	*	0.1099	*	*	*	*	*	*	0.0267	*	*	*	*	*
C11	0.0034	0.0131	*	*	*	*	*	*	*	*	*	*	*	*	*	*
C12	1.8E-5	0.0371	*	*	0.00246	0.0380	*	0.0400	*	*	*	*	0.0765	0.0193	*	*
C13	0.0059	0.0790	*	*	*	*	*	*	0.0225	*	*	*	*	*	*	*
C14	0.0010	0.0052	*	*	*	*	*	*	*	*	*	0.1218	*	*	0.00691	*
C15	0.0003	0.0068	0.028	*	*	*	*	*	*	0.0449	*	*	*	*	*	*
C16	0.0004	0.0159	*	*	*	*	0.0275	*	*	*	*	*	*	*	*	*
C17	0.0016	0.0240	*	*	*	*	*	*	*	*	*	*	*	*	*	*
C18	0.0004	0.0367	*	*	*	*	*	*	*	*	*	*	*	*	*	*
C19	0.0004	0.0056	*	*	*	*	*	*	*	*	*	*	*	*	*	*
C20	0.0004	0.0054	*	*	*	*	*	*	*	*	*	*	*	*	*	*
C21	0.0003	0.0052	*	*	*	*	*	*	*	*	*	*	*	*	*	*
C22	0.0004	0.0050	*	*	*	*	*	*	*	*	*	*	*	*	*	*
C23	0.0002	0.0047	*	*	*	*	*	*	*	*	*	*	*	*	*	*
C24	0.0006	0.0044	*	*	*	*	*	*	*	*	*	*	*	*	*	*

NP: Normal paraffins; IP: Isoparaffins; MA: Mono-aromatics; DA: Di-aromatics; TA: Tri-aromatics; A_A, A_AA: Biphenyl type compounds; A_N, AN: Naphteno-aromatic type compounds; MN: Mono-naphtenes; DN: Di-naphtenes; TN: Tri-naphtenes; N_N: Bicyclohexyl compounds; SI: Non-substituted dibenzothiophene; SII: Substituted dibenzothiophene; NI: Nitrogen compounds;

Appendix A-2. Validation of The Reaction Network Algorithm

Type of elementary step/species	This work	Kumar and Froment (2007)
Deprotonation/Protonation	14202	12845
Methyl-shift	3276	2670
Hydride-shift	12486	10474
PCP-isomerization	15174	10710
β -scission	2814	2335
Paraffins	891	747
Carbenium ions	7389	6167
Olefins	7946	7601